PUBLICATIONS OF
THE UNIVERSITY OF EASTERN FINLAND

Dissertations in Science, Forestry and Technology

ANAR OSPANOVA

Multipole approach in the invisibility and transparency problems

Multipole approach in the invisibility and transparency problems

Anar Ospanova

Multipole approach in the invisibility and transparency problems

Publications of the University of Eastern Finland
Dissertations in Science, Forestry and Technology
No 57

University of Eastern Finland
Joensuu
2024

Academic dissertation to be presented by permission of the Faculty of Science, Forestry and Technology for public examination in the Auditorium M100 in the Metria Building at the University of Eastern Finland, Joensuu, on 18 October, 2024, at 12 o'clock noon

Punamusta Oy
Joensuu, 2024
Editors: Pertti Pasanen

ISBN: 978-952-61-5330-8 (Print)
ISBN: 978-952-61-5331-5 (PDF)
ISSNL: 2954-131X
ISSN: 2954-131X
ISSN: 2954-1484 (PDF)

Author's address: University of Eastern Finland
Department of Physics and Mathematics
P.O. Box 111
80101 JOENSUU, FINLAND
email: anar.ospanova@uef.fi

Doctoral programme: Forestry and Technology

Supervisors: Professor Yuri Svirko
University of Eastern Finland
Department of Physics and Mathematics
P.O.Box 111
80101 JOENSUU, FINLAND
email: yuri.svirko@uef.fi

Professor Polina Kuzhir
University of Eastern Finland
Department of Physics and Mathematics
P.O.Box 111
80101 JOENSUU, FINLAND
email: polina.kuzhir@uef.fi

PhD Petri Karvinen
University of Eastern Finland
Department of Physics and Mathematics
P.O. Box 111
80101 JOENSUU, FINLAND
email: petri.karvinen@uef.fi

Reviewers:

Research Professor Zoran Ivic
Vinča Institute of Nuclear Sciences
Department of Theoretical and Condensed Matter Physics
P.O. Box 2208
11351 VINČA, BEOGRAD, SRBIJA
email: zivic@vin.bg.ac.rs

Professor Zhipei Sun
Aalto University
T411 Dept. Electronics and Nanoengineering
P.O. Box 1100
00076 AALTO, FINLAND
email: zhipei.sun@aalto.fi

Opponent:

Professor Ildiko Peter
George Emil Palade University of Medicine, Pharmacy, Science, and Technology of Targu Mures
Department of Industrial Engineering and Management
P.O. Box 1627
540139, TÂRGU MUREȘ, ROMANIA
email: ildiko.peter@umfst.ro

Anar Ospanova
Multipole approach in the invisibility and transparency problems.
Joensuu: Itä-Suomen yliopisto, 2024
Publications of the University of Eastern Finland
Dissertations in Science, Forestry and Technology; 57
ISBN: 978-952-61-5330-8 (print.)
ISBN: 978-952-61-5331-5 (PDF)
ISSNL 2954-131X
ISSN: 2954-131X (print.)
ISSN: 2954-1484 (PDF)

ABSTRACT

Nanophotonics studies light-matter interaction in the nanoscale. The Mie theory is sufficient to analytically calculate the electromagnetic scattering from nanoinclusions of the simplest spherical and cylindrical geometries and is capable to take into account the accompanying interference effects. However, in order to analyticaly describe an interaction of the electromagnetic waves with inclusions of more complex form and content that usually used in metamaterials one needs to perform multipole expansion of the optical response.

Generally, the electrodynamic effects in metamaterials can be described in terms of the excitation multipole moments in metaatoms, the simplest building blocks of the metamaterial. Resonances associated with shape and structure of metaatoms lead to the high-Q effects, which widely used in nanophotonic. Among such effects are the effect of electromagnetically induced transparency (EIT) often associated with Fano and Fano-type resonances, Kerker effect, anapole modes and cloaking as well as Bound State in Continuum (BIC). However, the observation of these effects has three major limitations associated with (i) dissipative (radiating) losses in metaatoms, (ii) radiation losses due to non-resonant scattering, and (iii) technological difficulties in the fabrication of meta-atoms especially in the optical frequency range.

In this Thesis we consider optical response of metaparticles (metaatoms) beyond conventional electric and magnetic dipole moments. This leads to new phenomena that may result in suppression of reflection and absorption of metamaterial, enable cloaking devices with reduced nonradiating losses and being suitable for fabrication. We will study electrodynamic effects associated with higher-order multipole moments of metaatoms and taking into account their interaction in terms of the so-called modified multipoles concept.

The Thesis objectives include

- development of the theory of modified multipoles that describe light scattering by metaatoms with a displaced or complex coordinate center;
- theoretical and experimental investigation of electromagnetic effects in complementary structures designed using the Babinet principle;
- observation of broadband transmission, transverse Kerker effect in the designed metamaterials and metasurfaces.

Achieving the project objectives implies resolving the following tasks:

1. To create the multipole expansion concept that takes into account the complex structure and mutual arrangement of metaatoms comprising metamaterial.
2. To develop a model of the scattering by a subwavelength dielectric particle of a spheroidal shape and to model its electrodynamic characteristics using the modified multipoles method.
3. To develop a theory of complementary Babinet metasurfaces demonstrating broadband transparency. To investigate the effects of asymmetry leading to high-Q resonances associated with Bound State in the Continuum (BIC) in complementary metasurfaces.
4. To experimentally observe transmission characteristics of Baabinet metamaterial in GHz range.

Keywords: metamaterials, multipole expansion, modified multipoles, Babinet principle, Kerker effect, Bound States in the Continuum, microwaves, THz, GHz

ACKNOWLEDGEMENTS

To begin with, I should thank my parents, honest and hard-working people who burned themselves to light my path. Without their efforts, I would not be here or anywhere else.

Thanks to my husband, my comrade Alexey Basharin, for all the blessings that I have now. Since God rewarded you with great patience, you had to meet a person who would test your patience, i.e. me. Thanks to my kids, Arsenii, Alan and baby girl Anna who illuminate my every day with heavenly light. Honestly, I cannot see any other reason to move forward.

Here I must thank my bachelor supervisor Prof. Askar Davletov for serving as an example of painstaking and careful work.

Thanks to my supervisors.

Petri Karvinen has great patience and the ability to repeat the same thing until it is fully understood. Thanks to Maria Cojocari for comprehensive assistance in research work.

Thanks to my friend and compatriot Maria Sinelnikova for always being with me and always standing up for me anytime and anywhere.

Thanks for Prof. Ladislau Matekovits for comprehensive support during the studies.

Professor Ildiko Peter, I really appreciate that you immediately responded to be my opponent and did everything to support me, including moral support on this path.

Professor Zoran Ivic and Professor Zhipei Sun, thank you for taking part in this agenda.

I would like to thank administrative staff of the faculty and the department for solving all organizational issues at the speed of light.

27 of August, Joensuu
Anar Ospanova

LIST OF ABBREVIATIONS

BIC	Bound State in the Continium
EIT	Electromagnetically Induced Transparency
SRR	Split Ring Resonators
ED	electric dipole
MD	magnetic dipole
TD	toroidal dipole
EQ	electric quadrupole
MQ	magnetic quadrupole
TQ	toroidal quadrupole
THz	Terahertz
GHz	Gigahertz

LIST OF ORIGINAL PUBLICATIONS

This thesis is based on data presented in the following articles, referred to by the Roman Numerals I-III.

I. A. Ospanova, M. Cojocari, and A. Basharin, ”Modified multipoles in photonics,” Phys. Rev. B 107, 035156 (2023).

II. M. M. Bukharin, V. Ya. Pecherkin, A. K. Ospanova, V. B. Il’in, L. M. Vasilyak, A. A. Basharin and B. Luk’yanchuk, ”Transverse Kerker effect in all-dielectric spheroidal particles,” Scientific Reports 12, 7997 (2022).

III. A. Ospanova, M. Cojocari, P. Lamberti, A. Plyushch, L. Matekovits, Yu. Svirko, P. Kuzhir, A. Basharin, “Broadband transparency of Babinet complementary metamaterials,” Appl. Phys. Lett. 122, 231702 (2023).

AUTHOR'S CONTRIBUTION

I) In paper I, author contributed to the conceptualization, was the maindriving force in electromagnetic simulations of shifted dipole moments.

II) In paper II, author contributed into the selection of model parameters and processed the simulation of multipole expansion of currents occurred in spheroid particles.

III) In paper III, author contributed to the task statement, carried out simulations and measured transmission characteristics, analyzed data and wrote the manuscript.

TABLE OF CONTENTS

1 BASIC DEFINITIONS AND CONCEPTS

1.1 Metamaterials and their electrodynamic properties

Metamaterials and metasurfaces are periodic structures comprising unit cells with a period and sizes much less smaller than the wavelength of the impinging electromagnetic wave. These unit cells are often called metaatoms by analogy with atoms in natural materials. The size of metaatom may vary from a few millimeters for microwaves to tens of nanometers in optics [1-23].

These metaatoms are building blocks of volumetric and planar structures reffered to as metamaterials and metasurfaces, respectively, which may possess properties not found in natural materials. Among such properties are negative refraction, the superresolution effect (overcoming the diffraction limit), and others [24-27].

1.1.1 Negative refraction

The first dive in to physical properties of metamaterials was associated with the excitation of backward waves. This kind effect can be observed in metamaterials with simultaneous negative indices of dielectric permittivity and magnetic permeability resulting in **negative refraction**, i.e. $n = \sqrt{-\varepsilon}\sqrt{-\mu}$. For the first time, the possibility of the existence of wave processes in matter, where the phase and group velocities are directed oppositely, was noted by G. Lamb in [28]. Almost simultaneously, it was shown in [29], that in backward waves supporting medium, a radiation source excites converging waves. These works had not been paid attention in that time and the further investigation on backward waves was published only 40 years later by Mandelstam, furthermore, existence of negative refraction was first predicted [30]. D.V. Sivukhin showed in [31] that in media with negative values of dielectric ε and magnetic μ permeabilities, the group and phase velocities of the wave are directed oppositely. Such waves have a negative phase velocity, however their group velocity that is responsible for the speed of energy propagation in the medium, is still directed out from the source. Next work in the study

of negative refraction of light was published by V. G. Veselago in 1967 and made a revolution in electrodynamics [32]. In this work, Veselago proposed the idea of a lens made from a plane-parallel layer of material with values $\varepsilon = \mu = -1$, enabling the focusing the image in front of the object. Moreover, there was proved that the components of electric ***E*** and magnetic ***H*** field and the wave vector ***k*** form a left-hand triple of vectors (Figure 1.1.1). This paper faced the same fate as ahead of their time da Vinci's works, thus, the first reference on it was made only 30 years later. In his revolutionary paper, J. Pendry [21] showed that the lens proposed by Veselago can create an image of a source scaled less than wavelength without distortion, i.e. not limited by the diffraction limit (Figure 1.1.2). Afterwards, in scientific society such a lens was called a superlense. According to Pendry, this effect is due to the wave, exponentially decaying in analogy with evanescent in a conventional optical medium, are amplified in a medium with negative values of dielectric ε and magnetic μ permeability. Based on these studies, the first super-resolution experiment was carried out in 2003 [33, 34].

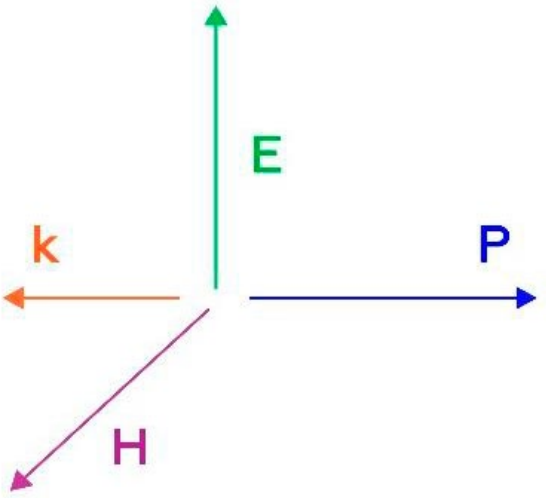

Figure 1.1.1. Illustration of the left-hand system of wave vector ***k*** and electric ***E*** and magnetic ***H*** components of an electromagnetic wave. Here, **P** is the Pointing vector

As for the fabrication of negative refraction materials, i.e. materials with negative values of ε and μ, this direction has turned into an independent branch of science and is actively developing to this day. It is worth noting that materials with negative values of ε and μ were developed and used long before Pendry's seminal paper. For example, noble metals like gold, silver, and others possess a negative dielectric constant in the optics and infrared ranges, while ferromagnetic resonance in specific microwave range usually lead to negative magnetic μ permeability. However, in optics, the relative magnetic permittivity of the vast majority of natural materials is close to unity, i.e. achieving negative refraction in optics is possipble only in the metamaterial paradigm.

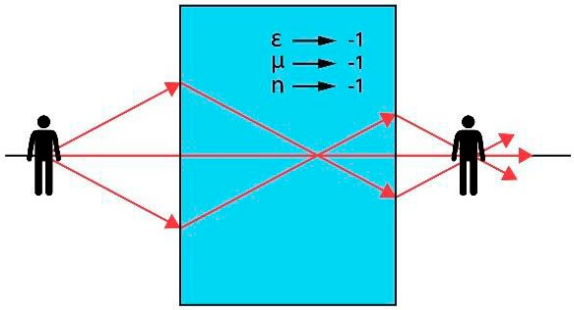

Figure 1.1.2. Schematic illustration of Veselago proposed lense

In metamaterials targeting negative refraction the key role is usually played by a split-ring resonator (SRR), a broken conductive ring having a gap narrower than the wavelength. An external electromagnetic wave induces currents in such a ring leading to negative magnetic permeability of the ensemble of such rings in the vicinity of the resonance [35-37]. The idea of creating such a structure was firstly proposed by Shchelkunov and Friis [38] and published in 1952, where primary purpose was to optimize the antenna performance. In the first studies, it was considered to implement negative values of dielectric ε and magnetic μ permeability separately. Furthermore, experimental studies of metamaterials made from metal microwires were performed in [39]. Here, two microwires of different lengths provided two

microwave resonances, i.e. the composite material demonstrated two negative minima in the dielectric permittivity spectrum. Experimental data on the study of structure of bifilar spiral inclusions with negative values of dielectric ε and magnetic μ permeability were given in [40].

1.1.2 Superresolution

The study and development of these inclusions has contributed greatly to study of **superresolution** effect – overcoming the diffraction limit in imaging sustems. The necessity of low loss metamaterials for superresolution was emphasized in [41-47]. Since ohmic losses can be significantly reduced in thin Veselago lenses [46], metamaterials were considered to achieve the super-resolution in real conditions. The interaction between electromagnetic wave with an ordinary lens or with an ordinary transparent material associated with the problem of exponential attenuation of evanescent waves that determines characteristics of less than wavelength particles, i.e. less than the diffraction limit. Thus, only harmonics whose wavelength is greater than the wavelength of light reach the focal region of a conventional lens, and, on the contrary, harmonics with larger wave numbers are attenuated in the source region, thus, it is not possible to focus the response from all parts of the object into the focal region.

In order to create an ideal image with the lens, the propagating and evanescent waves in the focal region should have the same amplitudes and phases as in the source region. In his theoretical work, Pendry have demonstrated that damped evanescent harmonics in a layer of negatively refractive metamaterial, i.e. Veselago lens, begin to increase exponentially toward the edge of the layer farthest from the source, i.e., to amplify resonantly. In the case of a metamaterial with $\varepsilon = \mu = -1$, the relationship between the amplitudes of the propagating and damped waves is restored exactly at the focus, resulting in an accurate image of the object, not distorted by the diffraction limit. On this base, one can admit that Veselago-Pendry lens is defined as an optical device for transmission propagating waves without distortion and amplifying harmonics with imaginary propagation coefficients, thus, maintaining the necessary phase relationships.

One of the successful implementations of a superlens was demonstrated in [46]. Here, the flat lens was exploited for demonstration of superresolution effect in metamaterial consisted of a metamaterial comprising multidirectional spiral turns and conducting wires. This effect appeared due to the concentration of field energy at the far wall of a plane-parallel layer of metamaterial [34, 48].

1.1.3 Strong localization

The effect of *strong localization* of an electromagnetic field in metamaterials is associated with great expectations for the creation of high-quality open subwavelength resonators that able to concentrate fields in dimensions significantly smaller than a wavelength of incident electromagnetic wave. In addition, highly localized electromagnetic fields are widely used to observe nonlinear effects in the optical and microwave spectral ranges [49]. The problem of creating of miniature high-Q resonators is also awaited in the field of high-power lasers, where geometric dimensions of the resonators must be at least half the wavelength of light. However, metamaterials and individual metaatoms are capable lasing even from a single subwavelength metaatom. Arrays of plasmonic nanoparticles [50-53] and nanoholes [54-57] have been proposed to function as resonators for plamons and gave birth to spasers. A number of metamaterials such as butterfly antennas [58], U-shaped cavities [59] and V-shaped optical resonant antennas [60] are capable of localizing an electric field in a narrow gap during interaction with an external electromagnetic wave, thus creating applications for such optical resonant nano-antennas in nonlinear optics [61-64], near-field scanning microscopy applications [65, 66], as well as Raman spectroscopy [67], etc [68]. On the other hand, some nanostructures have been proposed for amplification and localization magnetic field of nanostructures, such as diabolo nanostructure [69], cross-diabolo nanoantenna [70], etc [71].

Nowadays, metamaterials find application in entire frequency range, however, the use of metamaterials in the attractive optical range is still limited both technologically and due to dissipative and radiation losses.

The implementation of optical metamaterials is important for biological research [39, 63, 65, 66, 72], for controlling visible light [73-76], in medicine and other applications [9, 77, 78]. Often, for cloaking and superresolution

effects that are important at optical frequencies, the use of metamaterials is the only direct solution.

1.2 Invisibility and transparency phenomena of metamaterials

1.2.1 Cloaking effect

The **cloaking** phenomenon, also referred to as camouflage effect, has attracted a widespread attention of the general public mainly due to Harri Potter's invisibility hat. In the scientific literature, this effect was first realized by J. Pendry, however, the idea of invisibility mulled a long ago [38]. Inspired by mathematical calculations of Ulf Leonhardt [79, 80], Pendry and co-authors proposed a fundamentally new masking method - transformation optics (TO) [81, 82]. This theory was based on the curvature of incident wavefront on a masking coating that forces light fold around the object and then returns to original route. For external observer, this kind light propagation can be judged as free propagation without obstacles, and one cannot be able to record any distortion of the wave front. This can be achieved according to specific condition, stating that path length through the shell must coincide with the free path length for each ray.

Although a variety of cloaking coatings have been developed, they rely on either wave flow phenomenon or scattering compensation.

Cloaking based on the wave flow phenomenon holds for the object hidden inside a shell, causing electromagnetic waves to bend around the object and afterward restore the wave front and intensity distribution (Figure 1.2.1). The electromagnetic properties of the cloaked object do not impede the interaction between cloaking shell and impeding wave. Cloaking coatings are often relying on transformation optics that has a base on the invariance of Maxwell's equations with proper transformation of dielectric ε and magnetic permeability tensors [83]. The first experimental work on cloaking surfaces was carried out on the basis of various inclusions, such as split ring resonators (SRR), canonical spirals, and others [84, 85]. The first experimental implementation of a two-dimensional metamaterial-based cloaking device in

the microwave range was carried out on the base of theory published in [84] in 2006. Another widely used method is carpet camouflage coatings based on transformation optics and wave flow processes [86-89].

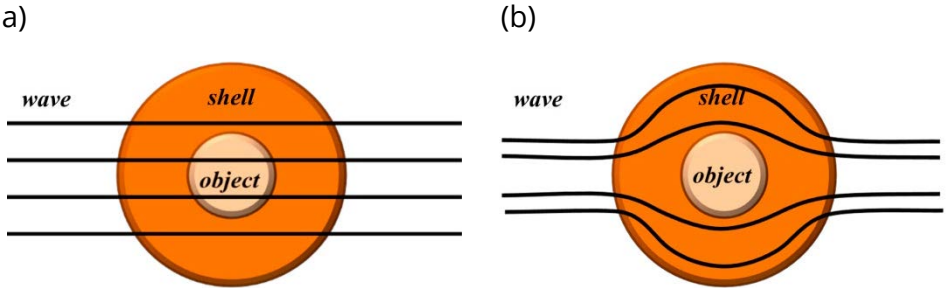

Figure 1.2.1. Illustration of cloaking effect on the base of wave flow processes. The object is hidden inside the shell interacts with impinging wave (a), while cloaking shell covers the objects and prevents the interaction with external impinging waves.

Cloaking on the base of scattering compensation can be understood by mutual compensation of wave scattering between cloaking coating and cloaked object itself, thus providing wave path with suppressed non-radiative losses.

In the framework of this approach, in order to suppress scattering from one object, one need to excite scattering from another object that would possess the same amplitude and oscillates in antiphase [15, 90-92]. This type of cloaking includes plasmon cloaking and mantle cloaking. The idea of plasmon cloaking is to place an object in a shell made of noble metals (gold, silver, aluminum) with negative dielectric constant. The dipole moment of the shell oscillates antiphase with respect to the vector of the object's dipole moment (Figure 1.2.2) [93-98].

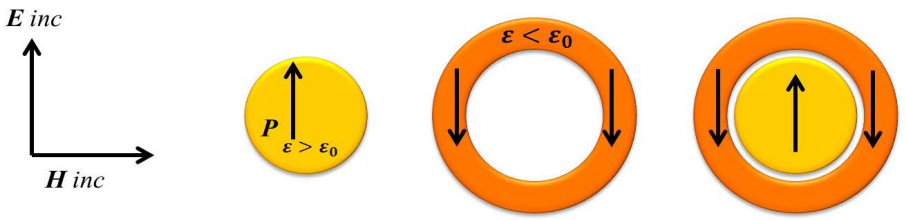

Figure 1.2.2. Cloaking effect on the base of scattering compensation in case of incident plane wave. The effect is based on destructive interference of electromagnetic fields between hidden object (yellow) and covering shell (orange).

The method of mantle cloaking based on suppressing the field scattered from an object using surface currents induced on metasurfaces, i.e. mantle. Incident wave excites surface currents on the metasurface resulting on scattering that oscillates in antiphase with the field scattered from the object. This results on destructive interference leading to the elimination of backscattering from the cloaked object [99-106].

The interest on study of invisibility effects in optical range is underpinned by important applications in biology and medicine. Nanoscale metamaterials and metasurfaces are used in the diagnosis and therapy of various diseases as well as in various biological studies. One prominent example is the therapy and imaging of cancerous tumors. Standard chemical therapy kills both cancerous and healthy cells in the body. Many laboratory studies have demonstrated the possibility of diagnosing and treating cancer through the use of nanoparticles. As a result of biological and physical processes, metal or metal-dielectric nanoparticles attach to the surface of cancer cells or get inside them. This infected area is irradiated in the near-infrared (IR) range, the scattered radiation from which makes it possible to visualize the tumor. In addition, sufficiently strong radiation locally heats nanoparticles up to 700^0C due to plasmon resonance, which leads to the death of cancer cells. Here, gold nanoparticles, single-walled nanotubes, ferromagnetic nanoparticles, and others can be used as nanoparticles [107-112]. In diagnostics, nanoparticles can act as biosensors. To date, a large number of methods have been

proposed for creating biosensors based on surface and localized plasmons [113-123] as further application of scattering effects from nanoparticles.

1.2.2 Bound State in the Continuum

The recent fascinating manifestation of electromagnetic properties of metamaterials is the Bound State in the Continuum (BIC) phenomenon, which manifests itself as coexistence of well defined eigenmodes with leaked waves that constantly leak energy away [124, 125]. Importantly, BICs are fundamentally differs from well-known resonances that leak out (see Figure 1.2.3 redrawn from [125]). These leaky modes can be defined as complex frequency , where is the resonance frequency and γ is leakage rate. In contrary, leakage rate BICs, which co-exists with these leaky modes, is negligible, i.e. and Q-factor of the system tends to infinite values. BICs can be considered as a special case of trapped mode [126]. BICs are excited via small variation of the system parameters and - depending on the parameters used - are referred to as symmetry-protected [127-133], parametric [134-137], accidentally BICs [138, 139]. The most illustrative symmetry-protected BIC effect is tied to symmetry of the system. Since it occurs in high-symmetry periodic structures (e.g. in photonic crystals [140]), metamaterials are suitable environment to observe such BICs [141, 142].

Each metaatom forms individual scattering response from local interaction with incident wave and contributes to overall scattering response from the whole metamaterial. Furthermore, metamaterials are good playground for wavefront engineering as well as beamshaping whereas response of metaatoms is defined by their parameters [143].

Metamaterials are also high-symmetry structures and can serve as platform for investigation of effects occurring due to small parametric changes causing BICs. One should mention methods for asymmetry introducing, such as defect of the system. A small fracture in metamaterial or metasurface can be considered as coupling parameter of bound state “resting” in the continuous spectrum to the leakage channels of the continuous spectra carrying energy away [129]. As a result, one can see high quality factor resonance of dielectric resonators in micron range. Here we should count methods on asymmetry introducing, such as Fabry-Perot BICs [134, 136], separable BICs [144], BICs

from inverse construction [145, 146] and others. The most spectacular example among them is symmetry protected BICs of (in-plane) asymmetry introduced by changing of incidence angle of electromagnetic wave. Ref. [147] has demonstrated such effect with the use of photonic crystal slab. The BICs in photonic crystal have been explained as vortices in the field of polarization and demonstrated in the term of conserved topological charges. It was established that the most robust BICs appears due to topological defects in corresponding parameter spaces. Importantly, Ref. [132] have developed very elegant theory explaining the emergence and development of the BIC effect due to the change of in-plane asymmetry parameter , where is the angle of asymmetry (see Figure 3 b for examples). Another intelligible investigation of symmetry protected BIC is based on altered angle of incidence is given in Ref. [128]. Here, authors have declared a photonic slab of arranged holes to demonstrate the high Q resonances (up to 1 000 000) due to release of BIC mode by means of introducing significant in-plane asymmetry. Moreover, authors have discussed the design of silicon nitrate thin film with a period 340 nm and demonstrated high Q resonance at large tilt of angle of incidence of about 35^0 in optical range.

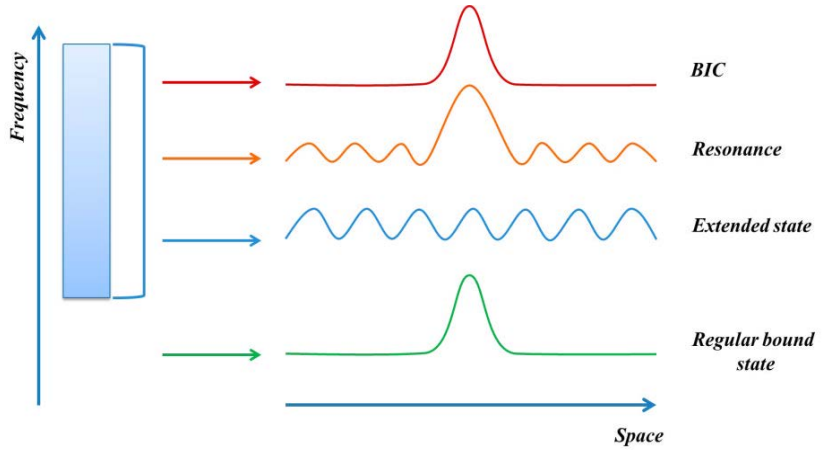

Figure 1.2.3. Schematic illustration of BIC excitation. The figure is redrawn from [125].

1.3 Multipole expansion and their main characteristics

1.3.1 Multipolar nonradiating effects in metamaterials: Fano resonances, Kerker effect, anapole states

The study of the electromagnetic properties of metamaterials and metasurfaces conventionally employs multipole approach when the the electromagnetic field is presented in terms of the dynamic multipoles created in the metaatoms by the incident radiation. The interference of radiation procused by these multipoles gives rise to the reflected and transmitted waves, which can be controlled by manipulating the shape and mutual arrangement of metaatioms in the subwavelength [1, 21, 42, 148-152, 153-184]. The multipole presentation of the scattered electromagnetic wave implies expansion of the induced current in series of , when is the characteristic size of the metaatom, is the wavelength, and often require taking into account not only the electric and magnetic dipole moments but also their higher-order counterparts (quadrupoles, octopoles, and so on) [185-187]. It is worth noting that there is a common belief that in metamaterials, the toroidal moments, which have been overlooked in electrostatics-inspired multipole expansion, may also play important role [27, 185-187].

Multipole analysis enables decomposion of the scattered electromagnetic wave in terms of multipoles and also allows one to design the metaatoms with prescribed characteristics. For instance, by using multipole expansion one can design a metaatom that possesses nearly zero scattering cross section (anapole mode) when the radiation of dipoles of electric and toroidal types cancel each other in the far-field. Generally speaking, this method makes it possible designing metaatoms with peculiar scattering properties allowing engineering of the electromagnetic field in the far- and near zones.

In the Thesis, we describe the electromagnetic wave scattered (radiated) by an metaatom in the far zone in terms of multipoles of electric, magnetic and toroidal family [16, 150, 188]. A schematic representation of these three types of multipoles as well as their patterns of far-field radiation are shown in Figure 1.3.1. As we can see, the radiation patterns of the electric, magnetic and toroidal dipoles coincide with those of conventional Hertz oscillator, current loop and the vortex of the magnetic field exciting from circular currents,

respectively. Since the radiation patterns of quadrupoles and octupoles are more complicated, one can design various emission patterns by enhancing or suppressing particular multipole moments of the metaatoms.

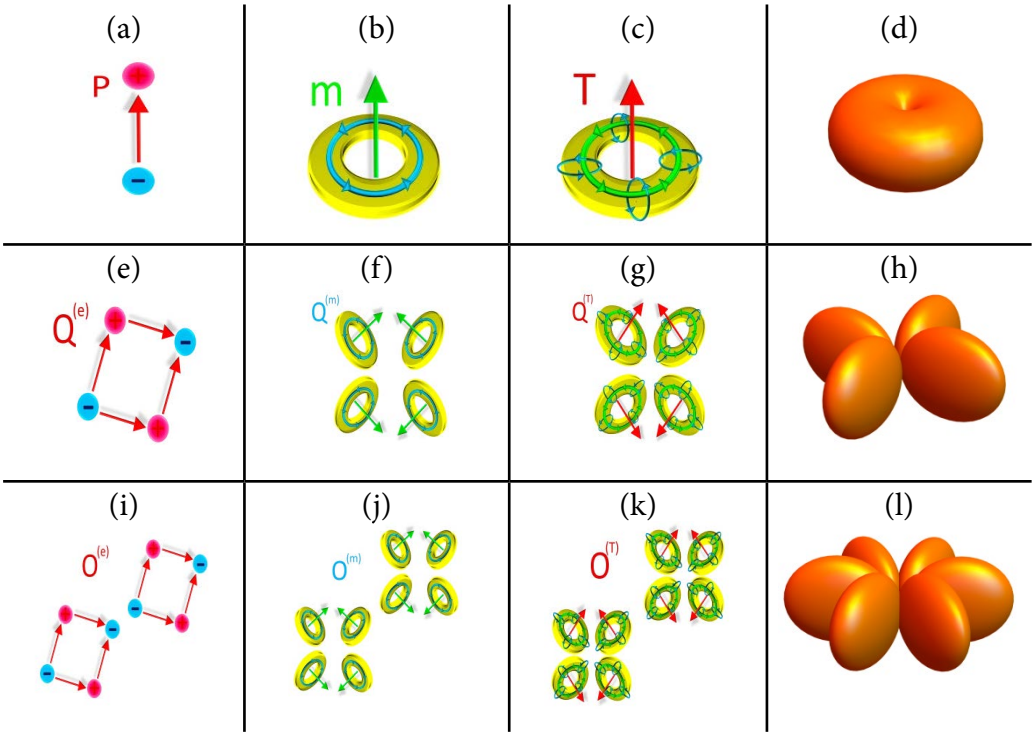

Figure 1.3.1. Schematic representation of electric, magnetic and toroidal multipoles up to octupole order and their radiation patterns [178]. The scheme shows the mechanism of excitation of dipoles of electric (a), magnetic (b), toroidal (c) families as well as their radiation pattern. The same colored scheme is presented for quadrupoles (e-h) and for octupoles (i-l).

To obtain the equation for an electric field produced by the array of multipoles, one can use the expression derived from the radiation emitted by the individual multipole sources as determined by Radescu and Vaman [169]. According to these equations, it is pragmatic to expand these series into various orders of *l*. Consequently, the *l* = 1 subseries comprises the contributions of the dipolar nature.

$$\mathbf{E}_{(l=1)} \approx \frac{\mu_0 c^2}{3\sqrt{2\pi}} \frac{\exp(-ikr)}{r} \times \sum_{m=0,\pm1} \Big[\Big(k^2 Q_{1,m} - ik^3 T_{1,m} + ik^5 T_{1,m}^{(1)} \Big) \times \big(\mathbf{Y}_{1,2,m} + \sqrt{2}\mathbf{Y}_{1,0,m} \big) + i\sqrt{3} \Big(k^2 M_{1,m} - k^4 M_{1,m}^{(1)} \Big) \times \mathbf{Y}_{1,1,m} \Big]. \quad (1.3.1.1)$$

The $l = 2$ subseries comprises the quadrupolar contributions:

$$\mathbf{E}_{(l=2)} \approx \frac{\mu_0 c^2}{10\sqrt{6\pi}} \frac{\exp(-ikr)}{r} \sum_{m=0,\pm1,\pm2} \big[\big(ik^3 Q_{2,m}^{(e)} + k^4 Q_{2,m}^{(T)} \big) \times \big(\sqrt{2}\mathbf{Y}_{2,3,m} + \sqrt{3}\mathbf{Y}_{2,1,m} \big) - \sqrt{5} k^3 Q_{2,m}^{(m)} \mathbf{Y}_{2,2,m} \big]$$

The $l = 3$ subseries contains the octupolar contributions:

$$\mathbf{E}_{(l=3)} \approx - \frac{\mu_0 c^2 k^4}{15\sqrt{3\pi}} \frac{\exp(-ikr)}{r} \times \sum_{m=0,\pm1,\pm2,\pm3} \Big[\frac{1}{7} O_{3,m}^{(e)} \big(\sqrt{3}\mathbf{Y}_{3,4,m} + 2\mathbf{Y}_{3,2,m} \big) + \frac{i}{\sqrt{7}} O_{3,m}^{(m)} \mathbf{Y}_{3,3,m} \Big].$$

The total field emitted by multipoles is shown as

$$\mathbf{E} = \mathbf{E}_{(l=1)} + \mathbf{E}_{(l=2)} + \mathbf{E}_{(l=3)} + (l > 3 \text{ subseries }).$$

From this definition, we can see possible interference of electric and magnetic types of radiation. For clarity, an electric dipole may interfere with a toroidal dipole, which belongs to the same family of radiation. On the other hand, an electric dipole can interfere with a magnetic dipole, which leads to the Kerker effect [16].

For clarification, here we demonstrate the arbitrary shaped structure of the volume V and occurring within this volume currents j (Figure 1.3.2).

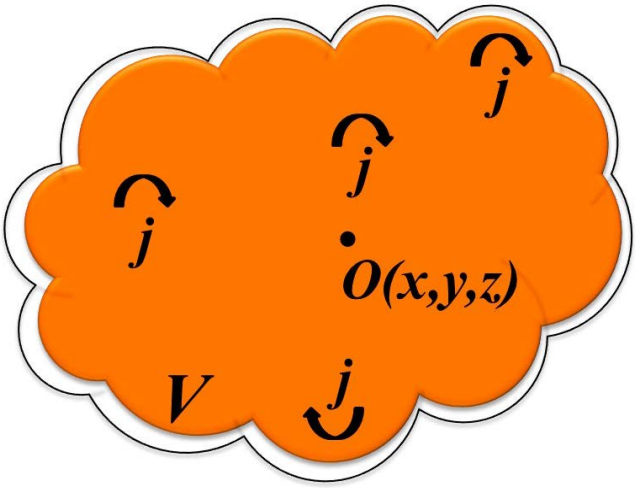

Figure 1.3.2. The illustration of metaatom of volume V and currents j occurring within it

A complete list of multipole moments up to the magnetic octupole, as well as their radiation intensity, is given below:

(1.3.1.2)

$$P_\alpha = \int \frac{\mathrm{i}}{\omega} \mathrm{d}^3\mathrm{r}\, \mathrm{j}_\alpha$$

$$\mathrm{M}_\alpha = \tfrac{1}{2\mathrm{c}} \int \mathrm{d}^3\mathrm{r} [\mathbf{r} \times \mathbf{j}]_\alpha$$

$$\mathrm{T}_\alpha = \frac{1}{10\mathrm{c}} \int \mathrm{d}^3\mathrm{r} [(\mathbf{r} \cdot \mathbf{j})\mathrm{r}_\alpha - 2\mathrm{r}^2 \mathrm{j}_\alpha]$$

$$T_\alpha^{(1)} = \tfrac{1}{28\mathrm{c}} \int \mathrm{d}^3\mathrm{r} [3\mathrm{r}^2 \mathrm{j}_\alpha - 2\mathrm{r}_\alpha (\mathbf{r} \cdot \mathbf{j})]\mathrm{r}^2,$$

$$\mathrm{Q}_{\alpha,\beta}^{(\mathrm{e})} = \frac{1}{2\mathrm{i}\omega} \int \mathrm{d}^3\mathrm{r} \left[\mathrm{r}_\mathrm{a} \mathrm{j}_\beta + \mathrm{r}_\beta \mathrm{j}_\alpha - \frac{2}{3} \delta_{\alpha,\beta} (\mathbf{r} \cdot \mathbf{j})\right]$$

$$\mathrm{Q}_{\alpha,\beta}^{(\mathrm{m})} = \frac{1}{3\mathrm{c}} \int \mathrm{d}^3 [\mathbf{r} \times \mathbf{j}]_\alpha \mathrm{r}_\beta + \{\alpha \leftrightarrow \beta\}$$

$$\mathrm{Q}_{\alpha,\beta}^{(\mathrm{T})} = \frac{1}{28\mathrm{c}} \int \mathrm{d}^3\mathrm{r} \left[4\mathrm{r}_\alpha \mathrm{r}_\beta (\mathbf{r} \cdot \mathbf{j}) - 5\mathrm{r}^2 \left(\mathrm{r}_\mathrm{a} \mathrm{j}_\beta + \mathrm{r}_\beta \mathrm{j}_\alpha\right) + 2\mathrm{r}^2 (\mathbf{r} \cdot \mathbf{j}) \delta_{\alpha,\beta}\right]$$

$$O^{(e)}_{\alpha,\beta,\gamma} = \frac{1}{6i\omega}\int d^3r\left[j_\alpha\left(\frac{r_\beta r_\gamma}{3} - \frac{1}{5}r^2\delta_{\beta,\gamma}\right) + r_\alpha\left(\frac{r_\gamma j_\beta}{3} + \frac{r_\beta j_\gamma}{3} - \frac{2}{5}(\mathbf{r}\cdot\mathbf{j})\delta_{\beta,\gamma}\right]\right.$$

$$+\{\alpha \leftrightarrow \beta,\gamma\} + +\{\alpha \leftrightarrow \gamma,\beta\}$$

$$O^{(m)}_{\alpha,\beta,\gamma} = \frac{15}{2c}\int d^3r\left(r_a r_\beta - \frac{1}{5}r^2\delta_{\alpha,\beta}\right)[\mathbf{r}\times\mathbf{j}]_\gamma + \{\alpha \leftrightarrow \beta,\gamma\} + +\{\alpha \leftrightarrow \gamma,\beta\}$$

where $\alpha,\beta,\gamma=\{x,y,z\}$. These expressions in (1.3.1.2) are given in the Cartesian coordinate system.

Multipole interaction occurs both between multipoles of the same type (for example, electric dipole and quadrupole) and between multipoles of different types (electric and magnetic or toroidal dipoles).

Interaction between electric type multipoles. In nanophotonics, to the study of the interference of electric multipoles has been paid more attention whereas the study of magnetic and toroidal multipoles has been developed relatively recently [1, 21, 189]. As a result, studies were carried out predominantly on the electric response, neglecting the magnetic one, in particular in the optical range, where magnetic dipole moments do not occur. The electric dipole (ED) moment arise as a result of the interaction of two oppositely charged charges in a unit volume.

Composite of multiple EDs with tunable amplitudes and phases enable the formation of directional and narrow radiation patterns for many nanophotonics applications such as sensors, nanoantennas, as well as photovoltaic devices [153, 190-193]. Generally, the effect of such combinations is underpinned by properly chosed phase difference and bias between these pairs, leading to constructive enhancement of scattering in one direction due to the “accumulation” of phases due to the difference in optical paths. More complex combinations of EDs lead to a change in the direction of propagation of surface plasmon-polaritons (SPP) modes that was excited by an impinging circularly polarized wave [194]. The couplement of EDs can be used as well to form radiation patterns of point sources [195, 196] and for tunable metasurfaces [158, 197, 198].

The basis of ED interference can spand to high-order electric multipoles, whose the simplest case is the spatial overlap of the electric dipole and electric quadrupole (EQ) modes. The playground for such interference is Mie

scattering by sphere-shaped particles with an impinging planar polarized wave [199]. The analysis of parity shows that electric dipoles and quadrupoles may interfere constructively and destructively resulting in scattering in the forward and backward directions, respectively [8, 154].

Here, ***Fano resonances*** are of great interest since they are precisely described via interaction of multipoles of both the same kind of different order as well as multipoles of different types [3, 22-26, 148, 200, 201, 202-205]. Fano resonance is inherent to quantum systems and occurs due to the superposition of two eigenmodes: narrow or so-called bright mode, and subradiative broad or so-called dark mode [205, 206]. Spectral superposition of these two modes leads to high-Q asymmetric transmission peak known as Fano resonance. For the first time, the Fano resonance in metamaterials was studied in an array of asymmetric SRR rings [148]. Here, microwave radiation excites antisymmetric currents in both parts of the broken ring leading to excitation of magnetic MD dipoles perpendicularly directed to the surface of the metamaterial. This magnetic dipole acts like subradiative mode that interferes with the external, wider superradiative electric mode, resulting in a classical Fano resonance. Fano resonances can be also generated via interference of the Mie dipole and the quadrupole modes also resulting in their interference [202]. This interference may result both in the enhancement of electromagnetic field intensity in the far-field, i.e. constructive interference or its suppression, i.e. destructive interference [205, 206]. In case of particles with sizes larger compared to wavelength, higher-order multipoles can interfere with the dipole mode of broader range and excite higher-order Fano resonances [22].

Interaction between magnetic multipoles. All principles for interactions of electric multipoles, by considering the parity of Maxwell's equations, can be directly compared with magnetic multipoles. The magnetic response of a system is of great importance in nanophotonics [21, 189], both in traditional plasmonic and all-dielectric structures [152, 153, 207] for the formation of optical magnetism and so-called magnetic light [208].

Magnetic Fano resonance is observed in all-dielectric nanoparticles as well [155, 156,163], that is alike electric Fano resonance observed in metal particles [22, 23, 157].

Interaction between electric and magnetic multipoles. As it is established in nanophotonics, the presence of a magnetic type of response provides an additional degree of freedom for more effective control of light by simultaneous electric and magnetic multipoles in metaparticles [152, 153, 159, 207].

One of the outstanding demonstration of the simultaneous intensification of forward scattering as well as suppression of backward scattering on the base of interference of electric and magnetic multipoles often referred to as the ***Kerker condition*** (Figure 1.3.2) [27, 28, 198, 81,153, 159, 160]. In continuous media, this condition implies $\varepsilon=\mu$, however, in the optical range, dinding such a materials is a difficult task because magnetic permeability at optical frequencies is close . However, comparable cross sections of the electric and magnetic dipole scattering can be achieved for dielectric nanoparticles. This was first demonstrated for a silicon nanoparticle in the optical frequency range [160].

(a) (b)

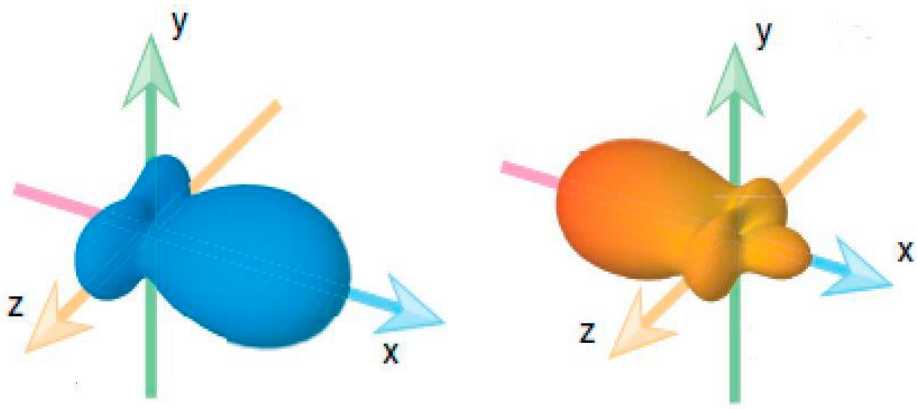

Figure 1.3.2. Schematic illustration of forward (a) and backward (b) Kerker conditions. Incident wave supposed to be planar wave which ***k*** vector propagating along ***x***-axis

Special attention should be paid for electromagnetic-induced transparency (EIT), arising as a result of the interaction of multipoles of different types by analogy with the quantum effect in three-level atomic systems [209, 210].

For the first time, the classical analogue of ***EIT*** was reproduced in metamaterials [180]. The spectral overlap of two modes of the same

resonant frequencies leads to the appearance of a narrow high-Q peak in the transmission spectrum, the so-called transparency window, resulting in transparency at given frequency. The establishment of EIT enables the application of light retardation systems and open high-quality resonators [211, 212].

Interaction of electric and toroidal dipoles and multipoles. Although dynamic type of toroidal multipoles play a significant role in an expansion of current distributions [213, 214], their extensive research began with the recent exhibition of toroidal dipoles in metamaterials [16]. In particular, this is due to the fact that far-field radiation patterns of electric and toroidal dipoles (TDs) coincide [214]. Simultaneously, the classical multipole expansion is typically conducted for configurations of charges and currents with propagation area significantly smaller than the effective wavelength of light, omitting the contributions of toroidal multipoles [213, 215]. The unique interaction between electric and toroidal moments results in ***anapole states***, which exhibit the suppression of all types of multipolar radiation, leading to complete invisibility. Specifically, the toroidal dipole moment $\boldsymbol{T}$ shares similar far-field characteristics with the electric dipole moment $\boldsymbol{P}$, allowing for destructive interference between them in the far-field under the condition that $\boldsymbol{P} = i k \boldsymbol{T}$, where i represents the imaginary unit and k is the propagation wave vector.

1.4 The Babinet principle and properties of Babinet surfaces

Babinet's principle is one of the fundamental effects of electrodynamics. Being a consequence of the duality of Maxwell's equations, it can be employed to simplify the diffraction problem solution. In simple terms, if we have found the field diffracted by a planar opaque object, we can easily find out the diffracted field by a hole of the same geometric shape in an opaque plane [216]. Let us clarify it with an example.

We assume two complementary screens with surface impedances $\boldsymbol{Z}_{oS}(x,y)$ and $\boldsymbol{Z}_{cS}(x,y)$ placed in a vacuum (Figure 1.4.1). The first, so-called original screen ("oS") is a metallic chessboard-shaped mirror, while the second,

complementary (“cS”) one is a similar metal mirror with vice-versa position of holes of the same size.

The oS is illuminated by planar polarized wave with electric ***E****(in)* and magnetic ***H****(in)* components that are partially reflected from it and partially transmitted through it, thus ***E****(in)*=***E****(ref)*+***E****(tr)*, ***H****(in)*=***H****(ref)*+*H(tr)*. The cS is illuminated by incident wave with electric ***E****c(in)* and magnetic ***H****c(in)* components that are

$$\boldsymbol{E}_c(in) = \boldsymbol{E}_c(ref) + \boldsymbol{E}_c(tr), \qquad (1.4.1)$$

$$\boldsymbol{H}_c(in) = \boldsymbol{H}_c(ref) + \boldsymbol{H}_c(tr).$$

A more detailed derivation of the expressions is given in works of Yoshiro Urade in [219-224].

One can conclude that “oS” and “cS” are related to each other since cS is radiated by dual component of field transmitted from oS that results in transmission properties of Babinet structures as follows:

$$\frac{E(t)}{E(in)} + \frac{E_c(tr)}{E_c(tr)} = |t_1|^2 + |t_1^c|^2 = 1, \qquad (1.4.2)$$

that represents energy conservation relation. Here, and transmission coefficients of original and complementary surfaces.

Basically, Babinet principle has found its place in antenna application and nowadays it is widely used for designing problems [217-225]. One of the spectacular applications of Babinet principle treatment can be found in medicine. Here the size of blood cells can be found by comparison with diffraction pattern with an array of small holes.

(a)

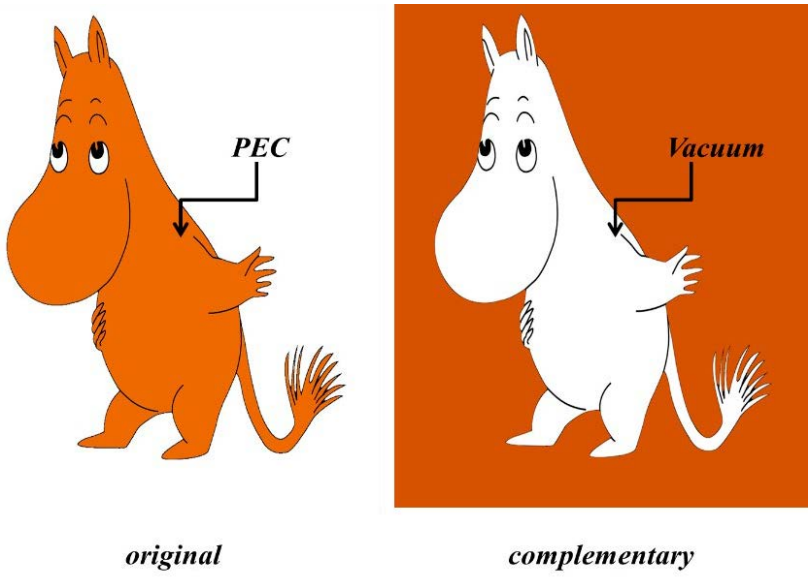
PEC
Vacuum
original
complementary

(b)

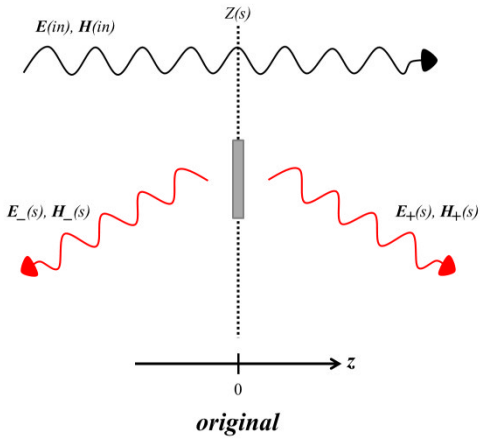
E(in), H(in)
Z(s)
E_(s), H_(s)
E+(s), H+(s)
z
0
original

(c)

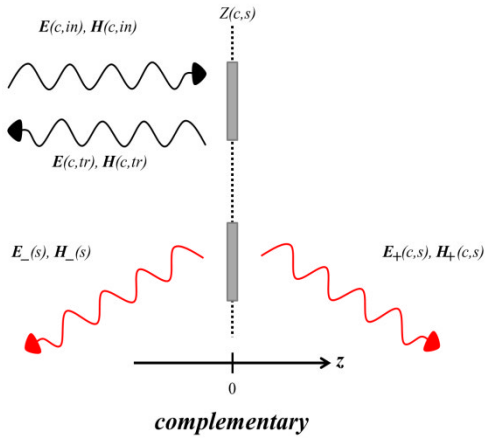

Figure 1.4.1: Graphical representation of Babinet structure and their field distribution

In Figure 1.4.1 the mechanism of complementary Babinet structure is thoroughly illustrated. Here we can see the simplest illustration of complementary Babinet pettern, where we suggest colored part to be metallic and non-colored part to be vacuum. In Figure 1.4.1 (b) and (c) we demonstrate the interaction of the structure with external electromagnetic wave. The incident electromagnetic wave splits as reflected and transmitted wave when it goes through the first layer. In turn, that transmitted from the first layer wave in turn splits as transmitted and reflected waves as well. The sum of transmitted from both layers waves restores the pattern of the original wave.

2 MODIFIED MULTIPOLE OF SHIFTED STRUCTURES

The utilization of the multipole expansion technique holds significant promise as a valuable instrument for manipulating the radiation or scattering characteristics in engineering applications. Its efficacy remains evident even when confronted with complex and composite scatterers, including multilayer particles, clusters, or systems with intricate structures composed of distinct components. Traditionally, the radiation fields originating from point magnetic or electric sources are primarily expanded into either electric or magnetic dipole moments. Nonetheless, it is crucial to emphasize that physical sources can be precisely represented by a sequence of multipoles, encompassing higher order multipoles and toroidal moments. Within this section, we present the notion of adapted multipoles that precisely portray the attributes of genuine sources, specifically electric, magnetic, and toroidal varieties. Through the utilization of analytical formulations of primary multipoles, we explore their reliance on both the position of the radiation focal point and the displacement of the source concerning the coordinate center. The inclusion of our adjusted dipole method proves to be indispensable for the multipoles examination of intricate systems within the realm of photonics, such as clusters of nanoparticles, metamaterials, and nanoantennas. Furthermore, it contributes to advancing our understanding of toroidal electrodynamics.

2.1 The alteration of multipole expansion due to the shift of coordinate center

The extensively examined matter in multipole analysis of metamaterials and metaparticles involves determining the radiation center of the multipoles. Even in the scenario of a relatively uncomplicated Split Ring Resonator (SRR) where the geometric center no longer aligns with the ring's center, the selection of the origin significantly influences the multipole series.

It has been illustrated and thoroughly deliberated in a Ref. [226] that multipole moments, excluding zero-order multipoles, are dependent on the choice of origin similar to how lower order multipoles impact the modification of the higher order multipoles. Whenever a low-order multipole moment is not zero, the shift in the origin results in the modification of the multipole moments of higher order [227, 228]. This implies that multipole series is not unque because it depends on the positioning of a source with respect to the origin.

The principal characteristic that sets metamaterials apart from natural media is the meta-atoms size, which is comparable to both the distance between them and the wavelength. This implies that low- and high-order may give comparable contribution to the scattered and/or radiated electromagnetic waves and they should be taken into account on the same basis. Consequently, it becomes impractical to simply consider a series featuring solely low-order dipole interaction among inclusions; higher order multipoles must also be accounted for [229]. Chiral particles, which have been extensively discussed in Ref. [230], since the chiral response originate from the interference of the electric dipole with magneto-dipole and electric quadrupole terms of the current density expansion. That is, at non-zero dipole moment, the electric quadrupole is essentially origin-dependent and conclusion on the chirality origin should be made with a care. Such a conclusion is also correct for the composite particles as elaborated in Ref. [229] (formula 17, p. 172). In this chapter, we demonstrate the critical nature of the origin's placement in ensuring the precise calculation of multipole moments, especially concerning secondary multipole decomposition [231].

Conventional definitions of dipole moments are typically applied to sources situated at the radiation center that coincides with the system's center of mass and geometric center of the sourse. However, if a source's geometric center differs from the coordinate center (e.g. due to experimental arrangement or fabrication inaccuracy or when the source consists of separated elements), this conventional approach may be inaccurate. This scenario is particularly relevant when examining clusters of metamolecules. To address this issue, we introduce electric, magnetic, and toroidal multipole moments when the origin shifted by vector $\boldsymbol{d}$ from the origin (Figure 2.1.1.). This can be achived

by replacing ***r*** in the multipole moments (1.3.1.2) with ***r - d***. The multipole moments denoted with "~" and defined with respect to the origin shifted by ***d*** are can be presented by the following equations:

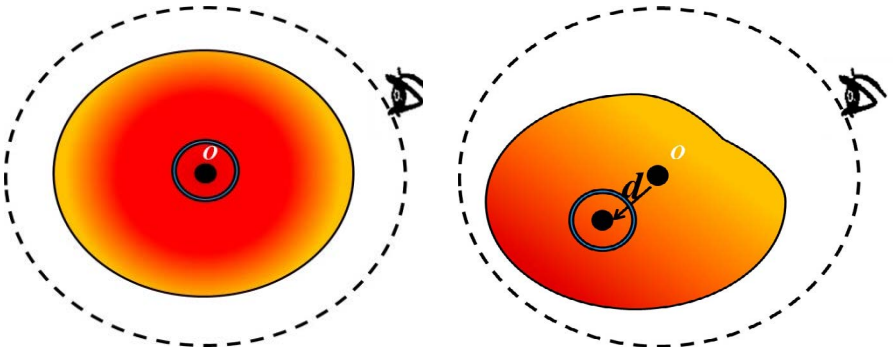

Figure 2.1.1. Schematical illustration of the shift of the radiation pattern. For external observer the radiated field is not changed, while multipoles contribution has altered

A shift in the configuration of multipoles results in the appearance of additional multipole components from a separate set in the multipole expansion, denoted as ~. Moreover, established equations for modified electric and magnetic quadrupoles are incorporated:

$$\tilde{p}_i = \frac{1}{i\omega}\int j_i d^3r = p_i$$

$$\tilde{m}_i = \frac{1}{2c}\int [(\boldsymbol{r}-\boldsymbol{d})\times j]_i d^3r = m_i - \frac{i\omega}{2c}(\boldsymbol{d}\times\boldsymbol{p})_i$$

$$\tilde{T}_i = \frac{1}{10c}\int [(\boldsymbol{r}-\boldsymbol{d})\cdot j](\boldsymbol{r}-\boldsymbol{d})_i - 2(\boldsymbol{r}-\boldsymbol{d})^2 j_i d^3r$$

$$= T_i - \frac{i\omega}{5c}p_i d^2 + \frac{i\omega}{10c}p_i d_i^2 + \frac{i\omega}{10c}d_i d_j p_j + \frac{i\omega}{10c}d_i d_k p_k$$

$$+\frac{3}{10}[m\times d]_i + \frac{\omega}{10ci}d_j Q^e_{ij} + \frac{\omega}{10ci}d_i Q^e_{ik} + \frac{3\omega}{20ci}d_k Q^e_{ii} \qquad (2.1.1)$$

$$\tilde{Q}^e_{ij} = \frac{i}{\omega}\int \left[(r_j - d_j)j_i + (r_i - d_i)j_j\right) - \frac{2}{3}\delta((\boldsymbol{r}-\boldsymbol{d})\cdot\boldsymbol{j})\Big] d^3r =$$

$$= Q_{ij}^{e} + d_j p_i + d_i p_j - \frac{2}{3}\delta(\boldsymbol{d}\cdot\boldsymbol{p})$$

$$Q_{ij}^{m} = \frac{1}{3}\int [(\boldsymbol{r}-\boldsymbol{d})\times\boldsymbol{j}]_i(\boldsymbol{r}-\boldsymbol{d})_j + (\boldsymbol{r}-\boldsymbol{d})_i[(\boldsymbol{r}-\boldsymbol{d})\times\boldsymbol{j}]_j d^3 r$$

$$= Q_{ij}^{m} + \frac{1}{3c} i\omega d_i d_k p_i - \frac{1}{3c} i\omega d_j d_k p_j + \frac{i\omega}{3c}\left(d_j^2 - d_i^2\right)p_k - d_j m_i - \frac{1}{3} d_i m_j$$
$$- \frac{\omega}{6ic} d_j Q_{jk}^{e} + \frac{\omega}{6ic} d_i Q_{ik}^{e} + \frac{\omega}{6ic} d_k\left(Q_{jj}^{e} - Q_{ii}^{e}\right)$$

2.1.1 Shifted electric dipole

The displacement of the origin by a vector $\boldsymbol{d}$ leads to the appearence of non-zero magnetic dipole and toroidal moments, which are determined by original undisturbed source's multipoles. Thus, if the electric dipole moment dominates the EM response of the source situated in the center of the particle, the EM response of the displaced source will be also has influenced by the electric, magnetic, and toroidal multipoles. Specifically, if only electric dipole and electric quadrupole moments of the source were non-zero in Equation (1.3.1.2), the multipoles momemnts at the displaced can be presented in the following form:

$$\tilde{p}_i = p_i$$

$$\tilde{m}_i = -\frac{i\omega}{2c}(\boldsymbol{d}\times\boldsymbol{p})_i$$

$$\tilde{T}_i = -\frac{i\omega}{5c} p_i d^2 + \frac{i\omega}{10c} p_i d_i^2 + \frac{i\omega}{10c} d_i d_j p_j + \frac{i\omega}{10c} d_i d_k p_k$$
$$+ \frac{\omega}{10ci} d_j Q_{ij}^{e} + \frac{\omega}{10ci} d_i Q_{ik}^{e} + \frac{3\omega}{20ci} d_k Q_{ii}^{e}$$

$$Q_{ij}^{e} = Q_{ij}^{e} + d_j p_i + d_i p_j - \tfrac{2}{3}\delta(\boldsymbol{d}\cdot\boldsymbol{p}) \qquad (2.1.2)$$

$$\tilde{Q}_{ij}^{m} = \frac{1}{3c} i\omega d_i d_k p_i - \frac{1}{3c} i\omega d_j d_k p_j + \frac{i\omega}{3c}\left(d_j^2 - d_i^2\right)p_k$$
$$- \frac{\omega}{6ic} d_j Q_{jk}^{e} + \frac{\omega}{6ic} d_i Q_{ik}^{e} + \frac{\omega}{6ic} d_k\left(Q_{jj}^{e} - Q_{ii}^{e}\right)$$

The induction of magnetic and toroidal moments in the multipole contribution of the shifted electric dipole causes the radiation pattern of the structure to undergo tilting and stretching through the introduction of *x* and *y* components of the magnetic and toroidal moments.

2.1.2 Shifted magnetic dipole

If the electric dipole, electric quadrupole and toroidal moments in (1.3.1.2) are zero, and remain zero at the shifted origin. Thus, when a magnetic dipole (a ring electrtric current) is displaced to a distance $\boldsymbol{d}$ from the coordinate center, the multipole response is determined by the magnetic dipole moment and toroidal dipole moment as the following:

$$\begin{aligned} \tilde{p}_i &= 0 \\ \tilde{m}_i &= m_i \\ \tilde{T}_i &= \tfrac{3}{10}[\boldsymbol{m} \times \boldsymbol{d}]_i \\ \tilde{Q}^e_{ij} &= 0 \\ \tilde{Q}^m_{ij} &= Q^m_{ij} - d_j m_i - \frac{1}{3} d_i m_j \end{aligned} \qquad (2.1.3)$$

When a ring with current is rotated along the center of radiation, giving rise to virtual poloidal currents, a toroidal moment is generated within the system. Consequently, due to the closed currents around the ring, the electric dipole moment vanishes even after shifting the ring. By utilizing the magnetic dipole (current ring) as an illustration, it is demonstrated that the magnetic dipole moment remains unchanged upon translation to the vector $\boldsymbol{d}$. The activation of *x* and *y*-components of the toroidal dipole moment is triggered by the presence of a *z*-component of the magnetic dipole moment, leading to an asymmetric radiation pattern.

2.1.3 Shifted toroidal dipole

When only electric dipole and electric quadrupole moments are zero, magnetic dipole moment remains unaltered, while the toroidal dipole is modified by

an additional component proportional to the magnetic dipole moment. Consequently, the radiation pattern of the shifted toroidal source may becomes asymmetric, if has a component orthogonal to . This phenomenon is explicitly depicted in Equation (2.1.4).

$$\begin{gathered}\tilde{p}_i = 0 \\ \tilde{m}_i = m_i \\ \tilde{T}_i = T_i + \frac{3}{10}[\boldsymbol{m} \times \boldsymbol{d}]_i \\ \tilde{Q}^e_{ij} = 0 \\ \tilde{Q}^m_{ij} = Q^m_{ij} - d_j m_i - \frac{1}{3} d_i m_j\end{gathered} \qquad (2.1.4)$$

When considering a toroidal dipole (a ring solenoid) that has been displaced from its initial location, the magnetic dipole moment remains the same, however the radiation pattern becoms asymmetric. It is worth noting that comparing the overall radiation patterns of the adjusted electric and toroidal sources may be confusing. Specifically, the rotation of one source relatively to the other might give rise to inquiries. This inconsistency can be traced back to the arrangement of the near zone of the source and its influence on radiation emission. In contrast to the electric dipole, in a toroid, the currents are concentrated within the volume. For example, when the ***T*** and ***m*** are aligned along the *z*-axis, the $\boldsymbol{T}_x$ component of the shifted toroidal moment is negative according to Equation (2.1.6), resulting in a shift in the pattern. This deviates from an electric source and signifies a crucial fundamental difference between the far-field radiation of toroidal and electric dipoles. These distinctions could potentially be clarified in forthcoming experiments.

In case of shifted electric dipole oriented along *z*-axis:

$$\begin{gathered}\tilde{\mathrm{T}}_{\mathrm{x}} = 0 \\ \tilde{\mathrm{T}}_{\mathrm{y}} = 0 \\ \tilde{\mathrm{T}}_{\mathrm{z}} = \frac{\mathrm{i}\omega}{10c}[(\mathrm{d_x d_z})\mathrm{p_z}].\end{gathered} \qquad (2.1.5)$$

In case of shifted toroidal dipole oriented along *z*-axis:

$$\begin{aligned} \widetilde{T}_x &= -\frac{3}{10} m_z d_y \\ \widetilde{T}_y &= \tfrac{3}{10} m_z d_x \\ \widetilde{T}_z &= T_z \end{aligned} \qquad (2.1.6)$$

Summing up the above statements, the shift of the center of the coordinate system actually does not lead to a change in the scattered electromagnetic field, however, it strongly affects the multipole series. That is, radiation pattern of particular multipoles may change drastically while the integral scattering characteristics are preserved. That is one may chose the position of the origin to strengthen or suppress a particular multipole thus simplifying interpretation of the observed phenomenon. For example, in non-radiating anapole configuration, it is possible to cancel the electric dipole moment of the system by a toroidal moment thereby leaving only the magnetic component radiating. For the problems of nonradiating structures in the frame of this thesis, this approach is of fundamental importance, since it enables more detailed observation of symmetric structures. Moreover, one can study symmetry breaking of the structure from viewpoint of altered set of multipoles and study its evolution for asymmetric strucures.

3 THE EXPERIMENTAL METHODS

3.1 Two horn antenna method for measurement of transmission spectrum in microwave range

For the measurement process, a chamber with an anechoic environment of sizes 2 × 2 × 3 m was employed. This chamber was outfitted with two wideband horn antennas (ETS-Lingren's model 3115), ECCOSORB absorbers, a rotary table, and a Vector Network Analyzer (Agilent E5071C ENA). Furthermore, a 20 dB amplifier was integrated to increase the signal-to-noise ratio. In this configuration, we can detect signal fluctuations up to -80 dB. In order to guarantee precise data collection, we carried out measurements of scattering cross-sections both with and without the sample to mitigate any potential inaccuracies and disturbances [232-234]. Origin of errors in the microwave measurements may vary, ranging from random internal thermal noise of electronic devices to long-stagedexternal reflections induced by objects within the vicinity, imperfect absorbers, cables, rotators, and other components (Refer to page 120 in [232]).

To avoid these, the signal scattered by the particle was normalized on the signal scattered when particle was absent [232]. This method entailed assessing the ambient radiation in the absence of a scattering object, followed by evaluating the object amidst the ambient radiation. By extracting preferredscattering signal from the combined particle-and-background signal, we managed to diminish the influence of measurement inaccuracies. This data processing alternative was made feasible by the VNA Agilent E5071C ENA.

The dimensions of the anechoic chamber permit a working area of about 20 cm^3 in the frequency range of interest. This is sufficient for examining a spheroidal particle with a diameter of 20 mm (refer to Section 4.1). By employing broadband horn antennas to generate a pseudo-spherical front, the spheroid particle can be harnessed to produce a plane wave front at distances greater than the wavelength. Hence, this setup is suitable for studying

scattering patterns [232-234]. The far field criterion for measurements is provided by formula 4.10 in Ref. [232]: R > 2d^2/λ, where R represents the distance between the antenna and the particle, d denotes the particle's size, and λ is the wavelength. The experimental setup (Figure 3.1) comprises a wide band horn antenna (1) that emits the incident wave, and antenna (2), which is situated 1.5 m above the the spheroidal particle and detects the scattered radiation. The antennas' polarization, as depicted schematically in Figure 3.1, was linked to the ports of a Vector Network Analyzer via a 50 Ohm cable. The radiation pattern was assessed by rotating antenna (2) around the particle.

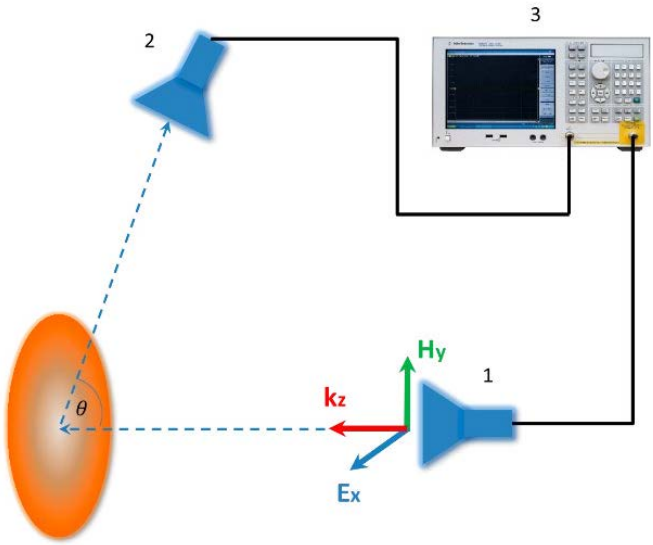

Figure 3.1. The experiment setup includess transmitting antenna (1), receiving antenna (2) and VNA Agilent E5071 C ENA (3). The incident wave is normal to the long axis of the spheroidal particle. The receiving antenna detens radiation scattered at angle with respect to long axis of spheroid

4 RESULTS AND APPLICATIONS

4.1 Transverse Kerker effect in all-dielectric metamaterials

Although, the generalized Kerker effect may exhibit resemblance to anapole states [19–21], there is fundamental differrence between them. While the generalized Kerker effect pertains to transverse scattering, the anapole particle does not scatter at all, even at higher multipoles, aligning with the optical theorem [22-26]. Conversely, the lateral scattering attribute of the generalized Kerker effect can be exploited in metasurfaces, especially in the realm of planar lasers and the interaction between near fields of particles. It can also facilitate the lateral excitation of nano-waveguides [2, 8, 18].

Our experiment focuses on the pronounced lateral scattering by a spheroidal all-dielectric particle. At the aspect ratio of a/b=2.1, the electric dipole and magnetic quadrupole resonances of the particles coincide. Consequently, the particle displays a transverse radiation pattern in the specified direction perpendicular to the incident wave front, resembling a dumbbell shape. These experimental findings correspond to the theoretical predictions. It is important to highlight that our study served as a “proof-of-concept” to demonstrate the transverse Kerker effect. This effect can also be witnessed with alternative shapes of meta-particles and permittivities.

The emission of dumbbell radiation arises from the interaction among multipole components. An initial step in understanding this phenomenon involves establishing the criteria for transverse scattering by using the multipole decomposition approach [31]. An interesting observation is the manifestation of the transverse Kerker effect, which leads to the suppression of both forward and backward scattering, consequently enhancing lateral scattering [18]. Our analysis predominantly focuses dipole and quadrupole on the contributions, which are usually sufficient to describe scattering of any particles. In terms of spherical harmonic expansion of the scattered filed, this implies we consider l=1 (electric and magnetic dipoles) and l=2 (electric and magnetic quadrupoles) terms:

$$\mathbf{E}_{(\mathrm{total})}(\theta,\varphi,\mathrm{r}) \approx \mathbf{E}_{(\mathrm{l}=1)}(\theta,\varphi,\mathrm{r}) + \mathbf{E}_{(\mathrm{l}=2)}(\theta,\varphi,\mathrm{r}) \tag{4.1.1}$$

$$\mathbf{E}_{(\mathrm{l}=1)}(\theta,\varphi,\mathrm{r}) \approx \frac{\mu_0 c^2}{3\sqrt{2\pi}} \frac{\exp(-\mathrm{ikr})}{\mathrm{r}} \sum_{\mathrm{m}=0,\pm1} \left[\left(\mathrm{k}^2 \mathrm{Q}_{1,\mathrm{m}} - \mathrm{ik}^3 \mathrm{T}_{1,\mathrm{m}}\right) \times \left(\mathbf{Y}_{1,2,\mathrm{m}} + \sqrt{2}\mathbf{Y}_{1,0,\mathrm{m}}\right) + \mathrm{i}\sqrt{3}\left(\mathrm{k}^2 \mathrm{M}_{1,\mathrm{m}} \times \mathbf{Y}_{1,1,\mathrm{m}}\right)\right] \tag{4.1.1}$$

$$\mathbf{E}_{(\mathrm{l}=2)}(\theta,\varphi,\mathrm{r}) \approx \frac{\mu_0 c^2}{10\sqrt{6\pi}} \frac{\exp(-\mathrm{ikr})}{\mathrm{r}} \sum_{\mathrm{m}=0,\pm1,\pm2} \left[\mathrm{ik}^3 \mathrm{Q}^{(\mathrm{e})}_{2,\mathrm{m}} \times \left(\sqrt{2}\mathbf{Y}_{2,3,\mathrm{m}} + \sqrt{3}\mathbf{Y}_{2,1,\mathrm{m}}\right) - \sqrt{5}\mathrm{k}^3 \mathrm{Q}^{(\mathrm{m})}_{2,\mathrm{m}} \times \mathbf{Y}_{2,2,\mathrm{m}}\right].$$

where μ_0 is the vacuum's magnetic permeability, *c is* the speed of light, ***r*** denotes the radius-vector, and $Y_{k,l,m}$signifies the spherical vector harmonics. The connection between spherical multipoles and Cartesian multipoles, such as electric dipole ***P***, magnetic dipole ***M***, toroidal dipole moment ***T***, electric quadrupole ***Qe***, and magnetic quadrupole ***Qm***, can be articulated as follows:

$$\mathrm{Q}_{1,0} = \mathrm{p}_z,\ \mathrm{Q}_{1,\pm1} = \frac{\mp \mathrm{p}_x + \mathrm{ip}_y}{\sqrt{2}},\ \mathrm{T}_{1,0} = \mathrm{T}_z,\ \mathrm{T}_{1,\pm1} = \frac{\mp \mathrm{T}_x + \mathrm{iT}_y}{\sqrt{2}},$$

$$\mathrm{M}_{1,0} = -\mathrm{M}_z,\ \mathrm{M}_{1,\pm1} = \frac{\pm \mathrm{M}_x - \mathrm{iM}_y}{\sqrt{2}},$$

$$\mathrm{Qe}_{2,0} = 3\mathrm{Qe}_{zz},\ \mathrm{Qe}_{2,\pm1} = \sqrt{6}\left(\mp \mathrm{Qe}_{xz} + \mathrm{iQe}_{yz}\right),$$

$$\mathrm{Qe}_{2,\pm2} = \frac{\sqrt{6}}{2}\left(\mathrm{Qe}_{xx} \mp \mathrm{i}2\mathrm{Qe}_{xy} - \mathrm{Qe}_{yy}\right), \tag{4.1.2}$$

$$\mathrm{Qm}_{2,0} = -\frac{3}{2}\mathrm{Qm}_{zz},\ \mathrm{Qm}_{2,\pm1} = \sqrt{\frac{3}{2}}\left(\pm \mathrm{Qm}_{xz} - \mathrm{iQm}_{yz}\right),$$

$$\mathrm{Qm}_{2,\pm2} = \frac{\sqrt{6}}{4}\left(-\mathrm{Qm}_{xx} \pm \mathrm{i}2\mathrm{Qm}_{xy} + \mathrm{Qm}_{yy}\right)$$

Cartesian multipoles can be calculated by means of integrating over the current density ***j****(r)* distribution within the volume of particle and $\alpha,\beta,\gamma = x,y,z$:

$$P_\alpha = \frac{1}{i\omega}\int j_\alpha d^3r,\ M_\alpha = \frac{1}{2c}\int [r \times j]_\alpha d^3r,$$

$$T_\alpha = \frac{1}{10c}\int [(r \cdot j)r_\alpha - 2r^2 j_\alpha]d^3r,\ P_\alpha = -p_\alpha + ikT_\alpha,$$

$$Qe_{\alpha\beta} = \frac{1}{i2\omega}\int \left[r_\beta j_\alpha + r_\alpha j_\beta - \frac{2}{3}(r \cdot j)\delta_{\alpha\beta}\right] d^3r, \qquad (4.1.3)$$

$$Qm_{\alpha\beta} = \frac{1}{3c}\int \left[r_\alpha [r \times j]_\beta + r_\beta [r \times j]_\alpha\right] d^3r.$$

here, $\delta_{\alpha\beta}$ is the Kronecker symbol.

The scattering cross section of the particle may be accurately described in terms of multipoles:

$$\sigma_{scat} = \frac{k^4}{6\pi\varepsilon_0^2|E_0|}(|M|^2 + |P|^2) + \frac{k^6}{80\pi\varepsilon_0^2|E_0|}\left(4\left|Qe_{\alpha\beta}\right|^2 + \left|Qm_{\alpha\beta}\right|^2\right) \qquad (4.1.4)$$

Let us contemplate two situations of transverse scattering that are mutually perpendicular to each other:

Condition 1. In the scenario of of and , the multipoles emit radiation solely in the transverse direction to the incident wave, resulting in scattering fields $\boldsymbol{E}_{(total)}(\theta=0)=0$ and $\boldsymbol{E}_{(total)}(\theta=\pi)=0$.

Condition 2. In the situation of $\theta=\pi/2$ and $\theta=3\pi/2$, the multipoles emit radiation exclusively along the incident wave direction, leading to scattering fields $\boldsymbol{E}_{(total)}(\theta=\pi/2)=0$ and $\boldsymbol{E}_{(total)}(\theta=3\pi/2)=0$.

By consulting Equation (4.1.1) and adhering to the prescribed methodologies, one can readily deduce the solution for conditions 1 and 2. This aids in establishing connections between the electric dipole ***P*** and the magnetic quadrupole *Qm*. Nevertheless, it is crucial to acknowledge that the remaining multipoles in our system do not exhibit a substantial response.

$$P_\alpha = -\frac{ik}{2} Q_{m_{\beta\gamma}}, \quad P_\alpha = \frac{ik}{2} Q_{m_{\beta\gamma}} \tag{4.1.5}$$

Similar conditions can be derived for magnetic dipole and electric quadrupole. This straightforward outcome highlights that achieving zero radiation (Transverse Kerker effect) concurrently in backward and forward directions (Condition 1), or simultaneously in lateral directions (Longitudinal Kerker effect) (Condition 2) is feasible solely through the interference between two multipoles of electric dipole moment and magnetic quadrupole. The direction of radiation is predominantly influenced by the phase of the magnetic quadrupole, as indicated by its polarity. Corresponding results were computationally obtained by Asano & Yamamoto [32], without an explanation for side scattering.

To investigate this distinctive characteristic, we will scrutinize the electromagnetic scattering by a high-index dielectric spheroidal particle with major semiaxis *a* and minor semiaxis *b*. The aspect ratio, *a/b*, denotes the spheroid's shape, varying from a needle-like form (prolate spheroid) when *a/b* > 1, to a sphere when *a/b* = 1, and to a disk-like configuration (oblate spheroid) when *a/b* < 1. In our experimental inquiry, our emphasis will be on a prolate spheroid with *a* = 19.5/2 mm and *b* = 12.5/2 mm, resulting in an aspect ratio of *a/b* = 1.56.The dielectric permittivity of the particle is ε = 150, suggesting a ceramics material with a high refractive index. The particle will encounter a plane wave with lateral incidence, where the polarization vector E will align parallel to the minor axis of the spheroid. The configuration of the particle and the incident wave are illustrated in Figure 4.1.1.

In this study, we have illustrated the potential of spheroidal all-dielectric particles in exhibiting the transverse Kerker effect, offering enhanced tunability compared to spheres due to their additional radius. To achieve this objective, we focus on a spheroid defined by a specific mathematical equation:

$$\frac{x^2}{b^2} + \frac{y^2}{a^2} + \frac{z^2}{b^2} = 1 \tag{4.1.6}$$

To illustrate the transverse scattering phenomenon, we conducted simulations of electromagnetic scattering by spheroidal particles with varying aspect ratios *a/b* (see Figure 4.1.2). To accomplish this, we utilized the commercial version of CST Microwave Studio and the Time domain solver with open boundary conditions. The particles were exposed to a plane wave with linear polarization (Figure 4.1.1 (a)). The scattering cross section σ was normalized to $\sigma/\pi ab$. For small aspect ratios *a/b* < 1, the particle exhibits a disc-like shape, with the scattering behavior primarily dictated by two main resonances: the magnetic dipole moment **M** and the electric dipole **P**. This pattern persists until *a/b* = 1, marking the transition from disc to sphere. At *a/b* > 1, the bifurcation point observed at *a/b* = 1 and *q* = 1.1 splits into two resonances. Both resonances involve an electric dipole moment and a magnetic quadrupole moment, with the key distinction being the phases of the magnetic quadrupoles. In the case of transverse scattering, the electric dipole moment *Px* and the magnetic quadrupole components *Qmyz* exhibit positive phases, while in the second resonance (longitudinal scattering), the phases are reversed (Figure 4.1.2).

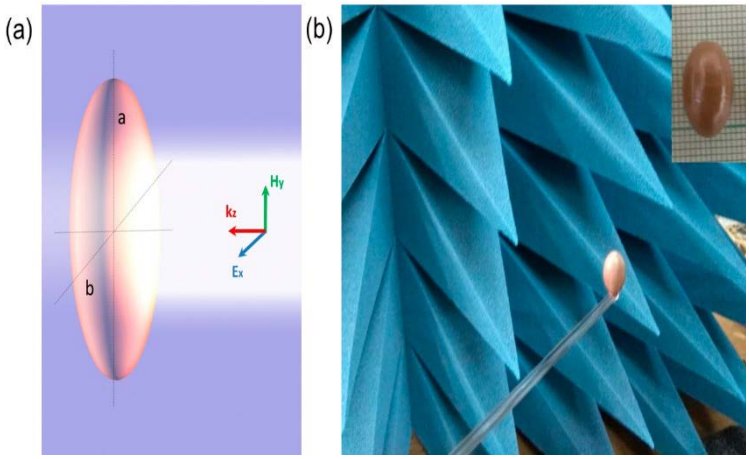

Figure 4.1.1. (a) Depiction of a high-index all-dielectric spheroidal particle with dielectric permittivity ε =150 and major and minor semi-axes *a* and *b*, respectively. A linearly polarized plane wave is incident laterally, with vector ***E*** aligned parallel to the minor axis. (b) Experimental setup featuring a ceramic spheroidal particle with *a* = 19.5/2 mm and *b* = 12.5/2 mm within an anechoic chamber. The inset provides a visual of the sample

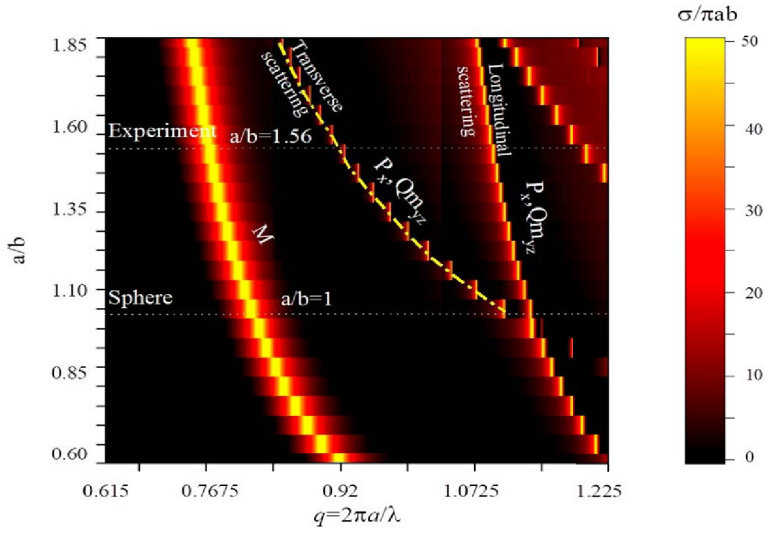

Figure 4.1.2 Illustration of dependence of the normalized scattering cross-section of spheroidal all-dielectric particles on the aspect ratio a/b and size parameter *q*. Experimental data for *a/b* = 1.56 reveals three peaks, two of which correspond to transverse and longitudinal scatterings

To characterize the electromagnetic response of a prolate spheroid (*a/b* > 1) and its modes, we analyzed the spectra derived from CST Microwave Studio for a particle with *a/b*=1.56. Additionally, we present experimental findings on the scattering cross-section (as depicted in Figure 4.1.3). The resonance peaks identified at 1.8 GHz, 2.17 GHz, and 2.65 GHz exhibit a satisfactory agreement between theoretical predictions and experimental results.

In order to enhance comprehension regarding the origins of these peaks, a multipole decomposition was conducted on the four main multipoles stimulated in the system encompassing electric dipoles (***P***), magnetic dipoles (***M***), electric quadrupoles (*Qe*), and magnetic quadrupoles (*Qm*) for the initial and secondary resonances. The primary peak close to 1.8 GHz is predominantly governed by the magnetic response (***M***) (as illustrated in Figure 4.1.4). The impacts of the other multipoles are adequately restrained and do not markedly influence the system's reaction. A reassessment of the scattering resonance profile was performed based on the multipoles,

demonstrating good conformity with the scattering cross-section computed by CST.

Figure 4.1.5 demonstrates the scattering pattern of the structure in the near-field. The second resonance detected at 2.17 GHz emerges from the interplay between the electric dipole components ($\boldsymbol{P}_x$) and the magnetic quadrupole ($Q_{myz} = Q_{mzy}$) (Figure 4.1.6). Analogous to the first resonance, the remaining multipoles converge towards zero and make insignificant contributions to the system's response.

Likewise, the third peak at 2.65 GHz is also distinguished by the electric dipole ($\boldsymbol{P}_x$) and the magnetic quadrupole (Q_{myz}) components (Figure 4.1.7). Notably, the scattering responses at 2.17 GHz and 2.65 GHz display analogous contributions from the multipoles. Nonetheless, an examination of the phases of these multipoles in close proximity to the resonances is carried out to detect any distinctions. Specifically, the phases of the electric dipole and the magnetic quadrupole at 2.175 GHz are both positive and equal to 1.752 rad and 0.1338 rad, respectively (Figure 4.1.6 (b)). However, the phase of the magnetic quadrupole at 2.648 GHz is negative, namely -1.9 rad (Figure 4.1.7 (b)). To elucidate the resulting radiation patterns at the resonant frequencies of 2.175 GHz and 2.648 GHz, the radiation patterns of the electric dipole and the magnetic quadrupole are plotted, considering their amplitudes and phases. For the resonance at 2.175 GHz (Figure 4.1.6 (c)), the electric dipole and the magnetic quadrupole emit with positive phases, leading to increased radiation in the ***y*** direction and reduced radiation along the ***z***-axis. Conversely, the radiation at 2.648 GHz (Figure 4.1.6 (c)) is shaped by destructive interference between the electric dipole and the magnetic quadrupole in the ***y***-direction, while the radiation in the ***z***-direction is consistent in both forward and backward directions.

Hence, the scattering pattern of an all-dielectric spheroidal particle is mainly defined by the electric dipole and the magnetic quadrupole, along with their corresponding phase signs. Our computational findings align well with Equation (4.1.3).

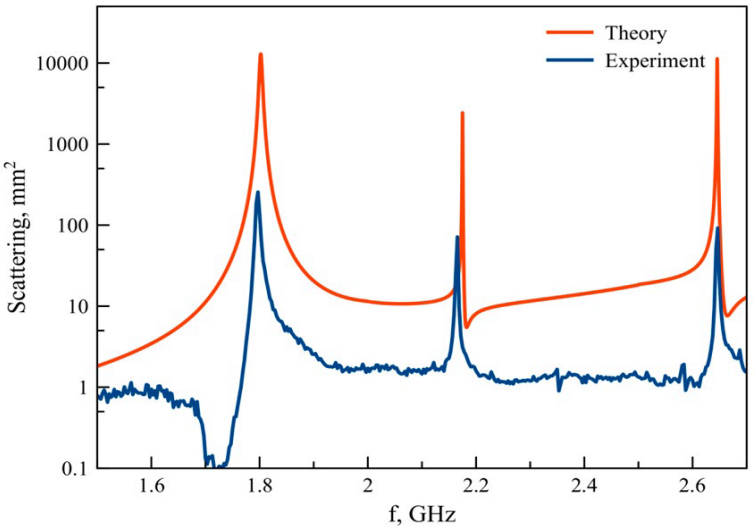

Figure 4.1.3. Simulation and measurement of scattering characteristics of spheroid with aspect ratio *a/b* = 1.56 in the range range 1.5–2.5 GHz

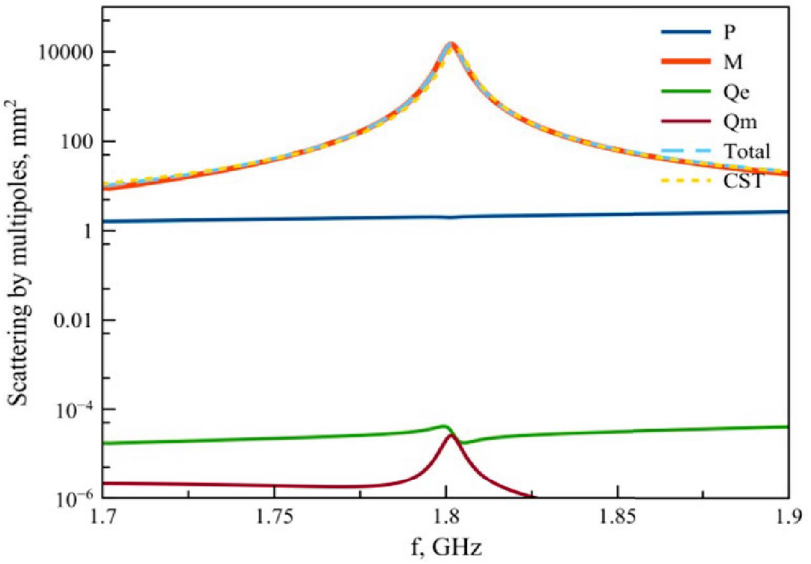

Figure 4.1.4. Scattering cross section of scattered multipoles on 1.8 GHz

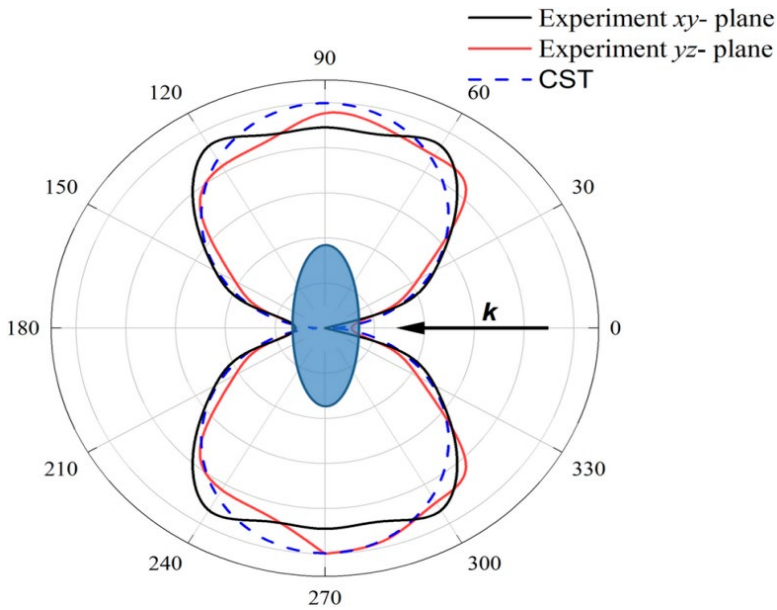

Figure 4.1.5. Theoretical and experimental radiation pattern on 2.17 GHz for *xy*-plane, *yz*-plane

In order to examine transverse scattering in a proof-of-concept microwave experiment, we employed a high-voltage capacitor crafted from titanate-based ceramics ($SrTiO_3$), specifically the ceramic K15U-2. Initially, a ceramic spheroidal particle was generated by mechanically grinding a ceramic cylinder. The particle's dimensions were precisely determined using a caliper with an accuracy of ±0.1 mm, showcasing a large axis of $2a$ = 19.5 ± 0.1 mm and a small axis of $2b$ = 12.5 ± 0.1 mm. These ceramics exhibit a notably high dielectric permittivity (up to 180) within the microwave range along with a corresponding loss tangent ranging from $tan\ \delta = 10^{-4}$ to 10^{-3} [34, 35]. Within our specific frequency range, the sample displayed a loss tangent of $tan\ \delta = 3\ 10^{-4}$ and a permittivity of ε = 150 at a frequency of 1.6–2.6 GHz. The examination of transverse scattering was conducted, and its radiation pattern was assessed at 2.17 GHz in the *xy* and *yz*-planes.

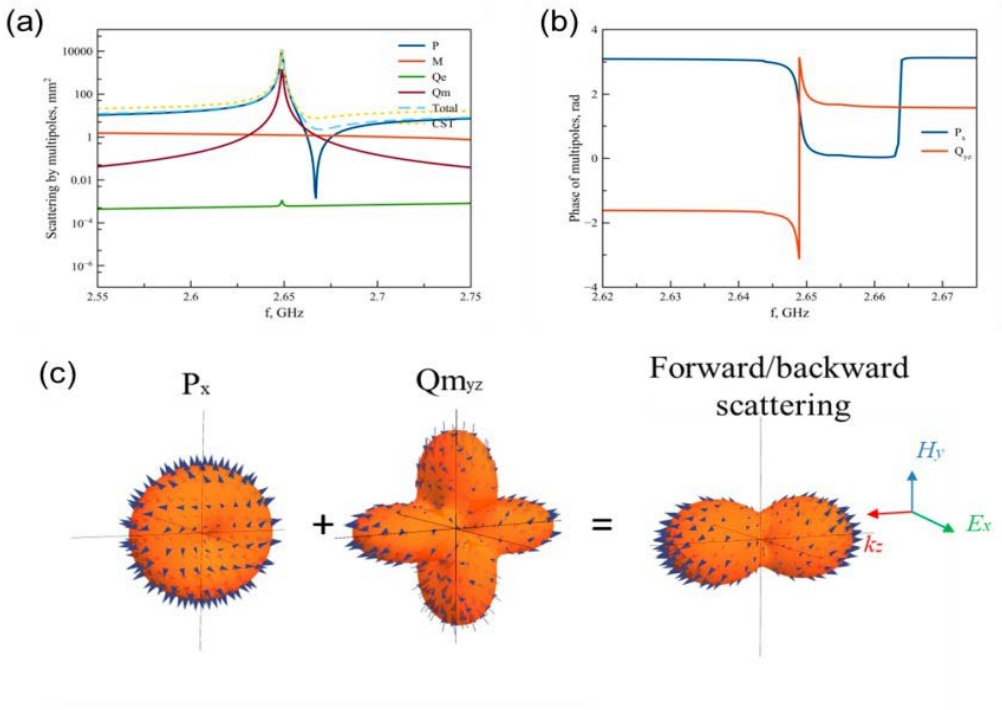

Figure 4.1.6. (a) Scattering cross section (SCS) of scattered multipoles at 2.175 GHz. (b) Illustration of phases of electric dipole and magnetic quadrupole. (c) Illustration of radiation pattern of excited electric dipole and magnetic quadrupole and total radiation pattern

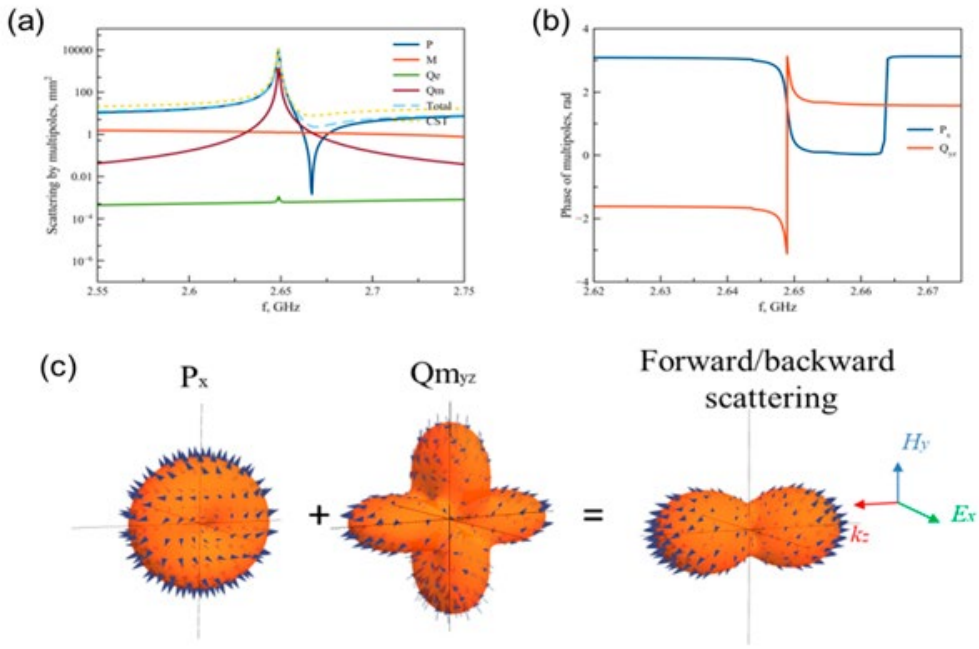

Figure 4.1.7. (a) Scattering cross section (SCS) of scattered multipoles at 2.64 GHz. (b) Illustration of phases of electric dipole and magnetic quadrupole. (c) Illustration of radiation pattern of excited electric dipole and magnetic quadrupole and total radiation pattern

Our experimental findings reveal diminished scattering at 0 and 180-degree angles, while accentuated scattering was observed at 90 and 270-degree angles, aligning with simulated outcomes acquired through CST Microwave Studio. The measured deviations fall within an acceptable range for the anechoic chamber (±2.5 dB). Discrepancies between the experimental and simulated data may be ascribed to losses in the ceramic material and fabrication procedures, resulting in narrower resonant peaks and a broader radiation pattern (Figure 4.1.3). Furthermore, the process of shaping spheroids from cylinders and manufacturing inaccuracies might lead to flatter tops on the spheroids, consequently yielding a broader radiation pattern.

In this context, we explore the evolution of the transverse scattering peak with respect to permittivity and simulate the scattering cross-section

of spheroidal particles possessing a size ratio of *a/b* = 1.56. For silicon's low permittivity (ε = 16), the scattering cross-section is both limited and wide-ranging, reaching a maximum value of 7. To achieve the transverse Kerker effect in visible optics (red light at 700 nm), the particle dimensions should be *a* = 423 nm and *b* = 271 nm. However, with an increase in spheroid permittivity, the scattering intensity escalates and the peak related to the transverse Kerker effect narrows. Material properties and dimensions can be selected based on our graphical representations. Hence, for permittivity values of 25, polaritonic crystals (NaCl, KCl, LiF) in the THz range are suitable, while for values of 100 or higher, BSTO ceramics in the microwave domain are preferable.

For the purpose of calculating the Q-factors of asymmetric Fano resonance, the Fano resonance approach [47] was utilized. Within this methodology, the Q-factor derived from the scattering spectra is defined as Q = (fd + fp) / (fd - fp), where the resonant region is situated between the dip fd and peak fp frequencies.

4.2 Broadband transparency in self-complementary metamaterials based on Babinet principle

Commonly, light-matter interaction of metamaterials and particles is characterized by the contribution of multipoles to the intensity of transmission and reflection spectra. Correspondingly, the intensity of far-field radiation of the source can be represented as a series of these multipoles:

$$\mathbf{E}_S = \frac{\mu_0 c^2}{2\Delta^2}\left[i\mathbf{k}(P_\parallel + ik\hat{\mathbf{R}} \times \left(M_\parallel + i\mathbf{k}R_\parallel^m\right)) + k^2\left(\left(Q^e + i\mathbf{k}Q^T\right)\cdot\hat{\mathbf{R}}\right)_\parallel - \frac{k^2}{2}\hat{R} \times \left((Q^m + i\mathbf{k}\mathbf{R}Q^m)\cdot\hat{\mathbf{R}}\right)_\parallel\right] e^{-ik\hat{\mathbf{R}}}, \quad (4.2.1)$$

where the subscript $(\ldots)_{||}$ denotes the projection of the corresponding vector onto the plane of the array and is the distance from the array to the observer.

One can consider that the total transparency of metamaterial is associated with the nullifying of multipole intensities up to higher multipoles. This situation can be satisfied if the metamaterial consists of several independent parts or layers 1, 2 … N, where *N* is number of parts or layers. And each multipole in decomposition Equation (4.2.1) presents a compound state. It means the intensity of *l*- multipole moment is:

$$I_l = |R_1^l + R_2^l|^2. \tag{4.2.2}$$

From Equation (4.2.2) follows that the intensity of each *l*-multipole moment can be almost zero if multipole compensates and one can observe total transparency if other multipoles are negligible in system.

Thus, our approach for demonstration of total transparency is representing multipoles opposite to each other. For this aim, we present modified multipoles decomposition for shifted sources/scatterers on distance d from coordinate center:

$$\begin{aligned}
\tilde{p}_i &= \frac{1}{i\omega}\int j_i d^3r = p_i \\
\tilde{m}_i &= \frac{1}{2c}\int [(\mathbf{r}-\mathbf{d})\times\mathbf{j}]_i d^3r = m_i - \frac{i\omega}{2c}(\mathbf{d}\times\mathbf{p})_i \\
\tilde{Q}_{ij}^e &= \frac{i}{\omega}\int \left[(r_j - d_j)j_i + (r_i - d_i)j_j\right) - \frac{2}{3}\delta\big((\mathbf{r}-\mathbf{d})\cdot j\big)\Big] d^3r \\
&= Q_{ij}^e + d_j p_i + d_i p_j - \frac{2}{3}\delta(\mathbf{d}\cdot\mathbf{p})
\end{aligned} \tag{4.2.3}$$

$$\begin{aligned}
\tilde{Q}_{ij}^m &= \frac{1}{3}\int [(\mathbf{r}-\mathbf{d})\times j]_i(\mathbf{r}-\mathbf{d})_j + (\mathbf{r}-\mathbf{d})_i[(\mathbf{r}-\mathbf{d})\times\mathbf{j}]_j d^3r = \\
&= Q_{ij}^m + \frac{1}{3c}i\omega d_i d_k p_i - \frac{1}{3c}i\omega d_j d_k p_j + \frac{i\omega}{3c}\left(d_j^2 - d_i^2\right)p_k - d_j m_i - \frac{1}{3}d_i m_j - \frac{\omega}{6ic}d_j Q_{jk}^e \\
&+ \frac{\omega}{6ic}d_i Q_{ik}^e + \frac{\omega}{6ic}d_k\left(Q_{jj}^e - Q_{ii}^e\right)
\end{aligned}$$

One should note that the shift of the electric dipole ED does not necessarily lead to change of its moment, since the dipole moment does not depend on the coordinates. Meanwhile, other multipole moments depend on the

contribution of an electric dipole ED and their shift in the form of separate terms.

Let us imagine two electric dipoles with opposed dipole moments +*p* and -*p* shifted from coordinate center as +*d* and -*d*, respectively. In this case, the overall multipoles are almost zero, as followed from Equation (4.2.3). Obviously, the electric moments disappear as a result of ordinary interference, while the magnetic moments of the shifted dipoles vanish as a result of the compensation of terms depending on the electric dipole moments and shift vector *d*.

To prove our idea, we theoretically and experimentally have investigated the Babinet principle based metamaterial based on the sheets with a checkerboard-like pattern. Let us use the same terminology as we introduced in the Section 1.4 and the metallic unit cell of first or original screen "oS" should spatially correspond to the void unit-cell of the complementary screen "cS" (Figure 4.2.1.) Notably, such structure is both self-complementary and self-dual, thus, it is awaited to demonstrate non-trivial transparency effect due to modified multipoles interaction excited in each unit-cell.

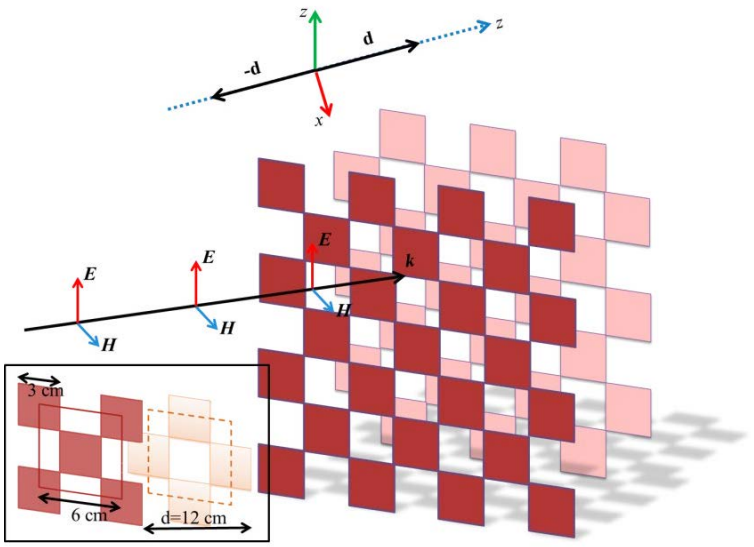

Figure 4.2.1. The illustration of Babinet metamaterial and orientation of plane wave. The colored squares are supposed to be metallic while void squares are supposed to be a vacuum. The metal squares of first layer

spatially corresponds with vacuum squares of second layer along ***x*** axis

The Babinet principle is an approach of the theory of diffraction for the convenient calculation of electromagnetic wave interaction with complementary objects. Thus, Babinet principle is consistent with electromagnetic duality due to complementary screens enabling structural inversion to interchange their metallic and void parts. Quite exciting is metamaterial with checkerboard-like pattern, if one change metal cells and vacuum voids, then the spectral characteristics of such a metamaterial will not change, and the multipole contributions of the unit-cells will remain the same.

It is worth noting another feature of Babinet metamaterials, presented in the form of separate sheets of a checkerboard. In this case, each such surface will have a transmission coefficient of $T = 0.5$ over a wide frequency range. Accordingly, it is expected that layers of checkerboard metamaterials spaced more than a wavelength from each other would have the same transmittance as a single layer. However, the situation changes drastically if the layers are placed in the near field zone of each other. In this case, dipole moments can be the same intensities but contrary directed to each other. Thus, the multipole moments of the layers will be compensated and the radiation intensity of all multipoles will be zero in broad frequency band. Indeed, near-field coupling between layers will lead to a narrowing of the frequency range. Nevertheless, we expect it to be quite broad in the experiment.

In order to achieve this objective, simulations were conducted using the CST Microwave Studio simulator employing the Time domain modeling approach along with appropriately implemented periodic boundary conditions (depicted by the black curves in Figure 4.2.2). The model is composed of a Babinet metamaterial consisting of two layers of metallic complementary checkerboard-like structures. The unit cell length is denoted as $P = 3$ cm, the metal layer thickness as $s = 5$ mm, and the spacing between screens as $d = 1.2$ cm. These metamaterial layers are assumed to be constructed from copper sheets and encompass an array of metallic unit cells. The simulated transmission spectra indicated ultra-broadband absolute transmission ranging from 4GHz to 6.5 GHz at 0 dB, which holds significant practical importance (Figure 4.2.2 b). Additionally, transmission simulations were conducted for distances greater ($d = 30$ mm) and lesser ($d = 6$ mm) than the

established distance between the layers (Figure 4.2.2 (a) and (c) represented by black curves).

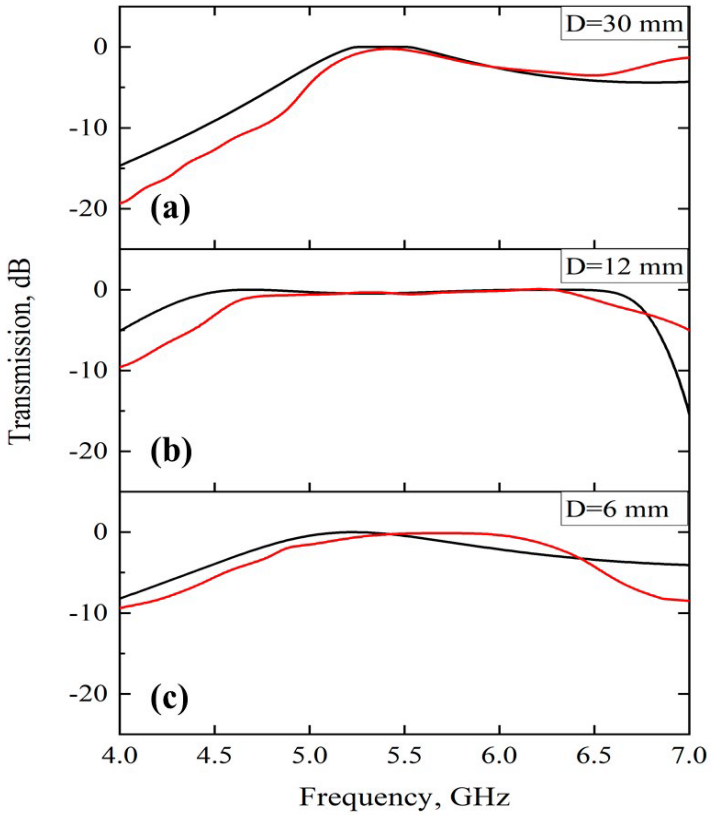

Figure 4.2.2. The simulated (black curve) and measured (red curve) transmission spectra of Babinet metamaterial for different distance *D* between them

Moreover, the objective was to elucidate the nature of the transparency effect through an analysis of multipole contributions. To achieve this, the Cartesian multipole moments were directly computed by integrating the induced displacement current density ***j*** over the entire volume of the unit cell. The time dependence was considered to be monochromatic in nature. The current density ***j*** at specific frequencies was numerically determined utilizing CST Microwave Studio.

The multipole moments are typically characterized in terms of electric and magnetic dipoles and quadrupoles, as they are the most prominent among all multipoles within the system. For a clearer understanding, the irradiation intensity was examined separately for the first screen “oS” in the two-screen system, the second screen “cS” in the two-screen system, and the combined irradiation from both screens in the two-screen system “oS+cS” (refer to Figure 4.2.3). The shift *d* of each layer relative to the coordinate center was considered for accurate calculations, as illustrated in Equation (4.2.3).

The distinct broad peak observed at 4-6 GHz cannot be straightforwardly elucidated by the common multipoles contributions of the entire metamaterial. The resolution lies in the utilization of modified multipoles and the application of the secondary multipole analysis method [25]. Each multipole moment of the metamaterials can be expressed as a sum of the same order multipole moments of its layer computed with respect to the same center of mass.

This aim entails the consideration of individual current densities in each layer while taking into account the irradiation across the entire system. When examining the multipoles of the initial layer at resonance frequency, it is apparent that magnetic quadrupole primarily influences transmission, with resonant suppression of dipole irradiation (Figure 4.2.3 (a)). Similarly, for the multipoles of the second layer, radiation from both quadrupoles and electric dipoles is resonantly suppressed (Figure 4.2.3 (b)). Consequently, in the combined system of both layers, an overall suppression of up to 100 times in radiation from multipoles is observed, along with variations in multipole interaction (Figure 4.2.3 (c)). The resonant behavior of transmission is substantiated by the resonant suppression of electric dipoles, while other multipoles are gradually suppressed. Based on these findings, it can be inferred that the resulting transparency effect arises from the interaction between multipoles from both layers, leading to a decrease in overall intensity. The conflicting interaction between the multipoles of the entire metamaterial is due to oppositely directed currents in each layer generating multipoles that mutually cancel out.

(a)

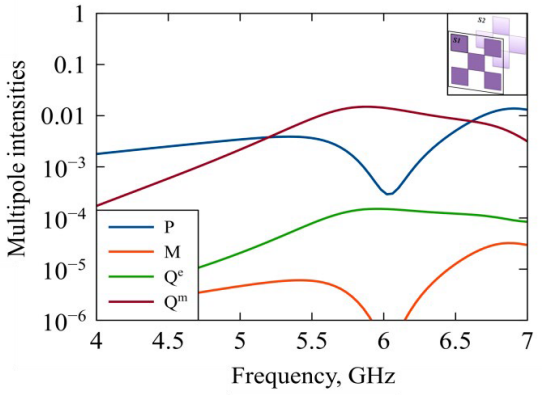

(b)

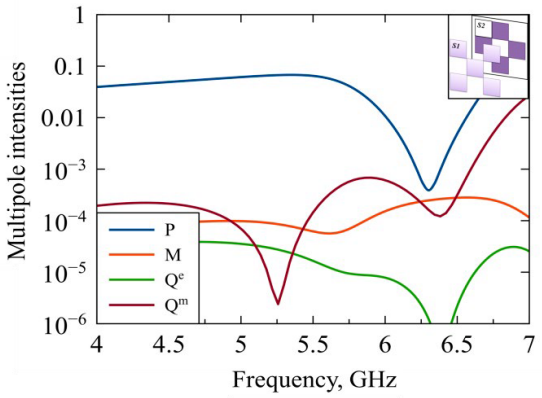

(c)

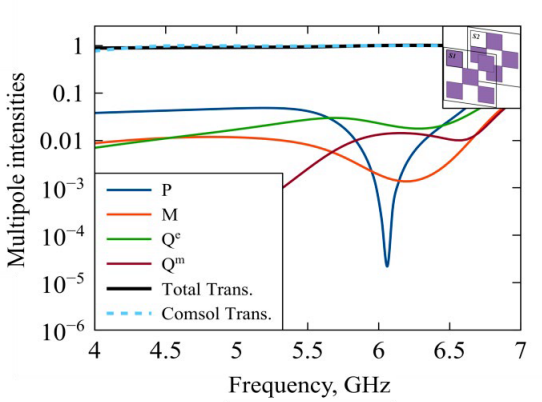

Figure 4.2.3. (a) Calculated multipoles in case of first layer illuminated by plane waves in the presence of second layer. (b) Calculated multipoles in case of second layer illuminated by plane waves in whole system in the sum with the first layer. (c) Calculated multipoles for metamaterials illuminated by plane waves in whole system

This section focuses on verifying our concept and investigating the manifestation of the transparency effect through a microwave experiment involving Babinet metamaterials. The initial step involves the fabrication of an experimental sample, where the planarity of metamaterial surfaces and the simplicity of the unit cell pattern are highlighted as key advantages of the overall structure, facilitating easy scaling to higher frequencies. The sample, made of copper sheets and cut using laser cutting technique, aligns with the parameters of the simulation model (Figure 4.2.4). S21 parameters (transmission) are measured in an anechoic chamber using the two-horn method, with broadband horn antennas P6-23M positioned 1 meter away from the metamaterial samples for electromagnetic radiation and detection. The transmission coefficient S21 of the electromagnetic waves passing through the metamaterial sample is recorded using a Vector Network Analyzer Rohde & Schwarz SVB20 within the 2–8 GHz frequency range. The experiment takes place in an anechoic chamber fitted with ECCOSORB absorbers, two wideband horn antennas P6-23M, a rotary table, and a Vector Network Analyzer Rohde & Schwartz. The measured transmission characteristics are compared with simulated data in Figure 4.2.1, showing precise match between experimental and simulation results.

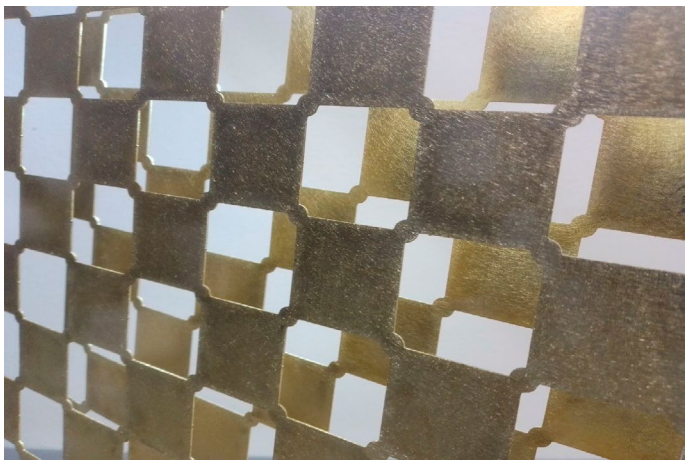

Figure 4.2.4. The illustration of fabricated Babinet metamaterial. Layers are made of copper

To study in details the interaction between complementary surfaces, we investigated the dependence of transmission on the distance between complementary surfaces. In Figure 4.2.5 we show the transmission coefficients at various distances between the surfaces. Firstly, we have studied the case of d=0, i.e. surfaces stand alone and behave as an entire metallic plate resulting in zero transmission. As the distance increases, one can see the appearance of modes $\mathbf{p}_1$ and $\mathbf{p}_2$ approaching each other as the distance between surfaces increases. At chosen distance d = 12 cm there is an absolute transmission. Therefore, further increase in the distance leads to divergence of modes $\mathbf{p}_1$ and $\mathbf{p}_2$ in opposite directions, thereby violating the regime of absolute transmission, i.e. there is no more interaction between complementary surfaces.

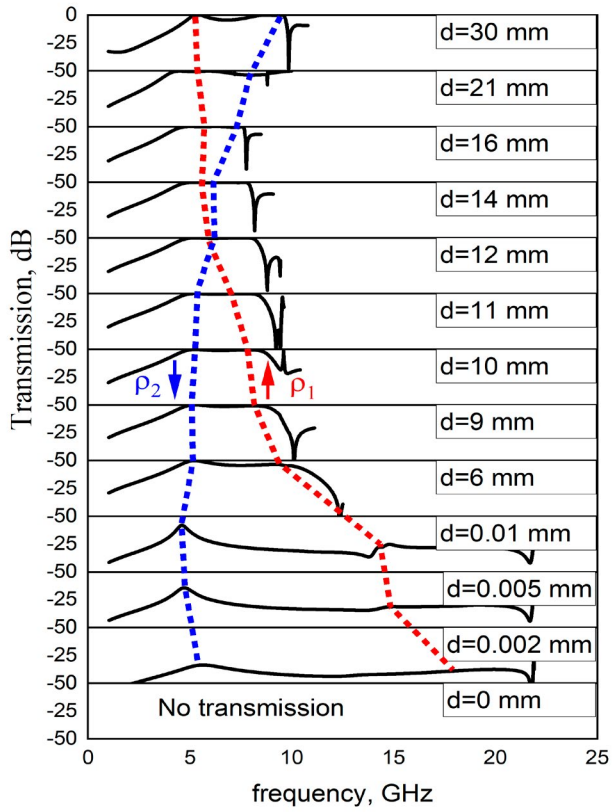

Figure 4.2.5. The dependence of transmission properties on the distance *d* between complementary surfaces

This section dedicated to the discussion of ultra-broadband absolute transmission within the 4-6.5 GHz range in Babinet principle-based metamaterials. The investigation serves a dual purpose. Firstly, it showcases the reliability of the modified multipole decomposition as a valuable tool for electrodynamic analysis of structures with shifted multipole centers. Secondly, it demonstrates ultra-broadband absolute transmission at 0 dB, highlighting the advantage of broad resonance in photonics, particularly for highly sensitive sensors, broadband filters, and similar applications. Broadband transmission and various multipole effects are linked to destructive interference among multipoles, leading to the suppression of far-field irradiation while enhancing near-field interactions between layers. Therefore, positioning any scatterer within the space between the layers will result in either enhanced transmission or conversely, suppression, depending on whether the object is located in an antinode or within the maximum field. The misalignment of the multipoles will consequently generate ultra-narrowband spectral characteristics in the transmission spectrum of the metamaterial. This phenomenon is facilitated by a simplistic design that could potentially be replicated in the more esteemed THz and optical frequency range in future.

CONCLUSION

In this thesis, we thoroughly discussed the phenomenon of multipole decomposition in composite structures as well as in structures with a displaced center. It was shown that additional terms of the multipole expansion, arising due to the shifted center of the structure, make a significant contribution to the study of near-field interaction.

In Chapter 1 we briefly discussed the current state of the problem, discussed the basic properties of metamaterials, have given definition of multipoles and multipole expansion, introduced the concept of the Babinet principle and Babinet principle based metamaterials.

In Chaper 2 we thoroughly discussed the generalized multipole expansion approximation. We have developed a multipole expansion method for structures of a displaced or complex center. We have demonstrated the excitation of previously neglected components of the magnetic and toroidal dipoles.

In Chapter 3 experimental method of measurement of transmission properties was briefly discussed.

In Chapter 4 we have considered the main results. In section 4.1 we demonstrated transverse Kerker effect on the base of spheroid particle. We have demonstrated secondary multipole expansion method using the spheroid particle as an example and provided theoretical and experimental results on near field properties investigations. In section 4.2 we presented self-complementary planar metamaterial possessing ultrabroadband transmission due to Babinet principle. Using such a composite structure as an example, we demonstrated the accuracy of the method of secondary multipole expansion, which on the base of excited multipoles, determined the origin of the transmission effect.

Scientific novelty. In this work, for the first time was demonstrated the method of multipole decomposition, that takes into account the redistribution of multipoles in a structure with a shifted center of coordinates as well as in the structure comprising several sub-structures. A model of a dielectric spheroidal particle supporting the transverse Kerker effect has been developed. For the

first time, broadband full transmission in the GHz range based on a planar metal metamaterial has been theoretically and experimentally demonstrated.

Theoretical and practical **significance** of the work. The method that describes the distribution of multipoles in structures with a shifted geometric center and containing several subsystems has been developed. The scientific significance of the approach is the correct consideration of multipoles in such systems, therefore allowing obtaining the correct results of theoretical and analytical investigation which, in turn, will perfectly match the experimental results.

In addition, a model of a subwavelength dielectric particle capable of suppressing scattering in the front and backward directions has been developed. In this way, all scattered fields will be redirected laterally, thereby allowing such a structure to be used as an invasive sensor.

A model of a planar metallic metamaterial consisting of two complementary surfaces of square unit cells, whose design is based on the Babinet principle, is presented. This metamaterial is of particular interest, firstly, due to the possibility of obtaining broadband full transmission in GHz range. In modern literature, the problem of broadband transmission has been barely studied, although it is crucial for increase of the volume of data transmission.

BIBLIOGRAPHY

1 G. Mie, “Beitrage zur Optik truber Medien, speziell kolloidaler Metallosungen,” Ann. Phys. (Leipzig) 25, 377 (1908).

2 C. F. Bohren and D. R. Huffman, Absorption and Scattering of Light by Small Particles (Wiley-Interscience, 1983).

3 J. D. Jackson, Classical Electrodynamics (Wiley, 1962).

4 V. A. Fedotov, A. V. Rogacheva, V. Savinov, D. P. Tsai, N. I. Zheludev, “Resonant Transparency and Non-Trivial Non-Radiating Excitations in Toroidal Metamaterials,” Scientific Reports 3, 296 (2013).

5 I. Fernandez-Corbaton, S. Nanz and C. Rockstuhl, “On the dynamic toroidal multipoles from localized electric current distributions,” Sci. Rep. 7, 1–8 (2017).

6 V. A. Fedotov, M. Rose, S. L. Prosvirnin, N. Papasimakis & N. I. Zheludev, “Sharp trapped-mode resonances in planar metamaterials with a broken structural symmetry,” Phys. Rev. Lett. 99, 147401 (2007).

7 U. Fano, “Effects of Configuration Interaction on Intensities and Phase Shifts,” Phys. Rev. 124, 1866–1878 (1961).

8 Wei Liu and Yuri Kivshar, “Generalized Kerker effects in nanophotonics and meta-optics,” Optics Express 26(10), 13085-13105 (2018).

9 A. E. Miroshnichenko, S. Flach and Y. S. Kivshar, “Fano resonances in nanoscale structures,” Rev. Mod. Phys. 82(3), 2257 (2010).

10 M. F. Limonov, M. V. Rybin, A. N. Poddubny, Y. S. Kivshar, “Fano resonances in photonics,” Nature Photonics 11(9), 543 (2017).

11 A. E. Miroshnichenko and Y. S. Kivshar, “Fano Resonances in All-Dielectric Oligomers,” Nano Lett. 12(12), 6459-6463 (2012).

12 K. E. Chong, B. Hopkins, I. Staude, A. E. Miroshnichenko, J. Dominguez, M. Decker, D. N. Neshev, I. Brener, Y. S. Kivshar, “Observation of Fano resonances in all-dielectric nanoparticle oligomers,” Small 10(10), 1985-1990 (2014).

13 B. Luk’yanchuk, N. I. Zheludev, S. A. Maier, N. J. Halas, P. Nordlander, H. Giessenand, C. T. Chong, “The Fano resonance in plasmonic

nanostructures and metamaterials," Nature Materials 9, 707–715 (2010).
14 M. Rahmani, B. Luk'yanchuk, M. Hong, "Fano resonance in novel plasmonic nanostructures," Laser & Photonics Reviews 7 (3), 329-349 (2013).
15 H. Chew, M. Kerker, "Abnormally Low Electromagnetic Scattering Cross-Sections," J. Opt. Soc. Am. 66, 445-449 (1976).
16 M. Kerker, "Invisible Bodies," J. Opt. Soc. Am. 65, 376-379 (1975).
17 Zarina Sadrieva, Kristina Frizyuk, Mihail Petrov, Yuri Kivshar, and Andrey Bogdanov, "Multipolar origin of bound states in the continuum," Phys. Rev. B 100, 115303 (2019).
18 S. Zhang et al. "Experimental demonstration of near-infrared negative-index metamaterials," Phys. Rev. Lett. 95, 137404 (2005).
19 V. M. Shalaev et al., "Negative index of refraction in optical metamaterials," Opt. Lett. 30, 3356–3358 (2005).
20 N. Yu and F. Capasso, "Flat optics with designer metasurfaces," Nat. Mater. 13, 139–150 (2014).
21 J. B. Pendry, "Negative refraction makes a perfect lens," Phys. Rev. Lett. 85, 3966-3969 (2000).
22 K. G. Balmain and G. V. Elefteriades, Negative-refraction metamaterials (John Wiley & Sons, Inc., 2005).
23 Y. M. Liu, X. Zhang, "Metamaterials: a new frontier of science and technology," Chem. Soc. Rev. 40, 2494-2507 (2011).
24 N. I. Zheludev, "The Road Ahead for Metamaterials," Science 328, 582 (2010).
25 C. M. Soukoulis and M. Wegener, "Optical Metamaterials - More Bulky and Less Lossy," Science 330, 1633 (2010).
26 C. M. Soukoulis and M. Wegener, "Past Achievements and Future Challenges in the Development of Three-Dimensional Photonic Metamaterials," Nat. Photonics 5, 523 (2011).
27 A. Boltasseva and H. A. Atwater, "Low-Loss Plasmonic Metamaterials," Science 331, 290 (2011).
28 H. Lamb, "On Group Velocity," Proc. London Math. Soc. Ser. 2(1), 473 (1904).

29 H. C. Pocklington, “Growth of a Wave-group when the Group-velocity is Negative,” Nature 71, 607 (1905).
30 L. I. Mandelstam, Lectures on optics, relativity and quantum mechanics (Nauka, 1982).
31 D.V. Sivukhin, Optics and spectroscopy (Fizmatgiz 1957).
32 V. G. Veselago, “The electrodynamics of substances with simultaneously negative values of ε and μ,” Sov. Phys. Usp. 10(4), 509-514 (1968).
33 A. N. Lagarkov, V. N. Kissel, “Superresolution and enhancement in metamaterials,” in Proc. of the 2nd Intern. Conf. on Materials for Advanced Technologies, Sym. F: Electromagnetic Materials, SUNTEC, (World Scientific, 2003) p. 157.
34 A. N. Lagarkov, V. N. Kissel, “Near-Perfect Imaging in a Focusing System Based on a Left-Handed-Material,” Plate. Phys. Rev. Lett. 92, 077401 (2004).
35 J. B. Pendry, A. J. Holden, D. J. Robbins, and W. J. Stewart, “Magnetism from Conductors and Enhanced Nonlinear Phenomena,” IEEE Transactions On Microwave Theory And Techniques 47, 11 (1999).
36 D. R. Smith, Willie J. Padilla, D. C. Vier, S. C. Nemat-Nasser and S. Schultz, “Composite Medium with Simultaneously Negative Permeability and Permittivity,” Physical Review Letters 84, 18 (2000).
37 R. A. Shelby, D. R. Smith, S. Schultz, “Experimental Verification of a Negative Index of Refraction,” Science 292(5514), 77–79 (2001).
38 S. A. Schelkunoff, H. T.Friis, Antennas: Theory and Practice (Wiley, 1952).
39 A. N. Kolesnikov et al., Optical and Electrical Properties of Polymers (Material Research Society, 1991).
40 A. N. Lagarkov et al., “Resonance Properties of Bi-Helix Media at Microwaves,” Electromagnetics 17, 213 (1997).
41 N. Fang, X. Zhang, “Imaging properties of a metamaterial superlens,” Appl. Phys. Lett. 82, 161 (2003).
42 D. R. Smith et al., “Limitations on subdiffraction imaging with a negative refractive index slab,” Appl. Phys. Lett. 82, 1506 (2003).

43 C. K. Ong, X. S. Rao, in Proc. of the 2nd Intern. Conf. on Materials for Advanced Technologies, Sym. F: Electromagnetic Materials, SUNTEC, p. 123, (Eds Lim Hock et al.) (Singapore: World Scientific, 2003).
44 X. S .Rao, C. K. Ong, "Subwavelength imaging by a left-handed material superlens," Phys. Rev. E 68, 067601 (2003).
45 V. N. Kissel, A. N. Lagarkov, Proc. of the 2nd Intern. Conf. on Materials for Advanced Technologies, Sym. F: Electromagnetic Materials, SUNTEC, p. 145, (Eds Lim Hock et al.) (Singapore: World Scientific, 2003).
46 A. N. Lagarkov, V. N. Kissel, "Quality of focusing electromagnetic radiation by a plane-parallel slab with a negative index of refraction," Dokl. Phys. 49 5 (2004).
47 V. A. Podolskiy, E. E.Narimanov, "Near-sighted superlens," Opt. Lett. 30, 75 (2005).
48 T. J. Cui et al., "Study of lossy effects on the propagation of propagating and evanescent waves in left-handed materials," Phys. Lett. A 323, 484 (2004).
49 Junxing Liu et al., "Switchable metamaterial for enhancing and localizing electromagnetic field at terahertz band," Optics Express 25(13), 13944-13952 (2017).
50 A. Yang et al., "Real-time tunable lasing from plasmonic nanocavity arrays," Nature Commun. 6, 6939 (2015).
51 T. K. Hakala et al., "Lasing in dark and bright modes of a finite-sized plasmonic lattice," Nature Commun. 8, 13687 (2017).
52 A. H. Schokker, A. F. Koenderink, "Lasing at the band edges of plasmonic lattices," Phys. Rev. B 90, 155452 (2014).
53 W. Zhou et al., "Lasing action in strongly coupled plasmonic nanocavity arrays," Nature Nanotechnol. 8, 506 (2013).
54 M. P. van Exter et al., "Surface plasmon dispersion in metal hole array lasers," Opt. Express 21, 27422 (2013).
55 F. van Beijnum et al., "Surface Plasmon Lasing Observed in Metal Hole Arrays," Phys. Rev. Lett. 110, 206802 (2013).
56 V. T. Tenner, M. J. A. de Dood, M. P. van Exter, "Two-mode surface plasmon lasing in hexagonal arrays," ACS Photon. 3, 942 (2016).

57 X. Meng et al., “Highly directional spacer array for the red wavelength region,” Laser Photon. Rev. 8, 896 (2014).
58 D. P. Fromm, A. Sundaramurthy, P. J. Schuck, G. Kino, and W. E. Moerner, “Gap-dependent optical coupling of single “bowtie” nanoantennas resonant in the visible,” Nano Lett. 4(5), 957–961 (2004).
59 Y. L. Ho, Y. Lee, E. Maeda and J. J. Delaunay, “Coupling of localized surface plasmons to U-shaped cavities for high-sensitivity and miniaturized detectors,” Opt. Express 21(2), 1531–1540 (2013).
60 J. Zhang, J. Yang, X. Wu and Q. Gong, “Electric field enhancing properties of the V-shaped optical resonant antennas,” Opt. Express 15(25), 16852–16859 (2007).
61 H. Wang, D. W. Brandl, F. Le, P. Nordlander and N. J. Halas, “Nanorice: a hybrid plasmonic nanostructure,” Nano Lett. 6(4), 827–832 (2006).
62 B. J. Wiley, Y. Chen, J. M. McLellan, Y. Xiong, Z. Y. Li, D. Ginger, and Y. Xia, “Synthesis and optical properties of silver nanobars and nanorice,” Nano Lett. 7(4), 1032–1036 (2007).
63 S. Lal, S. Link and N. J. Halas, “Nano-optics from sensing to waveguiding,” Nat. Photonics 1(11), 641–648 (2007).
64 S. Link and M. A. El-Sayed, “Spectral properties and relaxation dynamics of surface plasmon electronic oscillations in gold and silver nanodots and nanorods,” J. Phys. Chem. B 103(40), 8410–8426 (1999).
65 C. Yu and J. Irudayaraj, “Multiplex biosensor using gold nanorods,” Anal. Chem. 79(2), 572–579 (2007).
66 H. Chen, X. Kou, Z. Yang, W. Ni and J. Wang, “Shape- and Size-Dependent Refractive Index Sensitivity of Gold Nanoparticles,” Langmuir 24(10), 5233–5237 (2008).
67 M. Moskovits, “Surface-enhanced spectroscopy,” Rev. Mod. Phys. 57(3), 783–826 (1985).
68 A. Ospanova, I. Stenishchev, A. Basharin, “Anapole mode sustaining silicon metamaterials in visible spectral range,” Laser & Photonics Reviews 12 (7), 1800005 (2018).

69 T. Grosjean, M. Mivelle, F. I. Baida, G. W. Burr, and U. C. Fischer, “Diabolo nanoantenna for enhancing and confining the magnetic optical field,” Nano Lett. 11(3), 1009–1013 (2011).
70 Z. Gao, L. F. Shen, E. P. Li, L. L. Xu and Z. Y. Wang, “Cross-diabolo nanoantenna for localizing and enhancing magnetic field with Arbitrary Polarization,” J. Lightwave Technol. 30(6), 829–833 (2012).
71 A. F. Koenderink, R. Tsukanov, J. Enderlein, I. Izeddin and V. Krachmalnicoff, “Super-resolution imaging: when biophysics meets nanophotonics,” Nanophotonics 11 (2), 169-202 (2022).
72 Z. B. Wang, B. S. Luk’yanchuk, W. Guo, S. P. Edwardson, D. J. Whitehead, L. Li, Z. Liu, K. G. Watkins, “The influences of particle number on hot spots in strongly coupled metal nanoparticles chain,” The Journal of chemical physics 128 (9), 094705 (2008).
73 M. Decker, I. Staude, M. Falkner, J. Dominguez, D. N. Neshev, I. Brener, T. Pertsch, Y. S Kivshar, “High-efficiency dielectric Huygens’ surfaces,” Advanced Optical Materials 3(6), 813-820 (2015).
74 A. I Kuznetsov, A. E Miroshnichenko, M. L Brongersma, Y. S Kivshar, B. Luk’yanchuk, “Optically resonant dielectric nanostructures,” Science 354 (6314), aag2472 (2016).
75 A. E. Krasnok, A. E. Miroshnichenko, P. A. Belov, Y. S. Kivshar, “All-dielectric optical nanoantennas,” Optics Express 20 (18), 20599-20604 (2012).
76 S. B. Glybovski, S. A. Tretyakov, P. A. Belov, Y. S. Kivshar, C. R. Simovski, “Metasurfaces: From microwaves to visible,” Physics reports 634, 1-72 (2016).
77 N. I. Zheludev, Y. S. Kivshar, “From metamaterials to metadevices,” Nature materials 11(11), 917 (2016).
78 Wei Liu and Yuri Kivshar, “Multipolar interference effects in nanophotonics,” Philos. T. R. Soc. A. 375 (2017).
79 D. Rainwater et al., “Experimental verification of three-dimensional plasmonic cloaking in free-space,” New J. Phys. 14, 013054 (2012).
80 D. Filonov et al., “Double-shell metamaterial coatings for plasmonic cloaking,” Phys. Status Solidi RRL 6, 46 (2012).

81 A. Alu, D. Rainwater, A. Kerkhoff, “Multifrequency optical invisibility cloak with layered plasmonic shells,” New J. Phys. 12, 103028 (2010).
82 B. Edwards et al., “Experimental Verification of Plasmonic Cloaking at Microwave Frequencies with Metamaterials,” Phys. Rev. Lett. 103, 153901 (2009).
83 P.-Y. Chen et al., “Invisibility and Cloaking Based on Scattering Cancellation,” Adv. Mater. 24 OP281 (2012).
84 B. A. Munk, Frequency Selective Surface: Theory and Design (Wiley, 2000).
85 A. Alu, “Mantle cloak: invisibility induced by a surface,” Phys. Rev. B 80, 245115 (2009).
86 P. -Y. Chen and A. Alu, “Mantle cloaking using thin patterned metasurfaces,” Phys. Rev. B 84, 205110 (2011).
87 P.-Y. Chen et al., “Suppressing the Electromagnetic Scattering With an Helical Mantle Cloak,” IEEE Antennas Propag. Lett. 5, 1598 (2011).
88 P.-Y. Chen, A. Alu, “Atomically Thin Surface Cloak Using Graphene Monolayers,” ACS Nano 5, 5855 (2011).
89 X. J. Ni, Z. J. Wong, M. Mrejen, Y. Wang & X. Zhang, “An ultrathin invisibility skin cloak for visible light,” Science 349, 1310–1314 (2015).
90 C. F. Bohren, “How Can a Particle Absorb More Than the Light Incident on It,” Am. J. Phys. 51, 323-327 (1983).
91 M. G. Silveirinha, A. Alu & N. Engheta, “Cloaking mechanism with antiphase plasmonic satellites,” Phys. Rev. B 78, 205109 (2008).
92 S. J. Oldenburg, R. D. Averitt, S.L. Westcott, N. J. Halas, “Nanoengineering of optical resonances,” Chem. Phys. Lett. 288 (2-4), 243-247.
93 H. Wang, Y. Wu, B. Lassiter, C. L. Nehl, J. H. Hafner, P. Nordlander, N. J. Halas, “Symmetry breaking in individual plasmonic nanoparticles,” Proc. Natl. Acad. Sci. USA 103(29) (2006).
94 Christopher Loo et al., “Gold nanoshell bioconjugates for molecular imaging in living cells,” Opt. Lett. 30, 9, 1012-1014 (2005).
95 C Loo et al., “Nanoshell-enabled photonics-based imaging and therapy of cancer,” Technol. Cancer Res. Treat. 3(1), 33-40 (2004).

96 Nadine Wong Shi Kam, Michael O'Connell, Jeffrey A. Wisdom, Hongjie Dai and Harry B. Gray, "Carbon Nanotubes as Multifunctional Biological Transporters and Near-Infrared Agents for Selective Cancer Cell Destruction," Proceed. of the Nat. Academy of Sciences of the USA 102, 33, 11600-11605 (2005).

97 J. Konig, "Multiphoton microscopy in life sciences," J Microsc. 200(2), 83-104 (2000).

98 B. Liedberg, C. Nylander, I. Lundström, "Biosensing with surface plasmon resonance - how it all started," Biosens. Bioelectron. 10(8) (1995).

99 P. Y. Ufimtsev ,Method of edge waves in the physical theory of diffraction (Dayton, OH: U.S. Air Force, Foreign Technology Division ,1971).

100 Schuck P. "Use of surface plasmon resonance to probe the equilibrium and dynamic aspects of interactions between biological macromolecules," Annual Review of Biophysics and Biomolecular Structure 26, 541-566 (1997).

101 J. Homola, S. Yee, and G. Gauglitz, "Surface Plasmon Resonance Sensors: Review," Sensors and Actuators B 54, 3–15 (1999).

102 D. G. Myszka, R. L. Rich, "Implementing surface plasmon resonance biosensors in drug discovery," Pharm. Sci. Technol. Today. 3(9), 310-317 (2000).

103 A. Paul Alivisatos, Kai P. Johnsson, Xiaogang Peng, Troy E. Wilson, Colin J. Loweth, Marcel P. Bruchez Jr & Peter G. Schultz, "Organization of 'nanocrystal molecules' using DNA," Nature 382, 609–611 (1996).

104 Chad A. Mirkin, Robert L. Letsinger, Robert C. Mucic & James J. Storhoff, "A DNA-based method for rationally assembling nanoparticles into macroscopic materials," Nature 382, 607–609 (1996).

105 Robert Elghanian et al., "Selective Colorimetric Detection of Polynucleotides Based on the Distance-Dependent Optical Properties of Gold Nanoparticles," Science 277, 5329, 1078-1081 (1997).

106 L. R. Hirsch et al., “Nanoshell-mediated near-infrared thermal therapy of tumors under magnetic resonance guidance,” PNAS 100(23), 13549-13554 (2003).
107 Michelle Duval Malinsky et al., “Chain Length Dependence and Sensing Capabilities of the Localized Surface Plasmon Resonance of Silver Nanoparticles Chemically Modified with Alkanethiol Self-Assembled Monolayers,” J. Am. Chem. Soc. 123(7), 1471–1482 (2001).
108 Nidhi Nath, and Ashutosh Chilkoti, “A Colorimetric Gold Nanoparticle Sensor To Interrogate Biomolecular Interactions in Real Time on a Surface,” Anal. Chem. 74(3), 504–509 (2002).
109 Nidhi Nath and Ashutosh Chilkoti, “Label-Free Biosensing by Surface Plasmon Resonance of Nanoparticles on Glass: Optimization of Nanoparticle Size,” Anal. Chem. 76 (18), 5370–5378 (2004).
110 Alexey Basharin, Barbara Cappello, Anar K. Ospanova, Ladislau Matekovits, “Mantle cloaking due to ideal magnetic dipole scattering,” Scientific Reports 10, 2413
111 A. E. Miroshnichenko, A. B. Evlyukhin, Y. F. Yu, R. M. Bakker, A. Chipouline, A. I. Kuznetsov, B. Luk’yanchuk, B. N. Chichkov and Y. S. Kivshar, “Nonradiating anapole modes in dielectric nanoparticles,” Nat. Commun. 6, 8069 (2015).
112 S. Lemak et al., “Toroidal structure and DNA cleavage by the CRISPR associated [4Fe-4S]-cluster containing Cas4 nuclease SSO0001 from Sulfolobus solfataricus,” J. Am. Chem. Soc. 135, 17476–17487 (2013).
113 A. Ceulemans & L. F. Chibotaru, “Molecular anapole moments,” Phys. Rev. Lett. 80, 1861–1864 (1998).
114 N. A. Spaldin, M. Fiebig & M. Mostovoy, “The toroidal moment in condensed-matter physics and its relation to the magnetoelectric effect,” J. Phys. Condens. Matter 20, 434203 (2008).
115 V. Savinov, V. A. Fedotov &, N. I. Zheludev, “Toroidal dipolar excitation and macroscopic electromagnetic properties of metamaterials,” Phys. Rev. B 89, 205112 (2014).
116 Y. W. Huang et al., “Toroidal lasing spaser,” Sci. Rep. 3, 1237 (2013).

117 W. Liu, J. Zhang, B. Lei, H. Hu & A. E. Miroshnichenko, “Invisible nanowires with interfering electric and toroidal dipoles,” Opt. Lett. 40, 2293–2296 (2015).
118 A. D. Boardman, K. Marinov, N. I. Zheludev & V. A. Fedotov, “Dispersion properties of nonradiating configurations: finite-difference time-domain modeling,” Phys. Rev. E 72, 036603 (2005).
119 E. A. Marengo & R. W. Ziolkowski, “Nonradiating sources, the Aharonov Bohm effect and the question of measurability of electromagnetic potentials,” Radio Sci. 37, 10–19 (2002).
120 N. V. Hud & I. D. Vilfan, In Annual Review of Biophysics and Biomolecular Structure (Annual Reviews, 2005).
121 M. M. Hingorani & M. A O’Donnell, “Tale of Toroids in DNA Metabolism,” Nat. Rev. Mol. Cell Biol. 1, 22–30, (2000).
122 A. A. Simpson et al., “Structure of the Bacteriophage Phi 29 DNA Packaging Motor,” Nature 408, 745–750 (2000).
123 V. A. Fedotov, K. Marinov, A. D. Boardman & N. I. Zheludev, “On the Aromagnetism and Anapole Moment of Anthracene Nanocrystals,” New J. Phys. 9, 95–95 (2007).
124 V. I. Kukulin, V. Krasnopolsky, and J. Horˊacek, Theory of resonances: Principles and Applications (Springer Science & Business Media, 2013).
125 C. W. Hsu, B. Zhen, A. D. Stone, J. D. Joannopoulos, and M. Soljaˇci ´c, “Bound states in the continuum,” Nature Reviews Materials 1, 1 (2016).
126 V. Fedotov, M. Rose, S. Prosvirnin, N. Papasimakis, and N. Zheludev, “Sharp trapped-mode resonances in planar metamaterials with a broken structural symmetry,” Physical Review Letters 99, 147401 (2007).
127 J. Lee, B. Zhen, S.-L. Chua, W. Qiu, J. D. Joannopoulos, M. Soljaˇcíc, and O. Shapira, “Observation and differentiation of unique high-q optical resonances near zero wave vector in macroscopic photonic crystal slabs,” Physical Review Letters 109, 067401 (2012).

128 C. W. Hsu, B. Zhen, J. Lee, S.-L. Chua, S. G. Johnson, J. D. Joannopoulos, and M. Solja ˇcí c, “Observation of trapped light within the radiation continuum,” Nature 499, 188 (2013).
129 S. Campione, S. Liu, L. I. Basilio, L. K. Warne, W. L. Langston, T. S. Luk, J. R. Wendt, J. L. Reno, G. A. Keeler, I. Brener, et al., “Broken symmetry dielectric resonators for high quality factor fano metasurfaces,” ACS Photonics 3, 2362 (2016).
130 K. Koshelev, A. Bogdanov, and Y. Kivshar, “Meta-optics and bound states in the continuum,” Science Bulletin 64, 836 (2019).
131 D. Marinica, A. Borisov, and S. Shabanov, “Bound states in the continuum in photonics,” Physical Review Letters 100, 183902 (2008).
132 K. Koshelev, S. Lepeshov, M. Liu, A. Bogdanov, and Y. Kivshar, “Asymmetric metasurfaces with high-q resonances governed by bound states in the continuum,” Physical Review Letters 121, 193903 (2018).
133 J. Jin, X. Yin, L. Ni, M. Solja ˇcí c, B. Zhen, and C. Peng, “Topologically enabled ultrahigh-q guided resonances robust to out-of-plane scattering,” Nature 574, 501 (2019).
134 W. Suh, M. Yanik, O. Solgaard, and S. Fan, “Displacement-sensitive photonic crystal structures based on guided resonance in photonic crystal slabs,” Applied Physics Letters 82, 1999 (2003).
135 A. F. Sadreev, D. N. Maksimov, and A. S. Pilipchuk, “Gate controlled resonant widths in double-bend waveguides: bound states in the continuum,” Journal of Physics: Condensed Matter 27, 295303 (2015).
136 V. Liu, M. Povinelli, and S. Fan, “Resonance-enhanced optical forces between coupled photonic crystal slabs,” Optics express 17, 21897 (2009).
137 M. V. Rybin, K. L. Koshelev, Z. F. Sadrieva, K. B. Samusev, A. A. Bogdanov, M. F. Limonov, and Y. S. Kivshar, “High-Q supercavity modes in subwavelength dielectric resonators,” Physical review letters 119, 243901 (2017).
138 Y. Plotnik, O. Peleg, F. Dreisow, M. Heinrich, S. Nolte, A. Szameit, and M. Segev, “Experimental observation of optical bound states in the continuum,” Phys. Rev. Lett. 107, 183901 (2011).

139 S. Weimann, Y. Xu, R. Keil, A. E. Miroshnichenko, A. T ¨unnermann, S. Nolte, A. A. Sukhorukov, A. Szameit, and Y. S. Kivshar, "Compact surface fano states embedded in the continuum of waveguide arrays," Physical Review Letters 111, 240403 (2013).
140 J. D. Joannopoulos, S. G. Johnson, J. N. Winn, and R. D. Meade, "Molding the flow of light," Princet. Univ. Press. Princeton, NJ [ua] (2008).
141 D. R. Smith, J. B. Pendry, and M. C. Wiltshire, "Metamaterials and negative refractive index," Science 305, 788 (2004).
142 A. Lagarkov and V. Kissel, "Near-perfect imaging in a focusing system based on a left-handed-material plate," Phys. Rev. Lett. 92, 077401 (2004).
143 X. You, C. Fumeaux, and W. Withayachumnankul, "Tutorial on broadband transmissive metasurfaces for wavefront and polarization control of terahertz waves," Journal of Applied Physics 131, 061101 (2022).
144 M. Robnik, "A simple separable hamiltonian having bound states in the continuum," Journal of Physics A: Mathematical and General 19, 3845 (1986).
145 M. I. Molina, A. E. Miroshnichenko, and Y. S. Kivshar, "Surface bound states in the continuum," Phys. Rev. Lett. 108, 070401 (2012).
146 A. Jain and C. Shastry, "Bound states in the continuum for separable nonlocal potentials," Phys. Rev. A 12, 2237 (1975).
147 B. Zhen, C. W. Hsu, L. Lu, A. D. Stone, and M. Solja ˇcí c, "Topological nature of optical bound states in the continuum," Phys. Rev. Lett. 113, 257401 (2014).
148 Francillon, René J., Lockheed Aircraft since 1913 (Annapolis, Md.: Naval Institute Press, 1987)
149 Dakota Vannes and ty Steinke, Out of Nowhere: A History of the Military Sniper (Osprey Publishing, 2004).
150 D. W. T. Kent W. McKee, Active Camouflage for infantry headwear applications (Defence Research and Development Canada, Canada, 2007).

151 L. Rayleigh, “On the scattering of light by small particles,” Philos. Mag. 41, 447-454 (1871).
152 D. Bao et al., “All-dielectric invisibility cloaks made of BaTiO3-loaded polyurethane foam,” New J. Phys. 13, 103023 (2011).
153 N. A. Nemkov, A. A. Basharin, and V. A. Fedotov, “Nonradiating sources, dynamic anapole and Aharonov-Bohm effect,” Physical Review B, 95(16) (2017).
154 N. A. Nemkov, I. V. Stenishchev, A. A. Basharin, “Nontrivial nonradiating all-dielectric anapole,” Scientific Reports 7, 1064 (2017).
155 J. S. T. Gongora, A. E. Miroshnichenko, Y. S. Kivshar, and A. Fratalocchi, “Energy equipartition and unidirectional emission in a spaser nanolaser,” Laser and Photonics Reviews 10, 432–440 (2016).
156 J. S. T. Gongora, A. E. Miroshnichenko, Y. S. Kivshar, and A. Fratalocchi, “Anapole nanolasers for mode-locking and ultrafast pulse generation,” Nat. Commun. 8, 15535 (2017).
157 S. D. Liu, Z. X. Wang, W. J. Wang, J. D. Chen, and Z. H. Chen, “High Q-factor with the excitation of anapole modes in dielectric split nanodisk arrays,” Opt Express 25, 22375-22387 (2017).
158 S. Han, L. Q. Cong, F. Gao, R. Singh, H. L. Yang, “Observation of Fano resonance and classical analog of electromagnetically induced transparency in toroidal metamaterials,” Ann. Phys-Berlin 528, 352-357 (2016).
159 W. Liu, Y.S. Kivshar, “Multipolar interference effects in nanophotonics,” Philos. T. R. Soc. A. 375 (2017).
160 Z. Liu, S. Du, A. J. Cui, Z. C. Li, Y. C. Fan, S. Q. Chen, W. X. Li, J. J. Li, C. Z. Gu, “High-Quality-Factor Mid-Infrared Toroidal Excitation in Folded 3D Metamaterials,” Adv Mater. 29 (2017).
161 V. Mazzone, J. S. T. Gongora, A. Fratalocchi, “Near-Field Coupling and Mode Competition in Multiple Anapole Systems,” Appl. Sci-Basel. 7 (2017).
162 T. Raybould, V. A. Fedotov, N. Papasimakis, I. Youngs, N. I. Zheludev, “Exciting dynamic anapoles with electromagnetic doughnut pulses,” Appl. Phys. Lett. 111 (2017).

163 D. W. Watson, S. D. Jenkins, J. Ruostekoski, V. A. Fedotov, N. I. Zheludev, “Toroidal dipole excitations in metamolecules formed by interacting plasmonic nanorods,” Phys. Rev. B 93 (2016).
164 X. L. Zhang, S. B. Wang, Z. F. Lin, H. B. Sun, C. T. Chan, “Optical force on toroidal nanostructures: Toroidal dipole versus renormalized electric dipole,” Phys. Rev. A 92 (2015).
165 W. Liu, B. Lei, J.H. Shi, H.J. Hu, A.E. Miroshnichenko, “Elusive Pure Anapole Excitation in Homogenous Spherical Nanoparticles with Radial Anisotropy,” J Nanomater, (2015).
166 J. D. Jackson, Classical Electrodynamics (Wiley, New York, 1962).
167 B. Zel’dovich, “Electromagnetic interaction with parity violation,” Sov. Phys. JETP, 6, 1184 (1958).
168 G. N. Afanasiev and Y. P. Stepanovsky, “The ElectromagneticField of Elementary Time-Dependent Toroidal Sources,” J. Phys. A 28, 4565 (1995).
169 E. E. Radescu, G. Vaman, “Exact calculation of the angular momentum loss, recoil force, and radiation intensity for an arbitrary source in terms of electric, magnetic, and toroid multipoles,” Physical Review E 65, 046609 (2002).
170 V. M. Dubovik and V. V. Tugushev, “Toroid Moments in Electrodynamics and Solid State Physics,” Phys. Rep. 187, 145 (1990).
171 T. Kaelberer, V. A. Fedotov, N. Papasimakis, D. P. Tsai, and N. I. Zheludev, “Toroidal Dipolar Response in a Metamaterial,” Science 330, 1510–1512 (2010).
172 A. A. Gorbatsevich, O. E. Omelyanovsky, V. I. Tsebro, ”Toroidal ordering in crystals and nanostructures,” UFN 179, 887–897 (2009).
173 S.E. Kopaev, ”Toroidal ordering in crystals,” UFN, 1175-1190 (2009).
174 N. A. Spaldin, M. Fiebig, M. Mostovoy, “The toroidal moment in condensed-matter physics and its relation to the magnetoelectric effect,” J. Phys. Cond Mat. 20, 434203 (2008).
175 A. I. Popov, D. I. Plokhov and A. K. Zvezdin, “Anapole moment and spin-electric interactions in rare-earth nanoclusters,” EPL 87, 67004 (2009).

176 D. I. Plokhov, A. K. Zvezdin, A. I. Popov, “Macroscopic quantum dynamics of toroidal moment in Ising-type rare-earth clusters,” Phys. Rev. B 83, 184415 (2011).
177 A. A. Gorbatsevich et al, ”Magnetoelectricity,” UFN 179, 887–913 (2009).
178 V. Savinov et al, “Toroidal dipolar excitation and macroscopic electromagnetic properties of metamaterials,” Phys. Rev. B 89, 205112 (2014).
179 Alexey A. Basharin, Maria Kafesaki, Eleftherios N. Economou, Costas M. Soukoulis, Vassili A. Fedotov, Vassili Savinov and Nikolay I. Zheludev, “Dielectric metamaterials with toroidal response,” Physical Review X 5, 011036 (2015).
180 N. Papasimakis, V. A. Fedotov, N. I. Zheludev, and S. L. Prosvirnin, “Metamaterial Analog of Electromagnetically Induced Transparency,” Phys. Rev. Lett. 101, 253903 (2008)
181 Z.-G. Dong, P. Ni, J. Zhu, X. Yin, X. Zhang, “Toroidal dipole response in a multifold double-ring metamaterial,” Opt. Express 20, 13065-13070 (2012).
182 L. Y. Guo, M. H. Li, Q. W. Ye, B. X. Xiao, H. L. Yang, “Electric toroidal dipole response in split-ring resonator metamaterials,” Eur. Phys. J. B 85, 1-5 (2012).
183 Y. Fan, Z. Wei, H. Li, H. Chen, C. M. Soukoulis, “Low-loss and high-Q planar metamaterial with toroidal moment,” Physical Review B 87, 115417 (2013).
184 Y.-W. Huang et al., “Design of plasmonic toroidal metamaterials at optical frequencies,” Opt. Express 20, 1760-1768 (2012).
185 B. Ogut et al., “Toroidal Plasmonic Eigenmodes in Oligomer Nanocavities for the Visible,” Nano Letters 12, 5239-5244 (2012).
186 Zheng-Gao Dong et al., “Optical toroidal dipolar response by an asymmetric double-bar metamaterial,” Appl. Phys. Lett. 101 (2012).
187 Yao-Wei Huang et al., “Toroidal Lasing Spaser,” Scientific Reports 3, 1237 (2013).

188 H. Raether, “Surface Plasmons on Smooth and Rough Surfaces and on Gratings,” Springer Tracts in Modern Physics, Springer-Verlag, Berlin (1904).
189 A. Alu and N. Engheta, “Achieving transparency with plasmonic and metamaterial coatings,” Phys. Rev. E 72(1), 016623 (2005).
190 Z. G. Dong et al., “All-optical Hall effect by the dynamic toroidal moment in a cavity-based metamaterial,” Physical Review B 87 (2013)
191 J. H. Yan et al., “Magnetically induced forward scattering at visible wavelengths in silicon nanosphere oligomers,” Nat. Commun. 6 (2015).
192 A. B. Evlyukhin et al., “Demonstration of Magnetic Dipole Resonances of Dielectric Nanospheres in the Visible Region,” Nano Lett. 12, 3749-3755 (2012).
193 D. Zhang et al., “Magnetic Fano resonance of heterodimer nanostructure by azimuthally polarized excitation,” Opt Express 25, 26704-26713 (2017).
194 I. Staude, J. Schilling, “Metamaterial-inspired silicon nanophotonics,” Nat. Photonics 11, 274-284 (2017).
195 A. Mirzaei, A. E. Miroshnichenko, I. V. Shadrivov, Y. S. Kivshar, “All-Dielectric Multilayer Cylindrical Structures for Invisibility Cloaking.,”Sci. Rep. 5 (2015).
196 A. I. Kuznetsov, A. E. Miroshnichenko, M. L. Brongersma, Y. S. Kivshar, B. Luk’yanchuk, “Optically resonant dielectric nanostructures,” Science 354 (2016).
197 A. B. Evlyukhin, T. Fischer, C. Reinhardt, B. N. Chichkov, “Optical theorem and multipole scattering of light by arbitrarily shaped nanoparticles,” Phys. Rev. B. 94 (2016).
198 T. Ergin et al., “Three-dimensional invisibility cloak at optical wavelengths,” Science 328, 337 (2010).
199 S. Dai et al., “Subdiffractional focusing and guiding of polaritonic rays in a natural hyperbolic material,” Nature Commun. 6, 6963 (2015).
200 J. C. W. Song, M. S. Rudner, “Chiral plasmons without magnetic field,” Proc. Natl. Acad. Sci. USA 113 4658 (2016).

201 A. Kumar et al., “Chiral plasmon in gapped Dirac systems,” Phys. Rev. B 93, 041413(R) (2016).
202 C. Pfeiffer, A. Grbic, “Metamaterial Huygens’ Surfaces: Tailoring Wave Fronts with Reflectionless Sheets,” Phys. Rev. Lett. 110 (2013).
203 C. Y. Li et al., “Optical Anapole Metamaterial,” ACS Nano 12 (2), 1920-1927 (2018).
204 M. Decker, I. Staude, “Resonant dielectric nanostructures: a low-loss platform for functional nanophotonics,” J. Optics-Uk 18 (2016).
205 B. Luk’yanchuk, R. Paniagua-Dominguez, A. I. Kuznetsov, A. E. Miroshnichenko, Y. S. Kivshar, “Suppression of scattering for small dielectric particles: anapole mode and invisibility,” Philos. T. R. Soc. A 375 (2017).
206 B. Luk’yanchuk, R. Paniagua-Dominguez, A. I. Kuznetsov, A. E. Miroshnichenko, Y. S. Kivshar, “Hybrid anapole modes of high-index dielectric nanoparticles,” Phys. Rev. A. 95 (2017).
207 A. I. Kuznetsov, A. E. Miroshnichenko, Y. H. Fu, J. B. Zhang, B. Luk’yanchuk, “Magnetic light,” Sci. Rep. 2 (2012).
208 M. A. van de Haar, J. van de Groep, B. J. M. Brenny, A. Polman, “Controlling magnetic and electric dipole modes in hollow silicon nanocylinders,” Opt. Express 24, 2047-2064 (2016).
209 W. Liu, A. E. Miroshnichenko, “Scattering Invisibility With Free-Space Field Enhancement of All-Dielectric Nanoparticles,” Laser Photonics Rev. 11 (2017).
210 Y. H. Fu, A. I. Kuznetsov, A. E. Miroshnichenko, Y. F. Yu, B. Luk’yanchuk, “Directional visible light scattering by silicon nanoparticles,” Nat. Commun. 4 (2013).
211 R. W. Wood, “The invisibility of transparent objects,” Phys. Rev. 15(2), 123-124 (1902).
212 G. Gbur, “Invisibility physics: past, present, and future,” Prog. Optics 58, 65-114 (2013).
213 U. Leonhardt, “Optical conformal mapping,” Science 312, 1777-1780 (2006).

214 S. Guenneau, C. Amra, and D. Veynante, “Transformation thermodynamics: cloaking and concentrating heat flux,” Opt. Express 20(7), 8207-8218 (2012).
215 I. Fernandez-Corbaton, S. Nanz and C. Rockstuhl, “On the dynamic toroidal multipoles from localized electric current distributions,” Sci. Rep. 7, 7527 (2017).
216 M. Babinet, “Babinet’s principle and the band structure of surface waves on patterned metal arrays,” C. R. Acad. Sci. 4, 638 (1837)
217 K. Kempa, “Percolation effects in the checkerboard Babinet series of metamaterial structures,” Phys. Status Solidi RRL 4, 8–9, 218–220 (2010)
218 F. Falcone, T. Lopetegi, M. A. G. Laso, J. D. Baena, J. Bonache, M. Beruete, R. Marquer's, F. Martıı'n, and M. Sorolla, “Babinet Principle Applied to the Design of Metasurfaces and Metamaterials,” Phys. Rev. Lett. 93, 19 19740 (2004)
219 Yoshiro Urade, Yosuke Nakata, Toshihiro Nakanishi, and Masao Kitano, “Frequency-Independent Response of Self-Complementary Checkerboard Screens,” Physical Review Letters 114, 237401 (2015).
220 Yoshiro Urade, Yosuke Nakata, Kunio Okimura, Toshihiro Nakanishi, Fumiaki Miyamaru, Mitsuo W. Takeda, and Masao Kitano, “Dynamically Babinet-invertible metasurface: a capacitive-inductive reconfigurable filter for terahertz waves using vanadium-dioxide metal-insulator transition,” Opt. Exp. 24, 4405–4410 (2016).
221 Yoshiro Urade, Yosuke Nakata, Toshihiro Nakanishi, and Masao Kitano, “Broadband and energy-concentrating terahertz coherent perfect absorber based on a self-complementary metasurface,” Opt. Lett. 41, 4472–4475 (2016).
222 Yoshiro Urade, Yosuke Nakata, Toshihiro Nakanishi, and Masao Kitano, “Theoretical study on dynamical planar-chirality switching in checkerboard-like metasurfaces,” EPJ Applied Metamaterials 4, 2 (2017).
223 Yosuke Nakata, Yoshiro Urade, Toshihiro Nakanishi, and Masao Kitano, “Plane-wave scattering by self-complementary metasurfaces

in terms of electromagnetic duality and Babinet's principle," Phys. Rev. B 88, 205138 (2013).
224 Yosuke Nakata, Yoshiro Urade, Kunio Okimura, Toshihiro Nakanishi, Fumiaki Miyamaru, Mitsuo W. Takeda, and Masao Kitano, "Anisotropic Babinet-Invertible Metasurfaces to Realize Transmission-Reflection Switching for Orthogonal Polarizations of Light," Phys. Rev. Appl. 6, 044022 (2016).
225 K. Takano, F. Miyamaru, K. Akiyama, H. Miyazaki, M. W. Takeda, Y. Abe, Y. Tokuda, H. Ito, and M. Hangyo, "Crossover from capacitive to inductive electromagnetic responses in near self-complementary metallic checkerboard patterns," Optics Express, 22, 24787-24795, (2014).
226 R. E. Raab and O. L. De Lange, Multipole Theory in Eectromagnetism: Classical, Quantum, and Symmetry Aspects, with Applications (Oxford University Press, Oxford, 2004).
227 P. De Visschere, "On the origin dependence of multipole moments in electromagnetism," J. Phys. D 39, 4278 (2006).
228 R. Raab and O. De Lange, Comment on "On the origin dependence of multipole moments in electromagnetism," J. Phys. D 43, 508001 (2010).
229 A. Vinogradov, "Electrodynamics of composite materials (inRussian)", M.: Editorial URCC 208, 2 (2001).
230 I. P. Theron and J. H. Cloete, "The electric quadrupole contribution to the circular birefringence of nonmagnetic anisotropic chiral media: A circular waveguide experiment," IEEE Trans. Microwave Theory Tech. 44, 1451 (1996).
231 V. R. Tuz, V. Dmitriev, and A. B. Evlyukhin, "Antitoroidic and toroidic orders in all-dielectric metasurfaces for optical near-field manipulation," ACS Appl. Nano Mater. 3, 11315 (2020).
232 Knott, E. F., Shaeffer, J. F. Tuley, and M. T. Radar Cross Section 231 (Artech House, 1993).
234 Balanis, C. A. Antenna Theory: Analysis and Design (Wiley, 2005).
235 Balanis, C. A. Advanced Engineering Electromagnetics (Wiley, 2012).

236 M. Meier, A. Mekis, A. Dodabalapur, A. Timko, R. Slusher, J. Joannopoulos, and O. Nalamasu, “Laser action from two-dimensional distributed feedback in photonic crystals”, Appl. Phys. Lett. 74, 7 (1999).
237 M. Imada, S. Noda, A. Chutinan, T. Tokuda, M. Murata, and G. Sasaki, “Coherent two-dimensional lasing action in surface-emitting laser with triangular-lattice photonic crystal structure”, Appl. Phys. Lett.75, 316 (1999).
238 S. Noda, M. Yokoyama, M. Imada, A. Chutinan, and M. Mochizuki, “Polarization mode control of twodimensional photonic crystal laser by unit cell structure design,” Science 293, 1123 (2001).
239 E. Miyai, K. Sakai, T. Okano, W. Kunishi, D. Ohnishi, and S. Noda, “Lasers producing tailored beams,” Nature 441, 946 (2006).
240 H. Matsubara, S. Yoshimoto, H. Saito, Y. Jianglin, Y. Tanaka, and S. Noda, “GaN photonic-crystal surface-emitting laser at blue-violet wavelengths,” Science 319(5862), 445-7 (2008).
241 A. A. Yanik, A. E. Cetin, M. Huang, A. Artar, S. H. Mousavi, A. Khanikaev, J. H. Connor, G. Shvets, and H. Altug, “Seeing protein monolayers with naked eye through plasmonic fano resonances,” Proceedings of the National Academy of Sciences 108, 11784 (2011).
242 B. Zhen, S.-L. Chua, J. Lee, A. W. Rodriguez, X. Liang, S. G. Johnson, J. D. Joannopoulos, M. Solja ˇcí c, and O. Shapira, “Enabling enhanced emission and low- hreshold lasing of organic molecules using special fano resonances of macroscopic photonic crystals,” Proceedings of the National Academy of Sciences 110, 13711 (2013).
243 J. M. Foley, S. M. Young, and J. D. Phillips, “Symmetry-protected mode coupling near normal incidence for narrow-band transmission filtering in a dielectric grating,” Physical Review B 89, 165111 (2014).
244 V. I. Kukulin, V. Krasnopolsky, and J. Hor ́acek, Theory of resonances: Principles and Applications (Springer Science & Business Media, 2013)
245 A. Ospanova, M. Cojocari, P. Lamberti, A. Plyushch, L. Matekovits, Yu. Svirko, P. Kuzhir, A. Basharin, “Broadband transparency of Babinet complementary metamaterials,” Appl. Phys. Lett. 122, 231702 (2023)

246 C. W. Hsu, B. Zhen, A. D. Stone, J. D. Joannopoulos, and M. Solja ˇcí c, “Bound states in the continuum,” Nature Reviews Materials 1, 1 (2016)

APPENDICES

APPENDIX 1. PERMISSIONS FOR FIGURES PUBLICATION

Figure 1.2.3

Adapted from [Hsu, C., Zhen, B., Stone, A. et al. Bound states in the continuum. Nat Rev Mater 1, 16048 (2016). https://doi.org/10.1038/natrevmats.2016.48], with the permission of Springer Nature.

Figure 3.1, Figure 4.1.1, Figure 4.1.2, Figure 4.1.3, Figure 4.1.4, Figure 4.1.5, Figure 4.1.6, Figure 4.1.7

Reprinted from [Mikhail M. Bukharin, Vladimir Ya. Pecherkin, Anar K. Ospanova, Vladimir B. Il'in, Leonid M. Vasilyak, Alexey A. Basharin & Boris Luk'yanchuk, " Transverse Kerker effect in all-dielectric spheroidal particles," Scientific Reports 12, 7997 (2022)], with the permission of Springer Nature.

Figure 4.2.2, Figure 4.2.3, Figure 4.2.4, Figure 4.2.5

Reprinted from [A. Ospanova, M. Cojocari, P. Lamberti, A. Plyushch, L. Matekovits, Yu. Svirko, P. Kuzhir, A. Basharin, "Broadband transparency of Babinet complementary metamaterials," *Appl. Phys. Lett.* 122, 231702 (2023)], with the permission of AIP Publishing.

ARTICLES

ARTICLE I

A. Ospanova, M. Cojocari, and A. Basharin
“Modified multipoles in photonics”
Phys. Rev. B 107, 035156 (2023)

ARTICLE II

M. M. Bukharin, V. Ya. Pecherkin, A. K. Ospanova, V. B. Il’in,
L. M. Vasilyak, A. A. Basharin and B. Luk‘yanchuk
“Transverse Kerker effect in all-dielectric spheroidal particles”
Scientific Reports 12, 7997 (2022)

ARTICLE III

A. Ospanova, M. Cojocari, P. Lamberti, A. Plyushch, L. Matekovits, Yu. Svirko, P. Kuzhir, A. Basharin
“Broadband transparency of Babinet complementary metamaterials”
Appl. Phys. Lett. 122, 231702 (2023)

ARTICLE I

A. Ospanova, M. Cojocari, and A. Basharin
"Modified multipoles in photonics"
Phys. Rev. B 107, 035156 (2023)

ARTICLE II

M. M. Bukharin, V. Ya. Pecherkin, A. K. Ospanova, V. B. Il'in, L. M. Vasilyak, A. A. Basharin and B. Luk'yanchuk

"Transverse Kerker effect in all-dielectric spheroidal particles"

Scientific Reports 12, 7997 (2022)

scientific reports

Check for updates

OPEN

Transverse Kerker effect in all-dielectric spheroidal particles

Mikhail M. Bukharin[1], Vladimir Ya. Pecherkin[2], Anar K. Ospanova[1,3], Vladimir B. Il'in[4,5,6], Leonid M. Vasilyak[2], Alexey A. Basharin[3,7]✉ & Boris Luk'yanchuk[8]

Kerker effect is one of the unique phenomena in modern electrodynamics. Due to overlapping of electric and magnetic dipole moments, all-dielectric particles can be invisible in forward or backward directions. In our paper we propose new conditions between resonantly excited electric dipole and magnetic quadrupole in ceramic high index spheroidal particles for demonstrating transverse Kerker effect. Moreover, we perform proof-of-concept microwave experiment and demonstrate dumbbell radiation pattern with suppressed scattering in both forward and backward directions and enhanced scattering in lateral directions. Our concept is promising for future planar lasers, nonreflected metasurface and laterally excited waveguides and nanoantennas.

Recently, the studies of light manipulation in electromagnetic structures have emerged as promising scientific fields due to unusual multipoles interactions in subwavelength all-dielectric and plasmonic particles[1]. The transition from electronic systems and information processing methods to optical ones strongly requires development of high Q-factor open resonators and nanoantennas enabling effective light controlling at the nanoscale in optical microcircuits[2]. However, an implementation of strongly resonance nanoparticles requires complex geometries at nanoscale and forces to search for qualitatively new solutions[3].

In this issue, all-dielectric photonics brings the idea of resonant scattering on dielectric particles based on the so-called Mie resonances[4]. Firstly introduced for spherical particles, its definition was extended to particles of various shapes and based on electromagnetic multipoles interactions. There is a plenty of research on dielectric particles of different geometries demonstrating strong fields localizations, Fano-resonances[5], Kerker conditions[6], anapole modes[7], invisible metasurfaces[8] and Bound states in the continuum (BIC)[9].

Primarily, invisible physics inspired us to study multipolar interference between multipoles of so-called trivial and nontrivial families[6]. For instance first and second Kerker effects are results of interaction between electric and magnetic dipole moments fulfilling condition for zero backward or forward scattering[10,11]. Similarly, Kerker effect can be observed in interaction between quadrupoles of electric and magnetic types[6]. For the first time, Kerker effect was experimentally demonstrated for ceramic sphere in microwave[12] and then for silicon nanosphere[13] and gallium arsenide nano-disks in optics[14]. The main problem for demonstrating Kerker effects in all-dielectric particles is overlapping between resonances of electric and magnetic dipole moments in the same frequency[15]. For example, the magnetic and electric dipole resonances are separated from each other for silicon nanosphere. The solution can be found in the application of spheroidal particles giving optimum aspect ratio for overlapping electric and magnetic resonances provide suppressed backward scattering and strong forward scattering[16].

The second level of Kerker-scattering can be defined as suppression of radiation in both forward and backward directions and named as *generalized Kerker effect*[6,17]. In this issue, the particles of disks, cuboids shape[18] and onions multilayer particles[17] can be considered invisible due to interactions between electric and magnetic dipoles as well as between their quadrupoles. Moreover, metasurfaces based on them are almost transparent and unaccompanied by phase change with light transmission[8]. From practical applications, simultaneous excitation of Kerker's first and second conditions becomes crucially important for strong near-field localization and developing of nonreflected metasurfaces for advanced photonic technologies.

For the first glance, generalized Kerker effect may seem similar to electric and magnetic anapole states and hybrid anapole as well[19–21]. However, the main difference is that generalized Kerker effect is accompanied by transverse scattering while anapole particle does not scatter at all exceptionally up to higher multipoles in

[1]National University of Science and Technology "MISiS", Moscow 119049, Russia. [2]Joint Institute for High Temperatures, Russian Academy of Sciences, Moscow 125412, Russia. [3]Department of Physics and Mathematics, Institute of Photonics, University of Eastern Finland, Joensuu 80101, Finland. [4]Dept. Math. Mechan., St. Petersburg State University, St. Petersburg 198504, Russia. [5]Petersburg University of Aerospace Instrumentation, St. Petersburg 190000, Russia. [6]Main (Pulkovo) Astronomical Observatory of RAS, St. Petersburg 196140, Russia. [7]Institute for Theoretical and Applied Electromagnetics RAS, Moscow 125412, Russia. [8]Faculty of Physics, Lomonosov Moscow State University, Moscow 119991, Russia. ✉email: Alexey.basharin@gmail.com

agreement with optical theorem[22–26]. On the other hand, the side scattering property can be usefully exploited for metasurfaces as a platform for planar lasers via transverse Kerker effect as coupling between near fields of particles and for lateral excitation of nano-waveguides[2,8,18].

For this aim, we theoretically propose and demonstrate via proof-of-concept microwave experiment an intensive lateral scattering by spheroidal all-dielectric particle. We demonstrate this effect on the spheroidal particle with the aspect ratio close to 2.1 between resonantly coincidental electric dipole and magnetic quadrupole moments which gives transverse radiation pattern of dumbbell form in the selected direction perpendicular to the incident wave front. Experimental results match theoretical results. We should also note that we mean "proof-of-concept" definition for our experiment in order to show transverse Kerker effect, which can be demonstrated also for other shapes of meta-particles and permittivities.

We have previously implemented a number of studies to suppress scattering in an elliptical particle[21] due to hybrid anapole and this work is continuation of these studies. The novelty of the theoretical part of our paper is the optimization of the transverse Kerker effect by choosing the optimal shape of a spheroidal all-dielectric particle. This work originated from a previously published paper[15] which explored the possibility of maximizing forward scattering while completely suppressing backward scattering by choosing the shape of a spheroid particle. Moreover, In our work, we analyzed for the first time the possibility of maximizing the transverse Kerker effect for a spheroidal particle. In this paper, we theoretically involve the interaction between electric dipole and magnetic quadrupole moments. We find the formulas for a description of the interference conditions needed for longitudinal and transverse dumbbell scattering. These conditions describe relative amplitude and phases of electric dipole and magnetic quadrupole excited in spheroidal particles.

To confirm the proposed transverse Kerker effect origin of dumbbell scattering, we experimentally observe for the first time the radiation pattern of spheroidal particle in the microwave regime.

We note that the study of electromagnetic response of spheroidal particles is significant by several reasons. Dust grains in the interplanetary and interstellar medium are assumed to have spheroidal shape[27], and their response may be explained by our approach. Moreover, spheroidal particles are equally important for the problem of atmosphere optics[28], medicine and microbiology[29].

Additionally, resonant scattering phenomena have been demonstrated in another nonspherical particles. Nonradiating mode conditioned by so-called hybrid anapole establishment demonstrated in high-index dielectric ellipsoidal particles[21] and in all-dielectric nanocylinders[30].

Dumbbell radiation due to multipoles interaction

We start with finding of the transverse scattering conditions from the multipole decomposition of the field radiated by the arbitrary particle[31]. We note that transverse Kerker effect is interpreted as suppression of both scattering in forward and backward directions providing enhanced scattering in lateral directions[18].

In our consideration, we use only families of dipoles and quadrupoles.

The radiation of arbitrary source is formulated by electric field of multipoles. For l=1, radiation is presented by electric and magnetic dipoles, while for l=2 by electric and magnetic quadrupoles:

$$\begin{aligned}
&\mathbf{E}_{(total)}(\theta,\varphi,r) \approx \mathbf{E}_{(l=1)} + \mathbf{E}_{(l=2)},\\
&\mathbf{E}_{(l=1)}(\theta,\varphi,r) \approx \frac{\mu_0 c^2}{3\sqrt{2\pi}} \frac{\exp(-ikr)}{r} \sum_{m=0,\pm1} \Big[\big(k^2 Q_{1,m} - ik^3 T_{1,m}\big)\\
&\quad \times \Big(\mathbf{Y}_{1,2,m} + \sqrt{2}\mathbf{Y}_{1,0,m}\Big) + i\sqrt{3}\big(k^2 M_{1,m} \times \mathbf{Y}_{1,1,m}\big)\Big],\\
&\mathbf{E}_{(l=2)}(\theta,\varphi,r) \approx \frac{\mu_0 c^2}{10\sqrt{6\pi}} \frac{\exp(-ikr)}{r} \sum_{m=0,\pm1,\pm2} \Big[ik^3 Q^{(e)}_{2,m} \times (\sqrt{2}\mathbf{Y}_{2,3,m} + \sqrt{3}\mathbf{Y}_{2,1,m})\\
&\quad - \sqrt{5}k^3 Q^{(m)}_{2,m} \times \mathbf{Y}_{2,2,m}\Big].
\end{aligned} \tag{1}$$

Here, μ_0 is the magnetic permeability of vacuum, c is the speed of light, r is the radius-vector, and $\mathbf{Y}_{k,l,m}$ are the spherical vector harmonics. The spherical multipoles are related to the Cartesian multipoles, that is, electric dipole $\boldsymbol{p}$, magnetic dipole $\boldsymbol{M}$, toroidal dipole moment $\boldsymbol{T}$, electric quadrupole Qe, magnetic quadrupole Qm, as follows:

$$Q_{1,0} = p_z, \quad Q_{1,\pm1} = \frac{\mp p_x + ip_y}{\sqrt{2}}, \quad T_{1,0} = T_z, \quad T_{1,\pm1} = \frac{\mp T_x + iT_y}{\sqrt{2}}, \quad M_{1,0} = -M_z, \quad M_{1,\pm1} = \frac{\pm M_x - iM_y}{\sqrt{2}},$$

$$Qe_{2,0} = 3\,Qe_{zz}, \quad Qe_{2,\pm1} = \sqrt{6}\left(\mp Qe_{xz} + iQe_{yz}\right), \quad Qe_{2,\pm2} = \frac{\sqrt{6}}{2}\left(Qe_{xx} \mp i2Qe_{xy} - Qe_{yy}\right),$$

$$Qm_{2,0} = -\frac{3}{2}\,Qm_{zz}, \quad Qm_{2,\pm1} = \sqrt{\frac{3}{2}}\,(\pm Qm_{xz} - iQm_{yz}), \quad Qm_{2,\pm2} = \frac{\sqrt{6}}{4}\,(-Qm_{xx} \pm i2Qm_{xy} + Qm_{yy}).$$

Cartesian multipoles are calculated by integrating over the current density $\boldsymbol{J(r)}$ distribution within the particle volume and $\alpha,\beta,\gamma = x,y,z$:

$$p_\alpha = \frac{1}{i\omega}\int J_\alpha d^3r, \quad m_\alpha = \frac{1}{2c}\int [r\times J]_\alpha d^3r, \quad T_\alpha = \frac{1}{10c}\int \left[(r\cdot J)r_\alpha - 2r^2 J_\alpha\right] d^3r, \quad P_\alpha = -p_\alpha + ikT_\alpha,$$

$$Qe_{\alpha\beta} = \frac{1}{i2\omega}\int \left[r_\beta J_\alpha + r_\alpha J_\beta - \frac{2}{3}(r\cdot J)\delta_{\alpha\beta}\right] d^3r, \quad Qm_{\alpha\beta} = \frac{1}{3c}\int \left[r_\alpha [r\times J]_\beta + r_\beta [r\times J]_\alpha\right] d^3r.$$

Here $\delta_{\alpha\beta}$ is the Kronecker symbol.

The scattering cross section of the particle can be described by terms of multipoles:

$$\sigma_{scat} = \frac{k^4}{6\pi\varepsilon_0^2|E_0|}\left(|M|^2 + |P|^2\right) + \frac{k^6}{80\pi\varepsilon_0^2|E_0|}\left(4|Qe_{\alpha\beta}|^2 + |Qm_{\alpha\beta}|^2\right). \tag{2}$$

Let us suppose two transverse scattering cases, mutually perpendicular to each other:

1. $\theta = 0$ and $\theta = \pi$. In this case multipoles radiate only in transverse to incident wave direction and scattering fields $\boldsymbol{E}_{(total)}(\theta{=}0) = 0$ and $\boldsymbol{E}_{(total)}(\theta{=}\pi) = 0$.
2. $\theta = \pi/2$ and $\theta = 3\pi/2$. In this case multipoles radiate only along incident wave direction and scattering fields $\boldsymbol{E}_{(total)}(\theta{=}\pi/2) = 0$ and $\boldsymbol{E}_{(total)}(\theta{=}3\pi/2) = 0$.

From Eq. (1) one can simply find solution for conditions 1 and 2 (see "Methods"), and we get relations between electric dipole $\boldsymbol{P}$ and magnetic quadrupole Q_m. However, we imply other multipoles have insufficient response in our system:

$$P_\alpha = -\frac{ik}{2}Qm_{\beta\gamma}, \tag{3}$$

$$P_\alpha = \frac{ik}{2}Qm_{\beta\gamma}. \tag{4}$$

The same conditions can be obtained for magnetic dipole and electric quadrupole.

This simple result reveals that zero radiation (Transverse Kerker effect) simultaneously in backward and forward directions, Condition 1, Eq. (3) or simultaneously in lateral directions (Longitudinal Kerker effect) Condition 2, Eq. (4) can be achievable just by interference between two multipoles of electric dipole moment and magnetic quadrupole. Moreover, the radiation direction is almost defined by phase of magnetic quadrupole which indicated by its sign. Similar results were obtained numerically by Asano & Yamamoto[32], but without explaining the reason for side scattering.

Recently, Jeng Yi Lee et al.[17] formulated conditions for simultaneously nearly zero forward and backward scattering. It is possible when the first (dipoles) and second (quadrupoles) order multipoles excited in particle obey the condition $a_1 = -5/3\, b_2$ and $b_1 = -5/3\, a_2$. However, for simple all-dielectric sphere the coexistence of electric and magnetic dipoles and their quadrupoles is impossible at the same frequencies. Then, the multilayer structures[17], spherical particles with radial anisotropy give chance for experimental evidence of transverse Kerker effect[33].

To realize this unique property, let us consider the electromagnetic scattering by high-index dielectric spheroidal particle with a and b being the major and minor semiaxis, respectively. The aspect ratio a/b indicates the spheroidal shape changing from needle ($a/b > 1$, prolate spheroid), passing by sphere ($a/b{=}1$), to disk ($a/b < 1$, oblate spheroid). During our experimental study, we suppose the case of prolate spheroid with $a = 19.5/2$ mm and $b = 12.5/2$ mm, and ratio $a/b = 1.56$. The dielectric permittivity of particle is $\varepsilon = 150$ that presented as high-index ceramics. The particle is illuminated by plane wave at lateral incidence with polarization of vector $\boldsymbol{E}$ parallel to the minor spheroidal axis x. The particle geometry and excited wave are depicted in Fig. 1.

In our paper, we demonstrate spheroidal all-dielectric particle as promising for demonstration of transverse Kerker effect due to extra radius as a channel for multipoles tunability in comparison with sphere.

For this, we consider the spheroid with shape given by equation:

$$\frac{x^2}{b^2} + \frac{y^2}{a^2} + \frac{z^2}{b^2} = 1 \tag{5}$$

In order to demonstrate transverse scattering approach, we perform simulation of electromagnetic scattering by spheroidal particles of different ratio a/b (Fig. 2). We use commercial version of CST Microwave Studio and Time domain solver with open boundary conditions. The particle is illuminated by a plane wave with linearly polarized $\boldsymbol{E}$ component (Fig. 1). The scattering cross section σ is normalized to $\sigma/\pi ab$. For small ratio $a/b < 1$, the particle is of disk shape and its scattering spectrum is defined by two main resonances where magnetic dipole moment M is the first term and electric dipole P is the second one. This trend is not changing up to $a/b = 1$, i.e. transition of disk to the sphere. We observe that the bifurcation point $a/b = 1$ and $q = 1.1$ is splitting into two resonances for $a/b > 1$. Both of them are characterized by electric dipole moment and magnetic quadrupole moment. However, the main difference between them is determined in the phases of the magnetic quadrupoles. For the first case (Transverse scattering), electric dipole moment P_x and magnetic quadrupole Qm_{yz} components have positive sign of phases, while the second resonance (Longitudinal scattering) is characterized by the opposite sign of phases (Fig. 2).

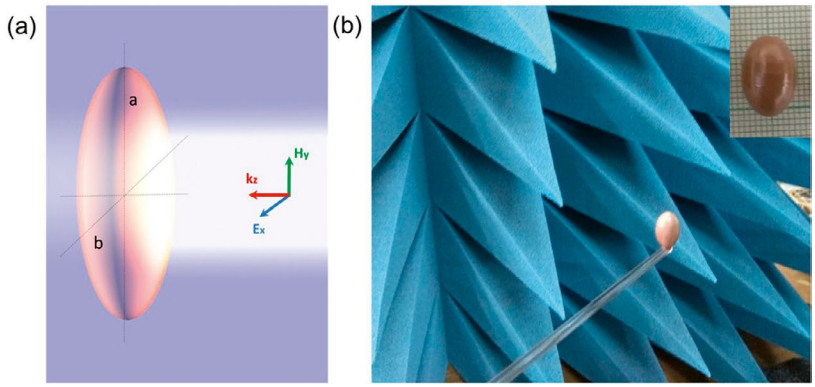

Figure 1. (**a**) Illustration of high-index dielectric prolate spheroidal particle with dielectric permittivity ε=150 and the major and minor semiaxes of a and b, respectively. Linearly polarized plane wave is impinging laterally with vector $\boldsymbol{E}$ parallel to minor axis. (**b**) Experimental sample of ceramic spheroidal particle with a = 19.5/2 mm and b = 12.5/2 mm in anechoic chamber. The inset shows picture of sample.

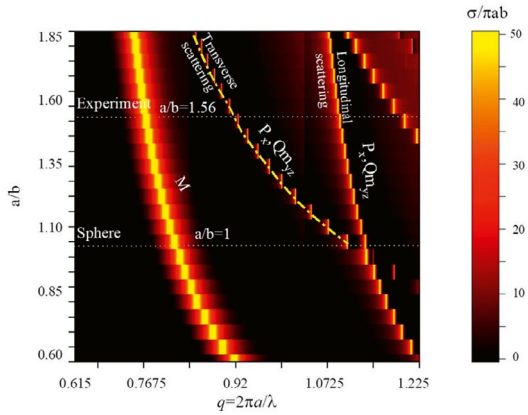

Figure 2. Normalized scattering cross-section of spheroidal all-dielectric particles depending on their aspect ratio a/b and size parameter $q = 2\pi a/\lambda$. Experimental cross-section obtained for a/b=1.56 demonstrates three peaks, two of them are related to transverse and longitudinal scatterings.

To propose features of electromagnetic response of prolate spheroid ($a/b > 1$) and their modes, we consider the spectra calculated by CST Microwave Studio of particle with a/b=1.56 and demonstrate its experimental scattering cross-section (Fig. 3). The resonance peeks on 1.8 GHz, 2.17 GHz and 2.65 GHz demonstrate good agreement between theory and experiment.

In order to clearly understand the origin of peaks, we perform multipole decomposition of four main multipoles excited in system, where $\boldsymbol{P}$ means electric dipoles, $\boldsymbol{M}$ magnetic ones, Qe electric quadrupoles and Qm magnetic ones for first and second resonances. The first peak close to 1.8 GHz is almost defined by magnetic response $\boldsymbol{M}$ (Fig. 4). Other multipoles are sufficiently suppressed and do not contribute to the response of the system. We also recalculated the shape of the scattering resonance from multipoles, which in good agreement with CST calculated scattering cross section.

The second resonance at 2.17 GHz is a result of interaction between components of electric dipole P_x and magnetic quadrupole Qm_{yz}= Qm_{zy} (Fig. 5). Other multipoles tend to zero and do not contribute to the response of the system.

The third peak at 2.65 GHz is also characterized by electric dipole P_x and magnetic quadroupole Qm_{yz} components (Fig. 6). Indeed, scattering responses at 2.17 GHz (Fig. 5a) and 2.65 GHz (Fig. 6a) have identical multipoles contributions. However, we analyze their phases close to resonances in order to find difference between them. The phases of electric dipole and magnetic quadrupole on 2.175 GHz (Fig. 5b) are both positive and equal to 1.752 rad and 0.1338 rad, respectively. However, the phase of magnetic quadrupole on 2.648 GHz is negative, namely −1.9 rad (Fig. 6b). In order to demonstrate resulted radiation pattern of resonance peak 2.175 GHz and 2.648

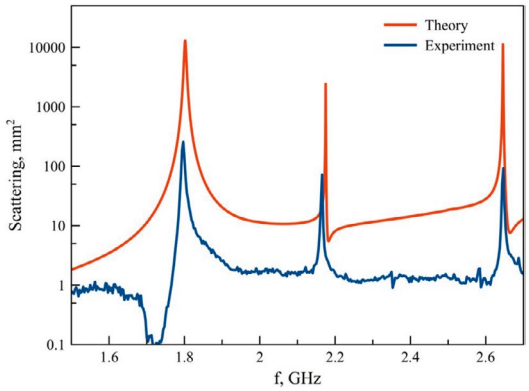

Figure 3. Simulated and measured scattering characteristics of spheroid with aspect ratio $a/b = 1.56$ in frequency range 1.5–2.5 GHz.

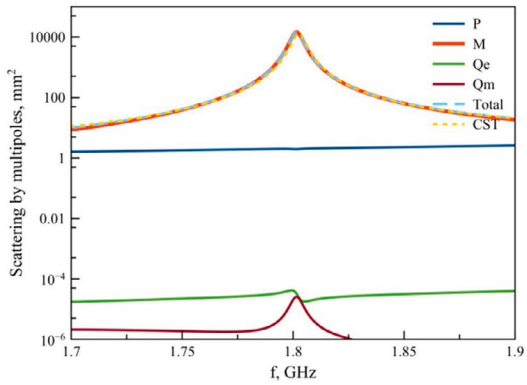

Figure 4. Scattering cross section of multipoles on 1.8 GHz.

GHz, we plot radiation patterns of electric dipole and magnetic quadrupole taken into account their amplitudes and phases. For resonance at 2.175 GHz (Fig. 5c), electric dipole and magnetic quadrupole radiate with positive phases, accordingly radiation of their interference enhanced in y direction and suppressed along z axis. Contrary, radiation on 2.648 GHz (Fig. 6c) formed by destructive interference of electric dipole and magnetic quadrupole in y direction, but radiation in z direction is identical in forward and backward directions.

Thus, the scattering pattern of all-dielectric spheroidal particle is defined by electric dipole and magnetic quadrupole and the phase signs. Our simulation results are in good agreement with Eq. (3).

Proof-of-concept microwave experiment

For the observation of transverse scattering via proof-of-concept microwave experiment, we use high-voltage capacitor ceramic K15U-2 that is made of titanate-based ceramics ($SrTiO_3$). For this purpose, we fabricate ceramic spheroidal particle with large axis of $2a = 19.5 \pm 0.1$mm and small axis $2b = 12.5 \pm 0.1$ mm from a ceramic cylinder by mechanical grinding process. The dimensions of the particle are determined by a caliper whose measurement accuracy is ±0.1 mm. These kind ceramics provide extremely high dielectric permittivity (up to 180) in microwave with an associated loss tangent in the range $\tan\delta = 10^{-4} - 10^{-3}$ (see Refs.[34,35]). In our frequency range, the sample loss tangent is $\tan\delta = 3 \cdot 10^{-4}$ and $\varepsilon = 150$ at a frequency of 1.6–2.6 GHz[34].

In order to observe transverse scattering we perform experiment and measure radiation pattern at 2.17 GHz in two planes xy and yz.

We use an anechoic chamber with dimensions of $2 \times 2 \times 3$ m equipped by ECCOSORB absorbers, two wideband horn antennas ETS-Lingren's model 3115, Rotary table and Vector Network Analyzer Agilent E5071C ENA. We also use 20 dB gain amplifier to increase the signal-to-noise ratio. Our setup permits to measure signal variation on the scale up to − 80 dB. In order to exclude all errors and noise from measured data, we measure

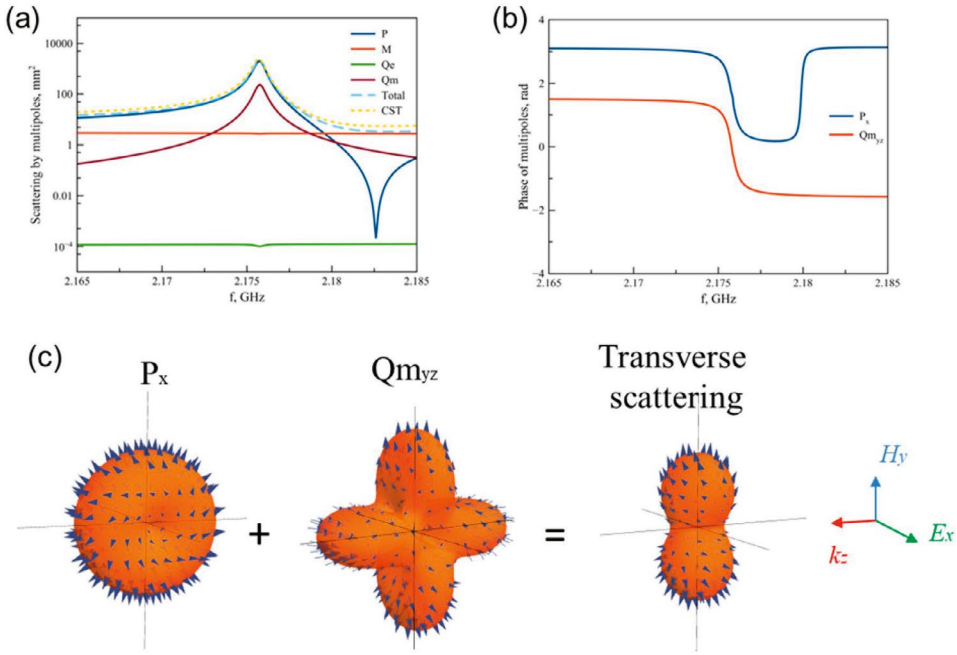

Figure 5. (**a**) Scattering cross section of multipoles on 2.175 GHz. (**b**) Phases of electric dipole and magnetic quadrupole. (**c**) Radiation pattern of excited electric dipole and magnetic quadrupole and total radiation pattern.

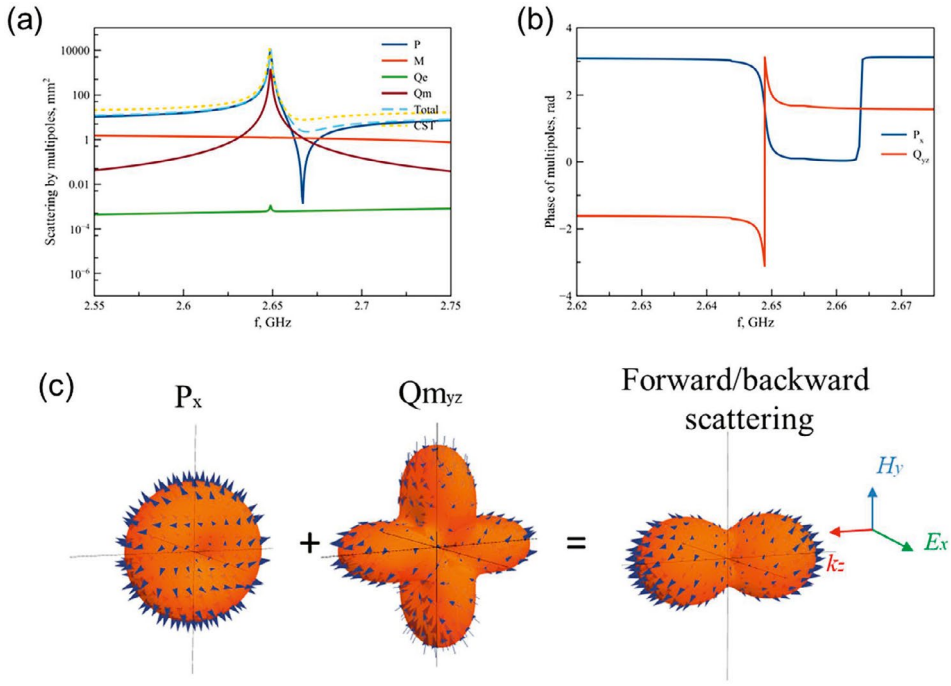

Figure 6. (**a**) Scattering cross section of multipoles on 2.64 GHz. (**b**) Phases of electric dipole and magnetic quadrupole. (**c**) Radiation pattern of excited electric dipole and magnetic quadrupole and total radiation pattern.

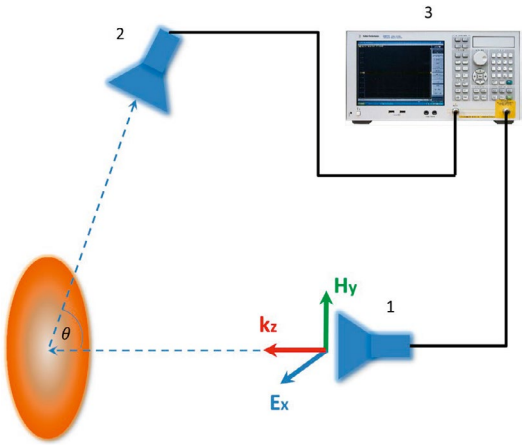

Figure 7. Sketch of experiment setup.1- transmitting antenna, 2- receiving antenna, 3-VNA Agilent E5071 C ENA.

scattering cross-section without sample and with sample[36–38]. The reasons for measurement errors in microwave experiments are range from random internal thermal noise of electronic devices to residual external echoes from obstacles of the range, non ideal absorbers, cables, rotators and etc. (See page 120 in[36]). In order to reduce these errors, the signal scattered from particle was normalized to the signal scattered from the area without particle, pages 147–148[36]. This being the case, the background radiation should be measured in the absence of a scatterer, and then scatterer should be measured in the presence of background radiation. The desired scattering signal from the particle have been extracted from the particle-plus-background signal. This processing is provided as an option of VNA Agilent E5071 C ENA.

The size of anechoic chamber provides a working zone of about 20 cm^3 at frequencies of interest to us, which is quite enough for measuring a spheroidal particle with the size of 20 mm. Considering that broadband horn antennas form a pseudo-spherical front, at a distance greater than the wavelength[36] within the dimensions of the spheroid, we can consider it as plane wave front, which is sufficient for measuring scattering patterns[36–38]. According to page 130, formula 4.10[36] far field criterion for measurements is perform: $R > \frac{2d^2}{\lambda}$, where R-distance between antenna and particle, d -size of particle, λ- wavelength. The sketch of the experimental setup is shown in Fig. 7. A wide band horn antenna 1 was used to generate the incident wave to excite the spheroidal particle. Another received antenna 2 positioned was used to detect the scattered from the particle signal. The distance between antenna and particle is 1.5 m. The antennas were connected to the ports of a Vector Network Analyzer by a 50 Ohm cable. The polarization of the wave was set as depicted in Fig. 7. In order to measure the radiation pattern we rotated antenna 2 by angle theta around the particle in two planes xy and yz and measured signal scatterer by the particle.

Obviously, the normalized radiation patterns in both planes of spheroid remind the dumbbell shape and coincide with the simulated by CST Microwave Studio pattern (Fig. 8), and we observe strong transverse scattering, reminiscent patterns resulted as interference of electric dipole and magnetic quadrupole multipoles (3) while forward and backward scattering is negligible. We also add theoretical pattern in manner of formula (3) for comparison with theoretical results. Due to our experiment we observe suppression scattering in 0 and 180 deg directions. However, the scattering in lateral 90 and 270 deg directions is pronounced. The distance between emitting antenna and spheroidal particle is 1.5 m. All radiation patterns are in good agreement with simulation results obtained by CST Microwave studio, the measured errors are enough for such kind of anechoic chamber (±2.5 dB)[36]. Our results are qualitatively demonstrating dumbbell scattering. However, we suppose that the difference between experimental and CST-calculated curves can be appeared due to presented losses in ceramic material. Thus, the resonant peaks in the experiment (Fig. 3) look less broadened. Moreover, we fabricated spheroids from the cylinders and manufacturing errors lead to the fact that the tops of the spheroids can be more flattened, which gives a wider radiation pattern.

Summary

Recently, the authors actively discussed the transverse Kerker effect of suppression scattering in forward or backward direction. However, Ufimtsev introduced another principle of invisibility[39]. He showed in 1962 (English translated in 1971) that the waves can bend around of body and diffracted in lateral directions. He called these waves as edges waves. Moreover, our effect of dumbbell-form scattering is different from invisibility effect due to enhanced scattering cross-section, while Kerker effect and Ufimtsev scattering aim to reduce scattering in whole.

We would like to remark that implementation of particles with such dumbbell scattering with near zero forward/backward scattering can be fabricated without complicated anisotropic and multilayer systems, as well

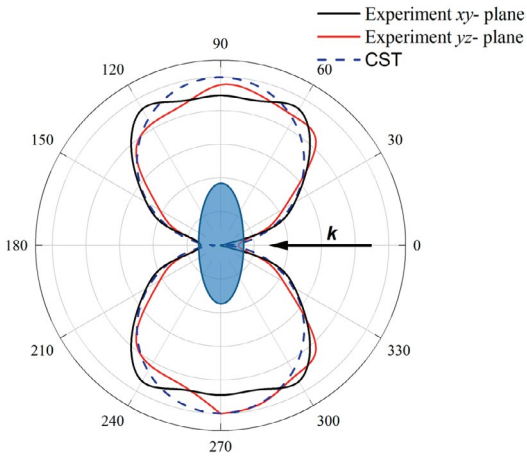

Figure 8. Experimental radiation pattern on 2.17 GHz for *xy*-plane, *yz*-plane compared with theory.

as without strong loss plasmonic materials. For a spherical particle, it is impossible to simultaneously suppress forward and backward scattering due to the optical theorem. However, for spheroids and other geometries, the optical theorem is modified to provide suppression of both forward/backward scattering in the presence of strong side scattering. Moreover, we propose that in optical experiments spheroidal particles may be replaced by elliptical cylinders. Note, that transverse dumbbell Kerker effect can be realized in planar structures by interaction of magnetic dipoles and electric quadrupoles.

Moreover, we suppose that in optical experiments spheroidal particles may be fabricated from low-index dielectrics like silicon or silica. The semiconductor nanoparticles behave well in optical range and can be easily tuned for required *nm* dimensions. But their permittivity is not so large ($\varepsilon \sim 16$) in optics.

Thus, we can expect a similar effect of transverse dumbbell scattering in THz and in optics by using these materials, though the Q-factor of resonances will be lower than in microwave. Moreover, several papers have demonstrated spheroidal particle fabrication process[40–42]. The long-awaited problem in photonics of planar lasers excited laterally would be realized by metasurfaces of proposed particles. Obviously, for this frequency range, the choice of dielectric material should be corrected toward resonant values. For example, Si, Ge, GaAs particles of nanodisks and cylindric shape have shown resonant behavior in optical frequencies[43]. Moreover, polaritonic crystals NaCl, KCl, LiF, $LiTaO_3$ are promising for THz frequency range[44–46]. Thus, we simulate response of spheroids with $a/b = 1.56$ for different permittivities reminiscent materials from our ceramics ($\varepsilon = 150$) to silicon in optical frequencies ($\varepsilon = 16$). The peak of dumbbell Kerker effect still exists for low permittivities, but its Q-factor is decreased (Fig. 9). For example, for silicon ($\varepsilon = 16$), its Q-factor is 32. Thus, we can expect that observation of transverse Kerker effect can be possible for low index materials in optics.

For this aim, we observe evolution of the transverse scattering peak dependence on permittivity and simulated scattering cross-section of spheroidal particles with size $a/b = 1.56$. For low permittivity of silicon ($\varepsilon = 16$) the scattering cross-section is low and broadband and its maximum is 7 (Fig. 10a). To achieve the transverse Kerker effect in visible optics (red light 700 nm), the particle should have dimensions $a = 423nm$ and $b = 271nm$.

However, as the permittivity of the spheroid grows, the scattering intensity increases, and the peak associated with the transverse Kerker effect becomes narrower. One can choose the material value and dimensions according to our graphs (Fig. 10b–d). Thus, for permittivity values of 25, polaritonic crystals (NaCl, KCl, LiF) in THz regime are suitable, and for values of 100 or more, BSTO ceramics in microwaves. Meanwhile, for calculation of the Q-factors of asymmetric Fano resonance we used Fano resonance approach[47]. Thus, Q-factor obtained from the scattering spectra is $Q = \frac{f_d + f_p}{f_d - f_p}$, where the resonant region lies between the dip f_d and peak f_p frequencies.

Conclusion

In this work, we proposed conditions for transverse dumbbell scattering based on interaction between multipoles of electric dipole and magnetic quadrupole moments. Our condition is beyond invisibility effects like classical and transverse Kerker effect and also anapole mode with suppressed scattering cross-section. In contrary, our scattering is enhanced in lateral directions in comparison with scattering in forward/backward directions which is suppressed. Therefore, by fabricated all-dielectric ceramic spheroidal particle based on K15U-2 capacitor ceramic, we proposed proof-of-concept microwave experiment and demonstrated dumbbell scattering in perpendicular to incident wave vector. At the same time, we observed suppressed forward and backward scattering. Our concept can be applied as ingredients for lateral excitation of planar lasers, waveguides and nanoantennas.

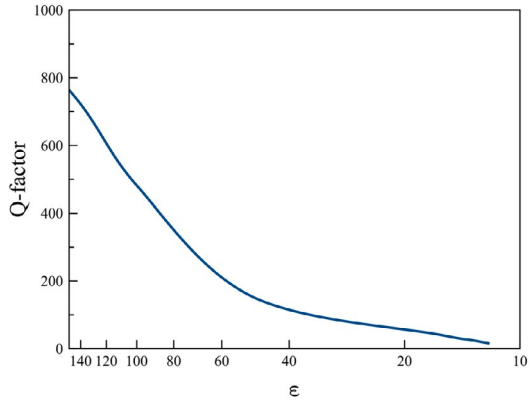

Figure 9. Dependence of dumbbell Kerker effect Q-factor on permittivity ε for spheroids of $a/b = 1.56$.

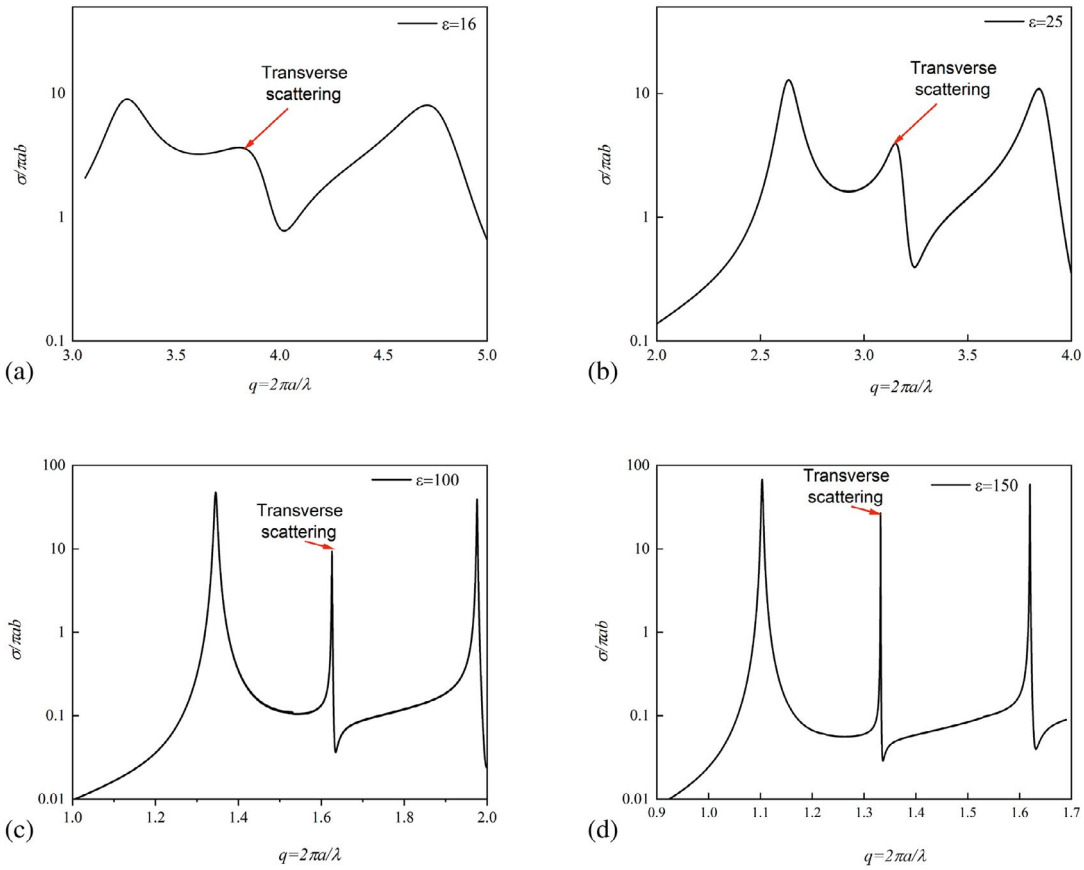

Figure 10. Normilized Scattering cross-section of spheroidal all-dielectric particle for different permittivities 16,25,100,150.

Methods

The radiation of arbitrary source is formulated by electric field of multipoles. For $l = 1$, radiation is presented by electric and magnetic dipoles, while for $l = 2$ by electric and magnetic quadrupoles. Due to electric and toroidal dipoles radiate with the same radiation pattern in far-field zone, we combine them as total electric dipole $\boldsymbol{P}$

$$\begin{aligned}\mathbf{E}_{(P)} &\approx \frac{\mu_0 c^2}{3\sqrt{2\pi}} \frac{\exp(-ikr)}{r} \sum_{m=0,\pm1} \left[(k^2 Q_{1,m} - ik^3 T_{1,m}) \times \left(\mathbf{Y}_{1,2,m} + \sqrt{2}\mathbf{Y}_{1,0,m} \right) \right], \\ \mathbf{E}_{(Qm)} &\approx \frac{\mu_0 c^2}{10\sqrt{6\pi}} \frac{\exp(-ikr)}{r} \sum_{m=0,\pm1,\pm2} \left[-\sqrt{5} k^3 Q^{(m)}_{2,m} \times \mathbf{Y}_{2,2,m} \right], \\ \mathbf{E}_{(total)} &\approx \mathbf{E}_{(P)} + \mathbf{E}_{(Qm)}.\end{aligned} \tag{6}$$

For $\varphi = \frac{\pi}{2}$ and $\widehat{x}, \widehat{y}, \widehat{z}$-basis in Cartesian coordinates

$$\begin{aligned}E(\theta, \varphi = \pi/2) \approx &\left(C_1 P_x + \frac{C_2}{4} (4Qm_{yz} \cos 2\theta + (Qm_{yy} - Qm_{xx} - 3Qm_{zz}) \sin 2\theta) \right) \widehat{x} \\ &+ \left(C_1 (P_y \cos\theta - P_z \sin\theta) \cos\theta - C_2 (Qm_{xz} \cos\theta + Qm_{xy} \sin\theta) \cos\theta \right) \widehat{y} \\ &+ \left(C_1 (P_z \sin\theta - P_y \cos\theta) \sin\theta + C_2 (Qm_{xz} \cos\theta + Qm_{xy} \sin\theta) \sin\theta \right) \widehat{z}.\end{aligned} \tag{7}$$

Here C_1 and C_2 are θ-independent constants:

$$C_1 = \frac{e^{-ikr} c^2 \mu_0 k^2}{4\pi r}, \quad C_2 = \frac{i e^{-ikr} c^2 \mu_0 k^3}{8\pi r}. \tag{8}$$

We can obtain condition for dumbbell radiation pattern in $\widehat{x}, \widehat{y}, \widehat{z}$ directions or along $\boldsymbol{E}$, $\boldsymbol{H}$, $\boldsymbol{k}$.

It is following from Eq. 7) for θ=0 and $\theta = \pi$ (transverse scattering) or for $\theta = \pi/2$ and $\theta = 3\pi/2$ for simultaneously suppressed forward/backward scattering

$$E_{(total)}(\theta, \phi = \pi/2, r = 1) \approx C_1 P_\alpha + C_2 Qm_{\beta\gamma} \cos 2\theta = 0. \tag{9}$$

We note that components $Qm_{xx}, Qm_{yy}, Qm_{zz}$ radiate with zero $\boldsymbol{E}$-fields for transverse scattering due to $sin2\theta = 0$. However, function $\cos 2\theta$ for other components of magnetic quadrupole forms four-lobe radiation pattern.

Accordingly, we obtain 3 conditions for dumbbell radiation pattern along $\boldsymbol{E}$, $\boldsymbol{H}$, $\boldsymbol{k}$ vectors:

1. For radiation pattern along $\boldsymbol{H}$ vector and suppressed scattering along $\boldsymbol{k}$ and $\boldsymbol{E}$, as in our experiment:

$$C_1 P_x + C_2 Qm_{yz} = 0, \quad C_1 P_y - C_2 Qm_{xz} = 0. \tag{10}$$

For multipoles, we have

$$\frac{P_x}{Qm_{yz}} = -\frac{ik}{2}, \quad \frac{P_y}{Qm_{xz}} = \frac{ik}{2}. \tag{11}$$

2. For radiation pattern along $\boldsymbol{k}$ vector and suppressed scattering along $\boldsymbol{E}$ and $\boldsymbol{H}$:

$$C_1 P_x - C_2 Qm_{yz} = 0, \quad C_1 P_z + C_2 Qm_{xy} = 0. \tag{12}$$

For multipoles:

$$\frac{P_x}{Qm_{yz}} = \frac{ik}{2}, \quad \frac{P_z}{Qm_{xy}} = -\frac{ik}{2}. \tag{13}$$

3. For radiation pattern along $\boldsymbol{E}$ vector and suppressed scattering along $\boldsymbol{k}$ and $\boldsymbol{H}$, $\varphi = 0$:

$$C_1 P_y + C_2 Qm_{xz} = 0, \quad C_1 P_z - C_2 Qm_{xy} = 0. \tag{14}$$

For multipoles:

$$\frac{P_y}{Qm_{xz}} = -\frac{ik}{2}, \quad \frac{P_z}{Qm_{xy}} = \frac{ik}{2}. \tag{15}$$

Received: 28 September 2021; Accepted: 26 April 2022
Published online: 14 May 2022

References

1. Grahn, P., Shevchenko, A. & Kaivola, M. Electromagnetic multipole theory for optical nanomaterials. *New J. Phys.* **14**, 093033 (2012).
2. Novotny, L. & Hecht, B. *Principles of Nano-Optics* (Cambridge Univ. Press, 2012).
3. Kuznetsov, A. I., Miroshnichenko, A. E., Brongersma, M. L., Kivshar, Y. S. & Luk'yanchuk, B. S. Optically resonant dielectric nanostructures. *Science* **354**, 6314 (2016).

4. Jackson, J. *Classical Electrodynamics* (Wiley, 1975).
5. Luk'yanchuk, B. S. *et al.* The Fano resonance in plasmonic nanostructures and metamaterials. *Nat. Mater.* **9**, 707–715 (2010).
6. Liu, W. & Kivshar, Y. S. Generalized Kerker effects in nanophotonics and meta-optics [Invited]. *Opt. Expr.* **26**, 13085–13105 (2018).
7. Miroshnichenko, A. E. *et al.* Nonradiating anapole modes in dielectric nanoparticles. *Nat. Commun.* **6**, 8069 (2015).
8. Shamkhi, H. K. *et al.* Transparency and perfect absorption of all-dielectric resonant metasurfaces governed by the transverse Kerker effect. *Phys. Rev. Mater.* **3**, 085201 (2019).
9. Koshelev, K., Lepeshov, S., Liu, M., Bogdanov, A. & Kivshar, Y. Asymmetric metasurfaces with high-Q resonances governed by bound states in the continuum. *Phys. Rev. Lett.* **121**, 193903 (2018).
10. Kerker, M., Wang, D. & Giles, G. Electromagnetic scattering by magnetic spheres. *J. Opt. Soc. Am.* **73**, 765–767 (1983).
11. Evlyukhin, A. B. *et al.* Demonstration of magnetic dipole resonances of dielectric nanospheres in the visible region. *Nano Lett.* **12**, 3749–3755 (2012).
12. Geffrin, J. M. *et al.* Magnetic and electric coherence in forward- and back-scattered electromagnetic waves by a single dielectric subwavelength sphere. *Nat. Commun.* **3**, 1171 (2012).
13. Fu, Y. H., Kuznetsov, A. I., Miroshnichenko, A. E., Yu, Y. F. & Luk'yanchuk, B. S. Directional visible light scattering by silicon nanoparticles. *Nat. Commun.* **4**, 1527 (2013).
14. Person, S. *et al.* Demonstration of zero optical backscattering from single nanoparticles. *Nano Lett.* **13**, 1806–1809 (2013).
15. Staude, I. *et al.* Tailoring directional scattering through magnetic and electric resonances in subwavelength silicon nanodisks. *ACS Nano* **7**, 7824–7832 (2013).
16. Luk'yanchuk, B. S., Voshchinnikov, N. V., Paniagua-Domínguez, R. & Kuznetsov, A. I. Optimum forward light scattering by spherical and spheroidal dielectric nanoparticles with high refractive index. *ACS Photon.* **2**, 993–999 (2015).
17. Lee, J. Y., Miroshnichenko, A. E. & Lee, R.-K. Simultaneously nearly zero forward and nearly zero backward scattering objects. *Opt. Exp.* **26**, 30393–30399 (2018).
18. Shamkhi, H. K. *et al.* Transverse scattering and generalized Kerker effects in all-dielectric Mie-resonant metaoptics. *Phys. Rev. Lett.* **122**, 193905 (2019).
19. Zanganeh, E. *et al.* Anapole meta-atoms: Nonradiating electric and magnetic sources. *Phys. Rev. Lett.* **127**, 096804 (2021).
20. Luk'yanchuk, B., Paniagua-Domínguez, R., Kuznetsov, A. I., Miroshnichenko, A. E. & Kivshar, Y. S. Hybrid anapole modes of high-index dielectric nanoparticles. *Phys. Rev. A* **95**, 063820 (2017).
21. Ospanova, A. K., Basharin, A. A., Miroshnichenko, A. E. & Luk'yanchuk, B. S. Generalized hybrid anapole modes in all-dielectric ellipsoid particles. *Opt. Mater. Express* **11**, 23 (2021).
22. Luk'yanchuk, B., Paniagua-Domínguez, R., Kuznetsov, A. I., Miroshnichenko, A. E. & Kivshar, Y. S. Suppression of scattering for small dielectric particles: Anapole mode and invisibility. *Phil. Trans. R. Soc. A* **375**, 20160069 (2017).
23. Nemkov, N. A., Basharin, A. A. & Fedotov, V. A. Nonradiating sources, dynamic anapole, and Aharonov-Bohm effect. *Phys. Rev. B* **95**, 165134 (2017).
24. Nemkov, N. A., Basharin, A. A. & Fedotov, V. A. Electromagnetic sources beyond common multipoles. *Phys. Rev. A* **98**, 023858 (2018).
25. Papasimakis, N., Fedotov, V. A., Savinov, V., Raybould, T. A. & Zheludev, N. I. Electromagnetic toroidal excitations in matter and free space. *Nat. Mater.* **15**, 263–271 (2016).
26. Gurvitz, E. A. *et al.* The high-order toroidal moments and anapole states in all-dielectric photonics. *Laser Photon. Rev.* **13**, 1800266 (2019).
27. Draine, B. T. & Hensley, B. S. Using the starlight polarization efficiency integral to constrain shapes and porosities of interstellar grains. *Astrophys. J.* **919**, 65 (2021).
28. Farafonov, V. G., Il'in, V. B. & Ustimov, V. I. Ellipsoidal models of small non-spherical scatterers. *Opt. Quant. Electron.* **52**, 23 (2020).
29. Fennema, E., Rivron, N., Rouwkema, J., Blitterswijk, C. & Boer, J. Spheroid culture as a tool for creating 3D complex tissues. *Trends Biotechnol.* **31**, 108–115 (2013).
30. Valero, A. C. *et al.* Theory, observation, and ultrafast response of the hybrid anapole regime in light scattering. *Laser Photon. Rev.* **15**, 2100114 (2021).
31. Savinov, V., Fedotov, V. A. & Zheludev, N. I. Toroidal dipolar excitation and macroscopic electromagnetic properties of metamaterials. *Phys. Rev. B* **89**, 205112 (2014).
32. Asano, S. & Yamamoto, G. Light scattering by a spheroidal particle. *Appl. Opt.* **14**, 29–49 (1975).
33. Ni, Y. X., Gao, L., Miroshnichenko, A. E. & Qiu, C. W. Controlling light scattering and polarization by spherical particles with radial anisotropy. *Opt. Expr.* **21**, 8091–8100 (2013).
34. Skanavi, G. I. *Dielectric Polarization and Loss in Glasses and Ceramic Materials with High Dielectric Permeability* (Gosenergoizdat, 1952).
35. Luk'yanchuk, B. S. *et al.* Colossal magnetic fields in high refractive index materials at microwave frequencies. *Sci. Rep.* **11**, 23453 (2021).
36. Knott, E. F., Shaeffer, J. F. & Tuley, M. T. *Radar Cross Section* 231 (Artech House, 1993).
37. Balanis, C. A. *Antenna Theory: Analysis and Design* (Wiley, 2005).
38. Balanis, C. A. *Advanced Engineering Electromagnetics* (Wiley, 2012).
39. Ufimtsev, P. *Method of Edge Waves in the Physical Theory of Diffraction* (U.S. Air Force Foreign Technology Division, 1971).
40. Champion, J. A., Katare, Y. K. & Mitragotri, S. Making polymeric micro- and nanoparticles of complex shapes. *Proc. Nat. Acad. Sci. USA* **104**, 11901–11904 (2007).
41. Vazquez, N. I., Gonzalez, Z., Ferrari, B. & Castro, Y. Synthesis of mesoporous silica nanoparticles by sol-gel as nanocontainer for future drug delivery applications. *Bolet. Soc. Esp. Ceram. Vid.* **56**, 139–145 (2017).
42. Selvarajan, V., Obuobi, S. & Ee, P. L. R. Silica nanoparticles: A versatile tool for the treatment of bacterial infections. *Front. Chem.* **8**, 602 (2020).
43. Baranov, D. G. *et al.* All-dielectric nanophotonics: the quest for better materials and fabrication techniques. *Optica* **4**, 814–825 (2017).
44. Pawlak, D. A. *et al.* Metamaterials: how far are we from making metamaterials by self-organization? The microstructure of highly anisotropic particles with an SRR-like geometry. *Adv. Funct. Mater.* **20**, 7 (2010).
45. Massaouti, M. *et al.* Eutectic epsilon-near-zero metamaterial terahertz waveguides. *Opt. Lett.* **38**, 1140–1142 (2013).
46. Acosta, M. F. *et al.* Micropillar templates for dielectric filled metal arrays and flexible metamaterials. *Adv. Opt. Mater.* **5**, 1600670 (2017).
47. Fan, Yu. *et al.* Achieving a high-Q response in metamaterials by manipulating the toroidal excitations. *Phys. Rev. A* **97**, 033816 (2018).

Acknowledgements

This work was supported by Ministry of Science and Higher Education of the Russian Federation (grant 14.W03.31.0008). This work was partially supported by the Russian Science Foundation (No. 20-12-00389). The multipole decomposition calculations was supported by Russian Science Foundation (No. 20-72-00016).

AAB work of analytical study of electromagnetic scattering was funded by the Russian Science Foundation (No. 21-19-00138). This work was supported by the Academy of Finland Flagship Programme, Photonics Research and Innovation (PREIN) (Project No 320166). The reported study was funded by RFBR, project number 20-02-00715. The experimental study of measuring spectra and the magnetic intensity distribution was supported by the Ministry of Science and Higher Education of the Russian Federation (State Assignment No. 075-00460-21-00). V.I. was partly supported by Ministry of Science and Higher Education of Russian Federation (grant FSRF-2020-0004) and in his decomposition calculations for spheroids by the grant RSF 20-72-10052.

Author contributions

M.M.B., A.K.O., V.B.I., A.A.B. and B.L. designed and performed the numerical simulation, multipole decomposition of the structure. V.Ya.P., L.M.V fabricated sambles and performed microwave experiments. All authors discussed the results and approved the manuscript. All authors reviewed the manuscript.

Competing interests

The authors declare no competing interests.

Additional information

Correspondence and requests for materials should be addressed to A.A.B.

Reprints and permissions information is available at www.nature.com/reprints.

Publisher's note Springer Nature remains neutral with regard to jurisdictional claims in published maps and institutional affiliations.

ARTICLE III

A. Ospanova, M. Cojocari, P. Lamberti, A. Plyushch, L. Matekovits, Yu. Svirko, P. Kuzhir, A. Basharin

“Broadband transparency of Babinet complementary metamaterials”

Appl. Phys. Lett. 122, 231702 (2023)

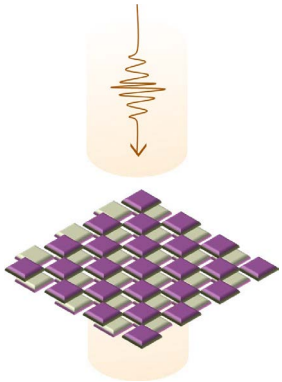

ANAR OSPANOVA

This thesis presents novel electromagnetic phenomena in spheroidal particles such as transverse Kerker effect as well as metamaterial transparency based on multipole interaction. The multipole decomposition method for modified multipoles underlying these techniques has proven to be a reliable tool for the study of resonances in complex metaparticles.
The obtained experimental results allow for further successful practical application in number of sensing, modulation and data transfer issues.

UNIVERSITY OF
EASTERN FINLAND

uef.fi

PUBLICATIONS OF
THE UNIVERSITY OF EASTERN FINLAND
Dissertations in Science, Forestry and Technology

ISBN 978-952-61-5330-8
ISSN 2954-131X